Title

Hyperpolarized C-13 Magnetic Resonance Imaging for Assessing Tissue Metabolism and Microenvironment: Technical Development, Preclinical Validation, and Clinical Translation

Permalink

https://escholarship.org/uc/item/9sz5z7g3

Author

Qin, Hecong

Publication Date

2021

Peer reviewed|Thesis/dissertation

Hyperpolarized C-13 Magnetic Resonance Imaging for Assessing Tissue Metabolism and Microenvironment: Technical Development, Preclinical Validation, and Clinical Translation

by

Hecong Qin

DISSERTATION
Submitted in partial satisfaction of the requirements for degree of

DOCTOR OF PHILOSOPHY

in

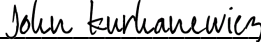Bioengineering

in the

GRADUATE DIVISION
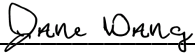
of the

UNIVERSITY OF CALIFORNIA, SAN FRANCISCO
AND
UNIVERSITY OF CALIFORNIA, BERKELEY

Approved:

_____   John Kurhanewicz _____
                                                                                                                        Chair

_____   Daniel Vigneron _____

_____   Peder Larson _____

_____   Jane Wang _____

_____
                                                                                                        Committee Members

Acknowledgments

First and foremost, I thank my dissertation advisor Dr. John Kurhanewicz. John engaged me in multiple basic science and clinical research projects, through which I grew as an independent researcher. He also gave me the freedom to pursue my academic interest and collaborate with multiple PIs, and entrusted me with the responsibility of leading an NIH R01 grant. This research and leadership experience shaped my academic career trajectory, and I am proud of what we have accomplished together. I will always be grateful for John's kindness, mentorship, and the opportunities he created for me.

My graduate education was significantly enhanced by having worked closely with Drs. Jane Wang and David Wilson, two exceptional physician-scientists. In addition to helping me publish two first-author papers, they have been my champions and advocates and encouraged me to pursue a career in academic medicine. They modeled scientific rigor and critical thinking, and even coached me on writing manuscripts and delivering presentations. I will always be grateful for their mentorship and friendship.

I thank Dr. Daniel Vigneron for chairing my qualifying exam committee, serving on my dissertation committee, and advising me throughout the graduate school; Dr. Peder Larson for serving on my qualifying exam and dissertation committees and for choosing me to be his teaching assistant; Dr. Renuka Sriram for her mentorship and always making herself available to discuss science with me; Dr. Romelyn Delos Santos for her assistance with countless experiments and always looking out for me; Dr. Robert Bok for his expertise in animal models and cancer research; Drs. Andrew Riselli and Jim Slater for their expertise in pharmacy regulatory compliance.

Science is teamwork. My labmates at the Kurhanewicz Group built an inclusive lab environment for collaboration and intellectual exchange – Jinny Sun, Natalie Korn, Shubhangi Agarwal, David Korenchan, Jessie Lee, Justin Delos Santos, and Jeremy Bancroft Brown. I also had the opportunity to collaborate with two fellow BioE graduate students, Shuyu Tang and Xucheng Zhu,

Contributions

Chapter 2 is adapted from **Qin, H.**, Carroll, V.N., Sriram, R., Villanueva-Meyer, J.E., Von Morze, C., Wang, Z.J., Mutch, C.A., Keshari, K.R., Flavell, R.R., Kurhanewicz, J. and Wilson, D.M., 2018. Imaging glutathione depletion in the rat brain using ascorbate-derived hyperpolarized MR and PET probes. *Scientific Reports*, 8(1), pp.1-9. This work was supported by National Institute of Health (NIH) grants R01CA166766 and P41EB013598.

Chapter 3 is adapted from **Qin, H.**, Zhang, V., Bok, R.A., Santos, R.D., Cunha, J.A., Hsu, I.C., Santos, J.D., Lee, J.E., Sukumar, S., Larson, P.E. and Vigneron, D.B., 2020. Simultaneous Metabolic and Perfusion Imaging Using Hyperpolarized ^{13}C MRI Can Evaluate Early and Dose-Dependent Response to Radiation Therapy in a Prostate Cancer Mouse Model. *International Journal of Radiation Oncology* Biology* Physics*, 107(5), pp.887-896. This work was supported by NIH grants R01CA214554, R01CA166655, and P41EB013598.

Chapter 4 is adapted from a manuscript submitted to *Magnetic Resonance in Medicine*: **Qin, H.**, Tang S., Riselli, A.M., Bok, R.A., Delos Santos, R., van Criekinge, M., Gordon J.W., Aggarwal, R., Chen, R., Goddard, G.D., Zhang, C.T., Chen, A., Reed, G., Ruscitto, D.M., Slater, J., Sriram, R., Larson, P.E.Z, Vigneron, D.B., Kurhanewicz, J., 2021. Clinical Translation of Hyperpolarized ^{13}C Pyruvate and Urea MRI for Simultaneous Metabolic and Perfusion Imaging. This work was supported by NIH grants R01CA214554 and P41EB013598.

Most figures in Chapter 1 are adapted from references for educational purposes; I claim no copyrights for them. All other figures (those without citations in the captions) are my original work, but the copyrights of the figures in Chapter 2 and Chapter 3 belong to Nature Research and Elsevier, respectively, as figures in these two chapters were adapted from my previously published manuscripts.

Abstract

Hyperpolarized C-13 Magnetic Resonance Imaging for Assessing Tissue Metabolism and

Microenvironment: Technical Development, Preclinical Validation, and Clinical Translation

Hecong Qin

Hyperpolarized (HP) C-13 magnetic resonance (MR) is an emerging molecular imaging technique that has shown the potential to assess metabolic and microenvironmental alterations in various diseases. MR spectroscopic imaging methods can monitor the distribution and biochemical conversion of injected HP C-13 labeled probes. These quantitative imaging markers could address the unmet clinical needs of non-invasive evaluation of cancer aggressiveness, disease burden, and early therapeutic response or resistance. This dissertation focuses on developing HP C-13 MR probes and techniques to evaluate cellular redox capacity, glycolytic metabolism, as well as tissue perfusion and microenvironment. Chapter 1 introduces the fundamental principles of MR, hyperpolarization techniques, and their biological and clinical applications. Chapter 2 describes using ascorbate-derived MR and Positron Emission Tomography probes to interrogate *in vivo* redox capacity of the brain. Chapter 3 reports the preclinical validation of the combined HP C-13 pyruvate and urea MR as a simultaneous metabolic and perfusion imaging technique to evaluate early and dose-dependent tumor response to radiation therapy in a prostate cancer mouse model. The results of Chapter 3, combined with other prior preclinical evidence, motivated the clinical translation of this dual-probe imaging technique. Chapter 4 describes the technical development (including co-polarization system development, probe characterizations, and imaging methodology development) and non-clinical studies (including impurity characterizations, toxicology study, and imaging feasibility study) required to translate the combined C-13 pyruvate and urea MR for clinical investigations. This work has led to the regulatory approval of this combined metabolic and perfusion imaging technique for investigational use to aid prostate cancer diagnosis in patients.

Table of Contents

List of Figures

xvi

List of Tables

List of Abbreviations

2D	Two-Dimensional
3D	Three-Dimensional
ADC	Apparent Diffusion Coefficients
ALT	Alanine Transaminase
ANOVA	Analysis of Variance
ATP	Adenosine TriPhosphate
AUC	Area Under the Curve
BBB	Blood-Brain Barrier
bSSFP	balanced Steady-State Free Precession
CE	Cross Effect
CSA	Chemical Shift Anisotropy
CSI	Chemical Shift Imaging
DCE	Dynamic Contrast Enhanced
dDNP	dissolution Dynamic Nuclear Polarization
DEM	Diethyl Maleate
DHA	Dehydroascorbic Acid
DMAC	4-(Dimethylamino)cinnamaldehyde
DNP	Dynamic Nuclear Polarization
DSC	Differential Scanning Calorimetry
DWI	Diffusion-Weighted Imaging
EPA	Electron Paramagnetic Agent
EPI	Echo Planar Imaging
EPR	Electron Paramagnetic Resonance
FDA	Food and Drug Administration

FDG	Fluorodeoxyglucose
FID	Free Induction Decay
FOV	Field of View
FSE	Fast Spin Echo
FT	Fourier Transform
Gd-DTPA	Gadolinium-Diethylenetriamine Pentaacetic Acid
GLUT	Glucose Transporter
GMP	Good Manufacturing Practice
GRASE	Gradient And Spin Echo
GRE	Gradient Echo
GSH	Glutathione
HIF1-α	hypoxia-induced factor 1-α
HP	Hyperpolarized
HPLC	High-Performance Liquid Chromatography
IACUC	Institutional Animal Care and Use Committee
iAUC	initial Area Under the Curve
IDEAL	Iterative Decomposition with Echo Asymmetry and Least squares estimation
IHC	Immunohistochemistry
K^{trans}	Vascular transfer constant
LC-MS	Liquid Chromatography-Mass Spectrometry
LDH	Lactate Dehydrogenase
MCT	Monocarboxylate Transporters
MR	Magnetic Resonance
MRI	Magnetic Resonance Imaging
MRSI	Magnetic Resonance Spectroscopic Imaging
$NADH/NAD^+$	Nicotinamide Adenine Dinucleotide
NADHP	Nicotinamide Adenine Dinucleotide Phosphate
nLac	normalized [1-^{13}C]lactate
NMR	Nuclear Magnetic Resonance

PA	Pyruvaic Acid
PCa	Prostate Cancer
PDH	Pyruvate Dehydrogenase
PET	Positron Emission Tomography
ppm	parts per million
PPP	Pentose Phosphate Pathway
PQ	Process Qualification
Q-TOF-MS	Quadrupole Time-of-Flight Mass Spectrometry
RECIST	Response Evaluation Criteria in Solid Tumors
RF	Radiofrequency
ROS	Reactive Oxygen Species
RT	Radiation Therapy
SE	Spin Echo
SNR	Signal-to-Noise Ratio
SOP	Standard Operating Procedure
SVCT2	Sodium-dependent Vitamin C Transporter-2
SWIF	Sterile Water for Injection
Tg	Glass transition temperature
TR	Repetition Time
TRAMP	Transgenic Adenocarcinoma of Mouse Prostate
TM	Thermal Mixing
VFA	Variable Flip Angle
VitC	Vitamin C

Chapter 1: Introduction and Background

1.1 Magnetic Resonance (MR) for Biological Applications

All nucleons, including protons and neutrons, posses the intrinsic physical property of *spin* carried by elementary particles. Spin, also a form of angular momentum, is quantized with different energy levels in the presence of a magnetic field, leading to uneven distribution of spins at equilibrium according to Boltzmann distribution. Since spin is associated with magnetism, this differential spin population translates into a net magnetization, forming the basis of Nuclear Magnetic Resonance (NMR) and Magnetic Resonance Imaging (MRI). From a quantum mechanic perspective, both NMR and MRI use radiofrequency (RF) pulses, the energy of which corresponds to the energy difference between the two spin states, to perturb the spin system from its equilibrium. As spins return to equilibrium, they emit electromagnetic waves, which are collected by specialized hardware known as RF coils and subsequently converted into digital signal. Alternatively, from a classic perspective, the net magnetization, viewed as a vector, is rotated by the RF pulse at its resonance frequency to produce MR signal in the form of electromagnetic waves as the vector returning to its starting position. Finally, through signal processing, NMR spectra of metabolites and MR images of anatomy are generated for scientists and physicians. In this section, I will introduce the above abstract concepts as I understood them[1].

1.1.1 Nuclear Magnetic Resonance Physics

Spin and Magnetism. As two of the intrinsic physical properties[2], spin and magnetism are closely related. Nuclei with an odd number of protons and/or neutrons, such as ^{1}H, ^{13}C, ^{31}P, ^{15}N, possess a nuclear spin angular momentum, $\hat{S}$[3], which can be viewed as a vector and its directions

---

[1] There are many ways to describe and understand Magnetic Resonance. The perspectives presented in this section are largely derived from *Spin Dynamics: Basics of Nuclear Magnetic Resonance* by Malcolm H. Levitt and *Principle of Magnetic Resonance Imaging* by Dwight G. Nishmura [1, 2].

[2] Intrinsic physical properties include mass, electrical charge, magnetism, and spin.

[3] The ˆ sign indicates microscopic vectors associated with spin.
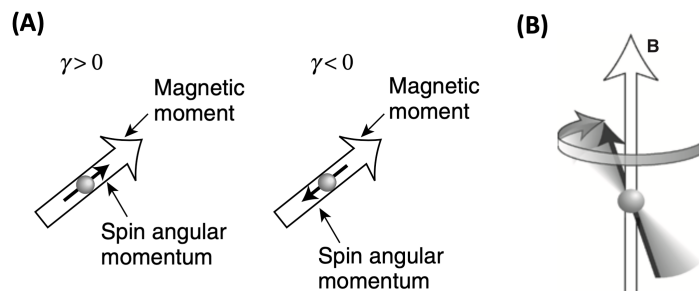
Figure 1.1: (A) Spin angular momentum, magnetic moment, and gyromagnetic ratio. (B) Spin procession in the magnetic field. Adapted from *Spin Dynamics* by Malcolm H. Levitt [2].

aligns with the axis of rotation[4] (**Figure 1.1A**). $\hat{S}$ is associated with magnetic dipole momentum $\hat{\mu}$ through a physical constant defined as gyromagnetic ratio (γ):

$$\hat{\mu} = \gamma \hat{S} \tag{1.1}$$

This means that the magnetic moment is either parallel or antiparallel to the spin angular momentum, depending on the sign of γ (**Figure 1.1A**). For ^{1}H and ^{13}C nuclei, $\gamma > 0$, so $\hat{\mu}$ aligns with $\hat{S}$. For ^{15}N nuclei, $\gamma < 0$, so $\hat{\mu}$ aligns against $\hat{S}$. Since $\hat{S}$ could be pointed to any directions, the distribution of $\hat{\mu}$ within a given volume is *isotropic* in the absence of magnetic field, i.e., zero net magnetization (**Figure 1.2A**).

However, in presence of a magnetic field (B_0), if $\hat{\mu}$ points to a different direction than B_0, the spin axis will move around the direction of B_0 maintaining a fixed angle between the field direction and the spin axis – this happens because particles with spin possess both angular momentum and magnetic moment. This phenomenon is called *spin precession*[5] (**Figure 1.1B**). From a classic perspective, the magnetic field B_0 applies a torque on $\hat{\mu}$ that equals the rate of change of angular momentum:

$$\frac{d\hat{S}}{dt} = \hat{\mu} \times \hat{B}_0 \tag{1.2}$$

Multiply both sides by γ,

$$\frac{d\hat{\mu}}{dt} = \hat{\mu} \times \gamma \hat{B}_0 \tag{1.3}$$

---

[4]Note that spin is not produced by particle precessing; the particles simply possess it.

[5]Spin precession can be viewed as a tilted but perfectly-balanced spinning top on frictionless surface that never stops.

The solution to above equation shows that $\hat{\mu}$ precesses about B_0 at a frequency given by

$$\omega = \gamma \cdot B_0 \tag{1.4}$$

$$f = \frac{\gamma}{2\pi} \cdot B_0 \tag{1.5}$$

The above equations show that the gyromagnetic ratio $(rad^{-1} \cdot s^{-1} \cdot T^{-1})$ governs the angular frequency of spin precession at a given magnetic field (B_0, T). This frequency is known as the Larmor frequency (ω) and is involved in both quantum and classical descriptions of NMR.

Spin Polarization. From a quantum mechanic perspective, spin angular momentum $\hat{S}$ is quantized into sublevels. The total angular momentum of particles with spin is derived from $[S(S-1)]^{1/2}\hbar$, where S is the spin quantum number and h is Planck's constant divided by 2π $(1.054 \times 10^{-34}\ m^2 \cdot kg \cdot s^{-1})$. Moreover, particles with spin have $(2S+1)$ sublevels, where S can be half integers such as 1/2, 2/3, 5/2, or integers such as 0, 1, 2. For both ^{1}H and ^{13}C NMR, the focus of this dissertation, the spin number S is 1/2 with two sublevels (two spin states).

In the absence of a magnetic field, degeneracy occurs, meaning one energy level corresponds to more than one quantum states. In the presence of a magnetic field, degeneracy breaks, meaning each quantum state corresponds to different energies, known as *Zeeman splitting* (**Figure 1.2B**) [3]. The energy difference between two spin states is defined by

$$\Delta E = h \cdot v_0 = h \cdot \frac{\gamma}{2\pi} \cdot B_0 \tag{1.6}$$

Where v_o is Larmor frequency, h is Planck's constant $(6.63 \times 10^{-34}\ m^2 \cdot kg \cdot s^{-1})$, γ is the gyromagnetic ratio (MHz/T), and B_0 is the magnetic field strength (T). According to Boltzmann distribution, the probability of a nucleus with spin at an energy state is directly related to the energy level by:

$$P(n_+) \propto \exp \frac{-E(n_+)}{kT} \tag{1.7}$$

$$P(n_-) \propto \exp \frac{-E(n_-)}{kT} \tag{1.8}$$

Where k is Boltzmann constant $(1.38 \times 10^{-23}\ kg \cdot s^{-2} \cdot K^{-1})$ and T is temperature in Kelvin.

3

This means that there is an excess of spins at the lower energy state (n_+, referred to as "parallel spins"[6]) than higher energy state (n_-, referred to as "antiparallel spins"). This uneven distribution of particles with spin and their magnetic moments in the presence of magnetic field forms the basis of NMR. Further, the ratio of two spin population is given by

$$\frac{n_+}{n_-} = \exp \frac{E(n_-) - E(n_+)}{kT} = \exp \frac{\Delta E}{kT} \tag{1.9}$$

Polarization is defined as the percentage of the excessive parallel spins over total spin population:

$$\frac{n_+ - n_-}{n_+ + n_-} = \frac{e^{\frac{\Delta E}{kT}} - 1}{e^{\frac{\Delta E}{kT}} + 1} = \tanh\left(\frac{\hbar \gamma B_0}{2kT}\right) \tag{1.10}$$

Where is $\hbar$ is Planck constant in the unit of $J \cdot s/rad$. Based on equation 1.10, polarization is directly proportional to gyromagnetic ratio γ, magnetic field strength B, and inversely proportional to temperature T. Since $\Delta E << kT$, the above equations can be simplified to

$$\frac{n_+}{n_-} \approx 1 + \frac{\Delta E}{kT} \tag{1.11}$$

$$\frac{n_+ - n_-}{n_+ + n_-} \approx \frac{\Delta E/kT}{2 + \Delta E/kT} \approx \frac{\Delta E}{2kT} \tag{1.12}$$

It is evident that when ΔE increases (usually by increasing magnetic field strength B in equation 1.6), the proportion of excessive lower energy spins increases, and the spin system becomes more polarized.

From a microscopic view, the local magnetic field that a spin experiences fluctuates slightly in magnitude and direction due to the wandering of molecules, which are full of magnetic particles such as nuclei and electrons. The long-term[7] effect of this fluctuation is to break the isotropic distribution of spin orientations because molecular wondering is biased towards spin orientation (hence, magnetic moment) parallel with the main magnetic field, creating a macroscopic net magnetization[8]. Overall, a high polarization of the spin system translates into a stronger nuclear magnetization, M_0, and

---

[6]The direction of spin momentums (or axis of rotation) does not actually fully align with the field; if so, spin precession would not happen.

[7]"Long-term" here is in the scale of seconds, as compared to the nano second time scale of spin precession.

[8]This magnetization build-up curve is identical to the longitudinal relaxation recovery curve characterized by equation 1.18 and as shown in Figure 1.3.
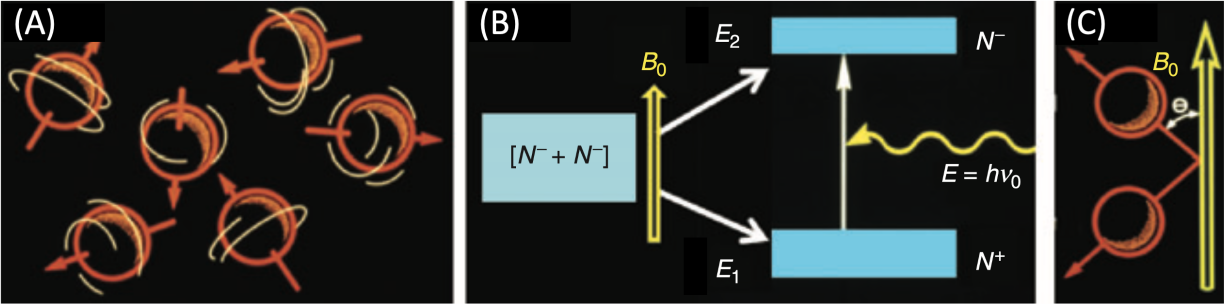
Figure 1.2: (A) Randomly oriented spin axis of rotation and magnetic moment. (B) Zeeman splitting and radiofrequency (RF) excitation: 1/2 spin populations are divided into two energy levels in the presence of the magnetic field; RF pulse at Larmor frequency, v_0, the energy of which is the same as the energy difference between two spin state, can deposit energy into the spin system by stimulating exchanges between the two energy states and temporarily change the spin distributions. (C) As spin system returns to equilibrium, the deposited energy is released in the form for electromagnetic (RF) waves at the Larmor frequency, v_0. Adapted from *Handbook of magnetic resonance spectroscopy in vivo* by Bottomley et al. [4].

thereby, a higher MR signal. In general, M_0 can be computed as:

$$M_0 = \frac{N\gamma^2\hbar^2 S(S+1)B_0}{3kT} \tag{1.13}$$

Where N is the number of nuclei with spin per unit volume. At physiologic temperature (37 °C), M_0 for protons in H_2O is 3.25×10^{-3} $B_0 A/m$. In the following discussion, we will consider how the macroscopic net magnetization moment $\mathbf{M}$[9] is manipulated to produce MR signal.

RF Excitation. We define the direction of the main magnetic field B_0 as longitudinal (z) direction and any directions that are orthogonal to B_0 as transverse (xy) directions; and that at equilibrium, $\mathbf{M}$ aligns with B_0[10]. A RF pulse (also a magnetic field, $\mathbf{B_1}$) applied in the xy-direction at the Larmor frequency (the resonance frequency of spins) can perturb the spin system from its equilibrium, called *excitation*. From a classic perspective, $\mathbf{B_1}$ induces a torque on $\mathbf{M}$ to rotate away from its equilibrium position along the z-direction. This behavior is described by solving the

---

[9]The net magnetization moment $\mathbf{M}$ can be viewed as the sum of the magnetic dipole momentum $\hat{\mu}$ within a given volume. Bold symbols indicate vectors associated with macroscopic behaviors of spin.

[10]This does not suggest that spin magnetic moments $\hat{\mu}$ align with B_0; only the summation of $\hat{\mu}$ do. In fact, the vast majority of spins maintain an angle between their rotation axis and the main field.

following equation[11]:

$$\frac{dM}{dt} = M \times \gamma B_1 \tag{1.14}$$

Moreover, similar to solving equation 1.3, **M** rotates away from z-axis at a frequency defined by $\omega_1 = \gamma B_1$. From a quantum mechanical description, the RF pulse at the Larmor frequency has the energy corresponding to ΔE in equation 1.6 and can stimulate the exchange between two energy states (**Figure 1.2B**).

Following the excitation, the tilted **M** will continue to precess around the z-axis at the Larmor frequency. Because now **M** has a transverse component rotating in the orthogonal plane of B_0, the detection of **M** becomes possible via Faraday's law of induction by the RF coils. The resulting time signal is referred to as *Free Induction Decay* (FID). The degree of rotation of **M** by $\mathbf{B_1}$, called *flip angle*, θ (in radians), can be computed by

$$\begin{aligned} \theta &= \omega_1 \tau & \text{for constant } B_1 \\ &= \int_0^\tau \omega_1(s)ds & \text{for time-varying } B_1 \end{aligned} \tag{1.15}$$

A 90° ($\pi/2$) RF pulse flips **M** onto the transverse plane and results in the largest transverse component, thereby producing the highest signal. A 180° (π) RF pulse inverts **M** and results in no transverse components, thereby producing no signal.

Relaxation. The flipped magnetization vector **M**, including the longitudinal component (M_z) and the transverse component (M_{xy}), will return to its thermal equilibrium following an excitation. This physical process is called *relaxation*. The dominant relaxation mechanism[12] relevant to biological applications is dipole interactions[13].

T_1 **relaxation:** The behavior of longitudinal magnetization M_z following excitation is described by

$$\frac{dM_z}{dt} = -\frac{M_z - M_0}{T_1} \tag{1.16}$$

---

[11]Readers are referred to the Chapter 6 of *Principles of Magnetic Resonance Imaging* by Dwight G. Nishimura for the detailed solutions.

[12]The relaxation mechanisms are diverse and complex. Readers are referred to Chapter 20 of *Spin Dynamics: Basics of Nuclear Magnetic Resonance* by Malcolm H. Levitt

[13]Another relaxation mechanism, chemical shift anisotropy (CAS) is important for ^{13}C T_1 relaxation.

The solution to the equation above is

$$M_z = M_0 + (M_z(0) - M_z)e^{-t/T_1} \qquad (1.17)$$

Where T_1 is the longitudinal relaxation time constant (also known as spin-lattice relaxation time constant). For non-hyperpolarized MR, immediately after a 90° pulse, $M_z(0)$ is 0; hence,

$$M_z = M_0(1 - e^{-t/T_1}) \qquad (1.18)$$

The longitudinal magnetization recover is governed by T_1. The same exponential build-up curve (**Figure 1.3**) applies when B_0 is applied suddenly. The microscopic description of T_1 relaxation is similar to the microscopic explanation for spin polarization introduced before – the molecular wandering induces random fluctuations[14] in local magnetic field by motions of dipoles, enhancing the energy exchange between spin system and the surroundings to disperse the energy deposited by the RF pulses.

$\underline{T_2 \text{ relaxation:}}$ The behavior of the transverse magnetization M_{xy} following excitation is described by

$$\frac{dM_{xy}}{dt} = -\frac{M_{xy}}{T_2} \qquad (1.19)$$

The solution to the equation above (after a 90° pulse, $M_{xy}[0] = M_0$) is

$$M_{xy} = M_0 e^{-t/T_2} \qquad (1.20)$$

Where T_2 is the transverse relaxation time constant (also known as spin-spin relaxation time constant). From a microscopic view, because of local magnetic field fluctuations, it is impossible to maintain the synchrony of spin precession – all that is required is that spins precess at slightly different frequencies at slightly different magnetic fields, regardless of whether they interact with each other or not. Macroscopically, this asynchrony causes the loss of coherence of transverse magnetization, which translates into the decay of MR signal (**Figure 1.3**).

---

[14]The relevant field fluctuations are those with a transverse (xy) component at the spin's resonance frequency, thereby inducing transition between n_+ and n_- populations. In other words, these fluctuations function in a similar manner to RF excitations.
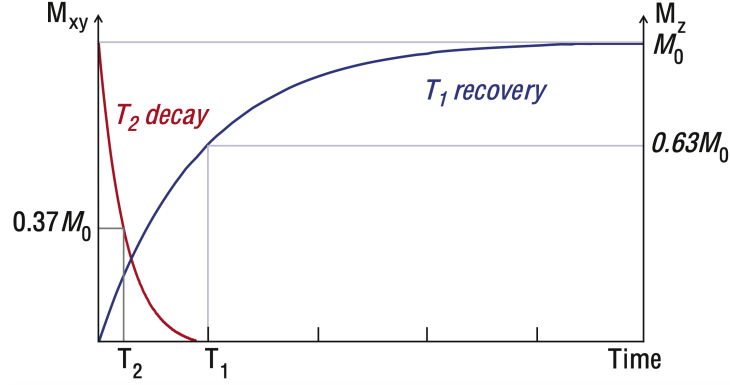
Figure 1.3: Longitudinal (T_1) and transverse (T_2) relaxation behavior of magnetization, where T_1 time constant $>> T_2$ time constant. Adapted from *MRI from Picture to Proton* by McRobbie, D. et al. [5].

Further, the broadening of spin resonance frequencies lead to the peak broadening on NMR spectra and image blurring on MR images. The typical line shape on NMR spectra owing to T_2 relaxation is Lorentzian, characterized by:

$$G(w) = \frac{T_2}{1 + (\omega - \omega_0)^2 T_2{}^2} \tag{1.21}$$

Where ω_0 is the center frequency of the peak and ω is the frequency on the horizontal axis of the NMR spectra. The above equation also shows that the line width at the half-height is $2/T_2$. In practice, the spectral line width is determined by the effective T_2 time constant that accounts for off-resonance sources such as solvent and field inhomogeneity, called T_2^*. Therefore, the spectra line width is commonly used to assess B_0 field homogeneity, where a narrow line width suggests good shimming quality[15].

Various organs and tissues have different T_1 and T_2 time constants, as well as proton nuclei densities, forming the basis of image contrast[16]. It is worth noting that although NMR and MRI only detect M_{xy} in the form of FID, the magnitude of M_{xy} is related to the magnitude of M_z immediately before the RF excitation, which is affected by T_1 relaxation (for example, if spins in a tissue have a long T_1 time constant and slow magnetization recovery, that tissue will generate

---

[15]Shimming is a manual or automatic adjustment of currents in the shimming coils in order to counter-balance the variations in the main magnetic field (B_0) and achieve a relatively homogenous B_0.

[16]Contrast means the difference of tissues/organs are amplified on images to aid distinguishing various anatomic structures and healthy vs. pathologic tissues. Next section will discuss in detail how to control image contrast through pulse sequence design.

a low MR signal and appear dark on the image). That being said, the T_1 and T_2 relaxation are independent processes, and T_1 relaxation usually occurs at a much slower rate than T_2 relaxation (T_1 time constant $>> T_2$ time constant). This is because T_2 relaxation is influenced by field fluctuations in both z- and xy-directions, while T_1 relaxation is primarily influenced by field fluctuations in xy-directions. Moreover, T_1 is field-dependent because a greater energy exchange between n_+ and n_- spins is required at the higher fields. The T_1 of ^{1}H nuclei generally increases as B_0 increases (i.e., the longitudinal relaxation is slower at higher field).However, the T_1 of ^{13}C nuclei generally decreases as B_0 increases, because chemical shift anisotropy (CSA) relaxation mechanism becomes more prominent at higher fields, causing hyperpolarized ^{13}C MR signal decay faster at higher fields.

Chemical Shift. In real-life NMR and MRI, the spin resonance frequency is slightly deviated from the Larmor frequency at a given field strength. This is because orbiting electrons shield nuclei from the main magnetic field (B_0), making spins experience a slightly lower field than B_0; and due to the difference in their chemical environment (i.e., electron densities), this frequency deviation varies among nuclei, called *chemical shift*. The local effective field is defined as:

$$B_{eff} = B_0 - B_{0\sigma} = B_0(1 - \sigma) \tag{1.22}$$

$$\omega_{eff} = \omega_0 - \omega_{0\sigma} = \omega_0(1 - \sigma) \tag{1.23}$$

Where σ is the shielding constant and is characteristic of the chemical environment. Chemical shift δ (in parts per million, ppm) of a sample (denoted by s) is defined with respect to a reference (usually tetramethylsilane, denoted by R) as

$$
\begin{aligned}
\delta &= \frac{\omega_s - \omega_R}{\omega_R} \times 10^6 \\
&= \frac{\sigma_R - \sigma_s}{1 - \omega_R} \times 10^6 \\
&= (\sigma_R - \sigma_s) \times 10^6 \quad \text{because } \sigma_R << 1
\end{aligned}
\tag{1.24}
$$

Chemical shift is responsible for the varying peak locations on NMR spectra. For historical reasons, the frequency on the horizontal axis of NMR spectra *decreases* from left to right (the reference sample at 0 ppm has the *most* electron shielding and the *lowest* frequency). Chemical

shift enables frequency-specific imaging, such as fat/water imaging for the liver and metabolite-specific imaging in hyperpolarized ^{13}C MR.

1.1.2 Imaging Principles

Signal Perspectives. In this section, I will discuss how MR images are generated. The *Bloch equation* describes the behavior of magnetization moment in the presence of magnetic fields[17],

$$\frac{dM}{dt} = M \times \gamma B - \frac{M_x i + M_y j}{T_2} - \frac{(M_z - M_o)k}{T_1} \tag{1.25}$$

where $\mathbf{M} = [M_x, M_y, M_z]^T$, M_x and M_y are transverse magnetizations, M_z is longitudinal magnetization, and i, j, k are vector units. In MRI, there are three types of magnetic fields: (1) B_0, the main static field; (2) $B_1(t)$, RF pulses (an electromagnetic field) used for excitation; (3) $G(t)$, the gradient (spatial- and/or time-varying) fields used for spatial location. Based on the solutions to the Bloch equation with all three fields considered[18], it can be shown that MR signal can be characterized by

$$s(t) = \int_x \int_y m(x, y) e^{-i2\pi[k_x(t) + k_y(t)y]} \, dx \, dy \tag{1.26}$$

where

$$k_x(t) = \frac{\gamma}{2\pi} \int_0^t G_x(\tau) \, d\tau$$
$$k_y(t) = \frac{\gamma}{2\pi} \int_0^t G_y(\tau) \, d\tau \tag{1.27}$$

Equation 1.26 is referred to as *the signal equation* because it captures the fundamental principle of MRI – applying gradient fields to enable spins precessing at different frequencies at different locations, which can be encoded in the time-varying signal $s(t)$; therefore, the problem becomes acquiring appropriate sets of $s(t)$, then inversing the signal equation to solve $m(x, y)$.

---

[17]Because of the ubiquitous application of Block equation, it can be considered as the sources of MRI equations, including equations 1.14, 1.18, 1.19.

[18]Readers are referred to Chapter 5 of *Principle of Magnetic Resonance Imaging* by Dwight G. Nishimura for detailed solutions.

Consider the Fourier transform (FT) of $m(x, y)$,

$$\mathcal{M}(k_x, k_y) = \int_x \int_y m(x, y) e^{-i2\pi(k_x + k_y)} \, dx \, dy \tag{1.28}$$

The FT equation above is exactly the same as the signal equation (1.26)! The significance of this relationship lies in that at any given time, $s(t)$ corresponds to the 2D FT of $m(x, y)$ at certain spatial frequency. In other words, the inverse FT of MR signal $s(t)$ can generate images in real space. Therefore, $s(t)$ can be expressed as:

$$
\begin{aligned}
s(t) &= \mathcal{M}[k_x(t), \; k_y(t)] \\
&= \mathcal{M}[\frac{\gamma}{2\pi} \int_0^t G_x(\tau), \; \frac{\gamma}{2\pi} \int_0^t G_y(\tau)]
\end{aligned}
\tag{1.29}
$$

Where k_x and k_y are spatial frequencies (in the units of cycles/cm). The recorded $s(t)$ is mapped onto a spatial-frequency (Fourier space) as determined by the time integral of gradient wave forms (G_x and G_y), called *k-space*. To form an image, a set of $s(t)$ should be collected with adequate coverage and sufficient sampling in k-space. Based on equation 1.27, this is achieved by controlling the on-off and magnitude of gradient fields and data acquisition timing.

Based on the unit of k-space (1/cm), it can be inferred that k-space and image in real-space have an inverse relationship. By convention, x-direction is commonly referred to as the *readout direction* or the frequency-encoding direction, because the gradient in the x-direction is on during data sampling. The following inverse relationship applies to image and k-space in x-direction:

$$\text{FOV}_x = \frac{1}{\Delta k_x} = \text{sampling rate along } k_x \tag{1.30}$$

$$\delta_x = \frac{\text{FOV}_x}{N} = \frac{1}{\Delta k_x N} = \frac{1}{W_{kx}} \tag{1.31}$$

Where FOV_x is the field of view of the real image, Δk_x is the resolution of the k-space, W_{kx} is the window width of k-space (equivalent to the field of view), and N is the number of k-space lines. The same equations above apply to the y-direction, often referred to as the *phase encoding direction* because the gradient in the y-direction is on before the data sampling begins so that spins can accrue phases.

11
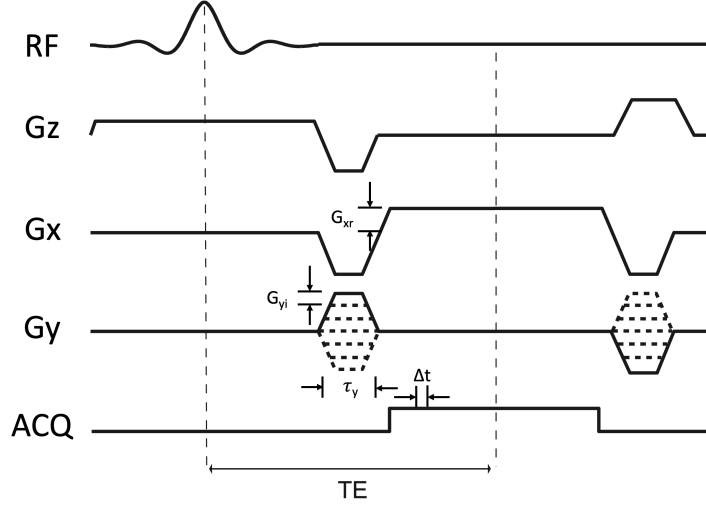
Figure 1.4: Representative 2D gradient echo pulse sequence diagram. RF: radiofrequency pulse; G_x, G_y, G_z: gradients applied in the x-, y-, z-directions, respectively; ACQ: acquisition timing; TE: echo time (the time interval between the center of RF pulse to where an echo is formed). Adapted from *Radiology Key* [6].

Based on equation 1.27, Δk_x and Δk_y can be expressed as

$$\Delta k_x = \frac{\gamma}{2\pi} G_x r \Delta t \tag{1.32}$$

$$\Delta k_y = \frac{\gamma}{2\pi} G_y i \tau_y \tag{1.33}$$

Where G_{xr} is the gradient in the x-direction, G_{yi} is the gradient increments in the y-direction[19]; Δt is the sampling interval in time, τ_y is the phase encoding interval (**Figure 1.4**), neglecting the ramping components in gradient wave forms).

Pulse Sequence and Imaging Contrast. Knowing the relationships above, we can design MR *pulse sequences* – controlled RF excitation, gradient wave forms, and data acquisition timing – to generate MR images with desired contrasts. In general, there are two types of pulse sequences based on the composition of RF pulses and data acquisition timing: *gradient echo* (GRE) and *spin echo* (SE). An echo in MR is a phenomenon where spatial-varying phases are momentarily removed. Echoes are important for acquisition because they have the most signal coherence and strength and should be sampled in the center of k-space. A GRE sequence uses balanced gradient wave forms

---

[19]In conventional 2D imaging, G_y changes with fixed increments for each phase encoding step.
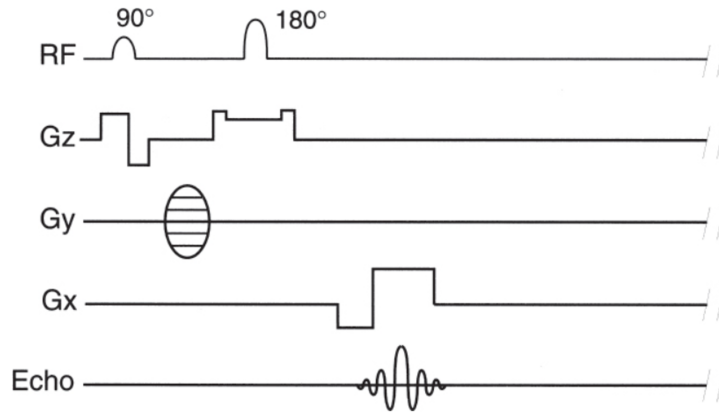
Figure 1.5: Representative 2D spin echo pulse sequence diagram. RF: radiofrequency pulse; G_x, G_y, G_z: gradients applied in the x-, y-, z-directions, respectively. Adapted from *Radiology Key* [6].

to achieve this sampling goal (**Figure 1.4**). However, the spatial-varying phase shifts are not only caused by manually applied gradient; other off-resonance sources, such as B_0 field inhomogeneity and chemical shifts, are not addressed by GRE. Therefore, the FID diminishes at a faster rate than T_2 due to the loss of signal coherence; this reduced relaxation time constant is called T_2^*. In contrast, spin echo sequences have the addition of a 180° RF pulse between phase encoding steps and frequency-encoding readout, as shown in **Figure 1.5**. A SE sequence can not only refocus phase shits caused by gradients, but also the phase shifts caused by other off-resonance sources, leading to more coherent and stronger signal.

Next, I will discuss designing pulse sequences and acquisition parameters to control the image appearance and contrast. From an imaging contrast generation perspective, there are two types of pulse sequences: *saturation recovery* and *inversion recovery*[20]. Both sequences produce *steady-state*[21] longitudinal magnetization M_z before each RF excitation (**Figure 1.6**), a requirement for 2D conventional MRI [7]. As discussed in the previous subsection, a set of MR signal, $S(t)$, need to be collected and mapped onto the k-space. If magnetization magnitudes immediately before excitation vary across k-space lines, there will be a weighting factor on the k-space, leading to image distortions and blurring in the real space. Therefore, dummy scans (excitation but no readouts)

---

[20]Inversion recovery (IR) is not discussed in detail here because it was not used in this dissertation. Briefly, IR uses the addition of 180° pulses to invert the magnetization before excitation and sampling, which increases the dynamic range of longitudinal magnetization and improves T_1 contrast. IR can also be used to measure T_1 time constants.

[21]Steady-state means a variable appears constant despite the dynamic changes. In MR, it means that the magnetization at a given point within the TR is constant from one repetition to the next.

are often used to prepared steady-state magnetization to avoid the signal weighting factors.

The basic saturation recovery sequence consists of a series of 90° pulses separated by repetition time (TR, the time interval between initial excitation RF pulses) as shown in **Figure 1.6**. The intensity of images obtained from a saturation recovery sequence is characterized by

$$I(x,y) = K\rho(x,y)[1 - e^{-TR/T_1(x,y)}]e^{-TE/T_2(*)(x,y)} \tag{1.34}$$

Where K is a catch-all gain term to take into account the coil sensitivity and other acquisition variabilities, ρ is nuclei density, and T_2^* applies to GRE sequences while T_2 applies to SE sequences.

Based on equation 1.34, it can be inferred that T_1 contrast is controlled by TR, whereas T_2 contrast is controlled by TE. In general, GRE sequences have short TRs by design, so the difference in T_1 recovery rate of varying tissues is accentuated on the images, called T_1 *weighting.* In contrast, SE sequences generally have longer TRs due to the inclusion of 180° RF pulses and by intentional design, leading to a higher recovery of M_z before the subsequent RF excitation. Therefore, SE images are less weighted by T_1 but heavily weighted by the difference in T_2 of varying tissues, called T_2 *weighting.* If TE was chosen to be $<< T_2$ to minimize T_2 weighting, these spin echo images are *proton density-weighted.*

GRE sequences are generally faster due to their short TRs and are commonly used to produced T_1-weighted images with high spatial coverage, such as standard anatomical images and dynamic contrast enhanced (DCE) imaging[22]. SE sequences are generally slower due to their longer TRs, but they are the most prevalent pulse sequences in conventional MRI. This is because SE signal is generally higher (due to the higher effective M_0 than GRE sequence and refocus pulses mitigating off-resonance effects), has higher superior image quality and flexibility in contrast generation, and is sensitive in detecting pathologies due to its ability to generate T_2-weighted images[23].

In reality, a 90° excitation pulse is rarely used because of the long time required for M_z to recover. Instead, partial saturation recovery with small flip angles are commonly used and its

---

[22]DCE uses GRE sequence to characterize the T_1 shortening effects of Gadolinium-based contrast agents and takes advantage of the fast scan time of GRE to achieve high temporal resolutions.

[23]Inflammation and edema are common tissue-level pathological changes in disease. They are characterized by an increase in free water, which has a longer T_2, and a reduction in protein-bound water, which has a shorter T_2. Therefore, these pathologies will appear hyperintense (bright) on SE images.
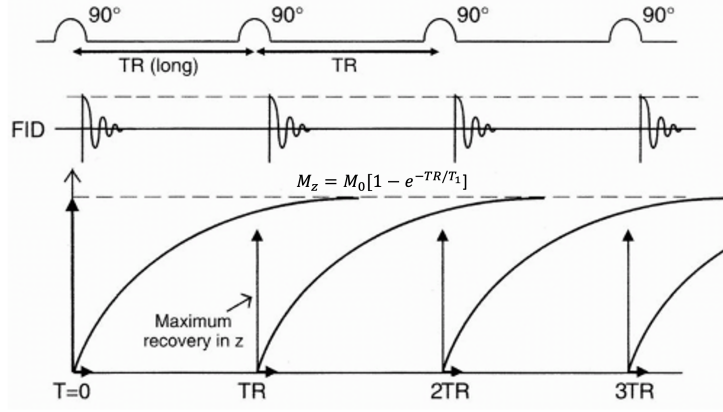
Figure 1.6: A representative saturation recovery pulse sequence: a string of 90° pulses separated by repetition time (TR), leading to steady-state longitudinal magnetization across repetitions. Adapted from *Radiology Key* [8].

image intensity is characterized by[24]

$$I(x,y) = K\rho(x,y)\frac{[1 - e^{-TR/T_1(x,y)}]\sin\theta}{1 - e^{-TR/T_1(x,y)}\cos\theta}e^{-TE/T_2(*)(x,y)} \tag{1.35}$$

Where θ is the flip angle. When θ is 90°, the equation above is the same as equation 1.34. The longitudinal magnetization curve for partial saturation recovery is similar to **Figure 1.6**, except that the longitudinal relaxation immediately after RF pulses is greater than zero. The flip angle can be chosen to maximize the steady-state signal in equation 1.35 for a given TR and T_1:

$$\theta_E = \cos^{-1}(e^{-TR/T_1}) \tag{1.36}$$

This optimized flip angle is called *Ernst angle*, which can lead to a maximal steady-state signal of $M_0\sqrt{(1 - e^{-TR/T_1})/(1 + e^{-TR/T_1})}$.

Images of diagnostic values must have sufficient signal-to-noise ratio (SNR) to delineate structures and lesions. The trade-off between SNR and spatial resolution is an important consideration when designing acquisition parameters. In general, the relationship between SNR and acquisition

---

[24]Readers are referred to Chapter 7 of *Principle of Magnetic Resonance Imaging* by Dwight G. Nishmura for detailed derivation.

parameters is described by

$$\text{SNR} \propto \rho K \Delta x \Delta y \Delta z \sqrt{\text{Number of Averages}} \tag{1.37}$$

Where ρ is the spin density, K is a catch-all gain factor that accounts for variations in pulse sequences and coil sensitivities, $\Delta x, \Delta y, \Delta z$ are spatial resolution in x-, y-, z-direction, respectively. It is important to note the square root relationship between SNR and Number of Average (also referred to as Number of Excitations, or NEX), which shows that increasing scan time or repetitions has a diminished return in SNR.

The fundamental principles of MRI introduced in this section are essential to the understanding of advanced MRI techniques such as echo planar imaging (EPI), diffusion-weighted imaging (DWI), balanced steady-state free precession (bSSFP) that are routinely use in the clinic. Readers are referred to *Handbook of MRI Pulse Sequences* by Bernstein et al. for discussions on the advanced sequences [9].

1.2 Hyperpolarized MR for Molecular Imaging

Hyperpolarized (HP) MR is an emerging molecular imaging technique with potential to study *in vivo* biological processes non-invasively. ^{13}C-labeled substrates, such as [1-^{13}C]pyruvate, are mixed with a polarizing agent (usually a stable radical with unpaired electrons, called electron paramagnetic agent, or EPA) in a dedicated polarizer (with sub-Kelvin temperature, high magnetic field, and GHz microwave source) to increase the polarization of ^{13}C spin system by more than 10,000-fold [10]. After hours of preparation, the HP substrates are rapidly dissolved into an injectable solution[25], and then intravenously administered into a living system. This order-of-magnitude signal enhancement, along with the large range of chemical shifts of ^{13}C-labeled metabolites, provides the sensitivity for MRI to monitor the distribution and the metabolic conversion of injected ^{13}C-labeled substrates in real time. These quantitative molecular imaging markers can inform on metabolic activities and physiologic processes, thereby potentially providing non-invasively assessments of cancer aggressiveness, disease burden, and therapeutic response. In this section, I will introduce the physics, imaging considerations, biological and clinical applications of HP ^{13}C MR.

---

[25]A detailed description of the dissolution process is presented in Chapter 4.
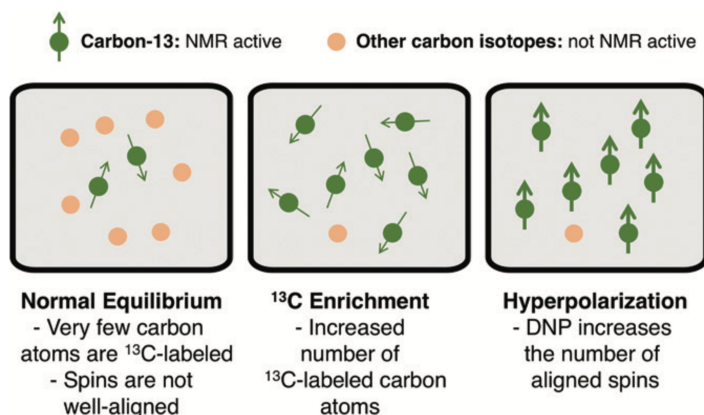
Figure 1.7: Schematic diagram of ^{13}C hyperpolarization. Adapted from Wang et al., 2019 [13].

1.2.1 Hyperpolarization Physics and Imaging Approach

Dynamic Nuclear Polarization. NMR is generally considered to be a low-sensitivity technique, given that only few in a million spins contribute to the NMR signal. This low sensitivity can be overcome by high concentration and large sample volume, as in the case of clinical MRI[26], but limits the application of NMR to study biological processes involving low-concentration metabolites. Several hyperpolarization techniques have been developed to increase the sensitivity of NMR through perturbing spins from their thermal equilibrium to increase the fraction of parallel spins (n_+, lower energy state), with dynamic nuclear polarization (DNP) technique being one of most the commonly used hyperpolarization methods (**Figure 1.7**)[10]. There are two polarization-enhancing factors in DNP: 1) the extreme low temperature (< 1K) increases polarization level by 300-fold (according to equation 1.10), and 2) microwave irradiation transfers polarization from electron spins to nuclear spins. During DNP, the nuclei-electron mixture is irradiated by a continuous microwave around the Larmor frequency of the electron[27]. The microwave irradiation coupled with the low temperature and the high magnetic field results in the electron spin ensemble reaching a high steady-state polarization (usually over 99% at typical DNP conditions). Through a combination of relaxation events and level mixing between electron spins and nuclear spins, including *solid effect*, *cross effect*, and *thermal mixing*, the nuclear spin ensemble is hyperpolarized (**Figure 1.8**) [11, 12]. These physical mechanisms are described qualitatively in the section.

---

[26]The concentration of ^{1}H is over 100M in water, the predominant molecule in living systems.

[27]Note that the differences between electron spin energy levels are 3 orders of magnitude larger than the differences between nuclear spin energy levels, i.e., ω(electrons) $>>$ ω(nuclei).
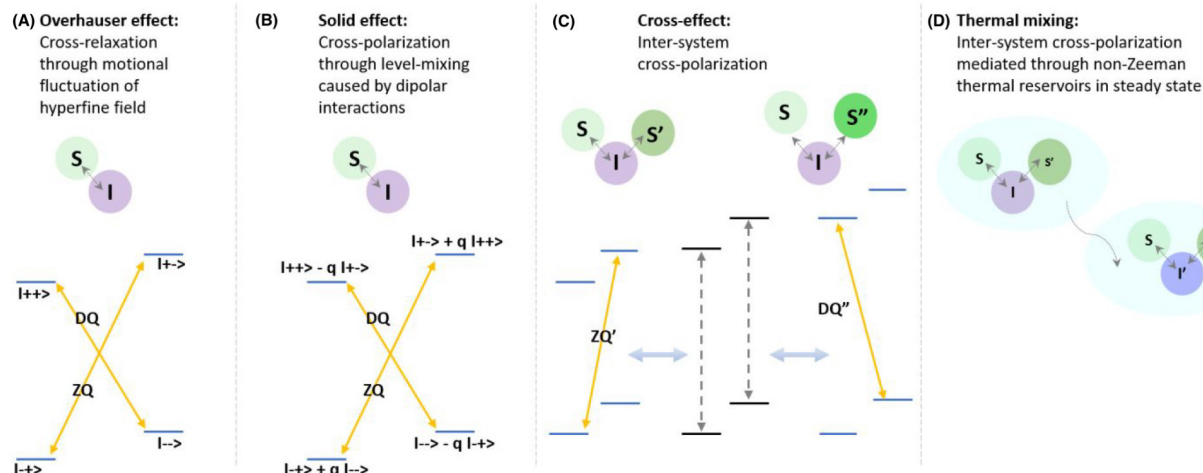
Figure 1.8: Schematic of four broad classes of hyperpolarization mechanisms. S, electron spin; I, nuclear spin; DQ, double quantum; ZQ, zero quantum. Note that the Overhauser effect is only applicable in liquid state, while the other three mechanisms are relevant in the solid state dynamic nuclear polarization (DNP). Adapted from Abhyankar and Szala, 2021 [12].

Solid effect: The electron spin (S) and nuclear spin (I) can form a dipolar interaction (a two-spin system) if electrons are relatively isolated, such as when EPA concentrations are low. This dipolar spin interaction allows simultaneous flipping of nuclear and electron spins, driven by microwave irradiation with energies of $\hbar(w_S \pm w_I)$. In other words, microwave irradiation at the sum or difference frequency of the electron and nuclear Larmor frequencies induce the coupled flipping of electron-nuclear spins. This "flip-flop" action is followed by subsequent rapid relaxation of electron spins to equilibrium, leaving nuclear spins in "flipped" state due to their slow relaxation rates at solid-state and low-temperature conditions (**Figure 1.8B**). This process is called *solid effect*, which requires narrow electron paramagnetic resonance (EPR) line widths in order to selectively perform "positive" or "negative" enhancement[28] [14]. Although the description of solid effect suggests that only nuclear spins in close contact with electrons are polarized, nuclear spins distribute their polarization homogeneously to their neighboring nuclear spins via *spin diffusion*, thereby transferring the high polarization from electrons to the entire nuclear spin ensemble [15]. Finally, the solid effect is less efficient at higher magnetic fields [12].

Cross Effect and Thermal Mixing: When EPA concentrations are sufficiently high, a three-spin system can be formed, electron-electron-nuclei, which is the physical framework for the cross

---

[28]Double Quantum (DQ) transitions result in positive enhancement of nuclear polarization, while Zero Quantum (ZQ) transitions result in negative enhancement (Figure 1.8B).

effect (CE) and thermal mixing (TM), two interrelated mechanisms. The concept of *spin temperature* is introduced here: according to equation 1.10, a polarization level is inversely associated with temperature; this means a lower spin temperature is associated with a higher polarization.

CE and TM rely on the broad EPR line width of EPA: ideally, the EPR line width needs to be greater than nuclear Larmor frequency, ω(nuclear)[16]. When the sample is irradiated with microwave at a frequency of $\omega = \omega$(electrons) $+ \Delta$, where Δ could be $>$ or < 0, $\hbar\ \omega$(electrons) is absorbed by the electron Zeeman reservoir and the remaining $\hbar\Delta$ is absorbed or emitted by the electron spin-spin dipolar reservoir, lowering its spin temperature. Because EPR line width $>$ ω(nuclear), the electron spin-spin dipolar reservoir is coupled with the nuclear Zeeman reservoir, allowing the spin transitions depicted in **Figure 1.7C** to enhance nuclear polarization. Eventually, all nuclear spin ensembles (including ^{13}C, ^{15}N, ^{1}H, and more) reach the same spin temperature, as depicted in **Figure 1.7D**. The detailed distinctions in physical mechanisms between CE and TM are beyond the scope of this dissertation, but a few application differences between the two is summarized below.

Generally, CE requires an imhomogeneously broaden EPR line width, a higher-power microwave irradiation, and a stronger electron-electron dipolar interaction; can only yield polarization transfer between nuclei with the same gyromagnetic ratio (such as ^{13}C to ^{13}C); and is the dominant mechanism at higher than sub-Kelvin temperature. In contrast, TM requires high magnetic fields, extreme low temperatures (< 4 K), homogeneously broaden EPR line width; and can yield multi-nuclear hyperpolarization (such as ^{1}H and ^{13}C) [12, 15]. The dominant DNP mechanism is determined by a combination of factors, including temperature, main field strength, microwave frequency and power, and the type and the concentration of EPA; and more than one mechanism can operate simultaneously [17, 18]. The EPA concentrations and microwave frequency and power used in this dissertation were chosen empirically to optimize solid-state polarization as monitored by the build-in NMR spectrometer in the polarizer and the liquid-state polarization as measured by external NMR spectrometers. The HP probe formulation strategy is discussed in Chapter 4.

Imaging Approach. The HP MR signal is short-lived as the spin ensemble will start to relax back to thermal equilibrium once the microwave irradiation is stopped. Based on equation 1.18,
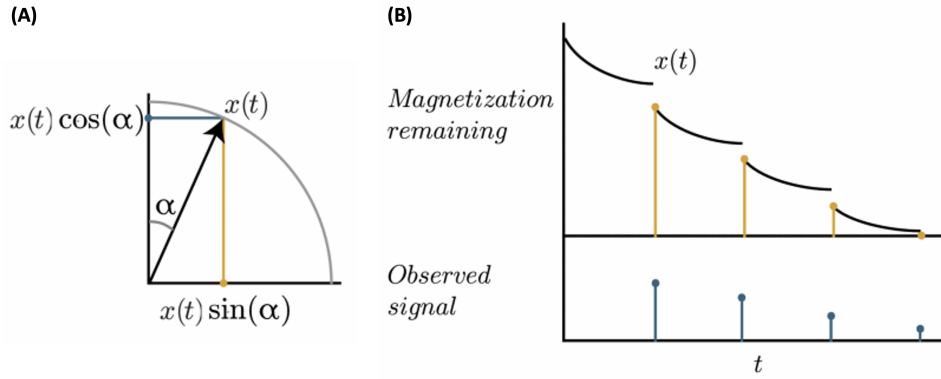
Figure 1.9: (A) Illustration of the effect of flip angles. (B) The influence of RF excitation and T_1 relaxation on the hyperpolarized magnetization and signal (a hybrid discrete-continuous model). Adapted from Maidens et al., 2016 [19].

the longitudinal magnetization of HP compounds can be characterized by

$$M_z(t) = M_{z,HP} \cdot e^{-t/T_1} \tag{1.38}$$

Where $M_z(0) = M_{z,HP} >> M_0$ and $M_{z,HP}$ is the initial HP magnetization. The equation above shows that the decay of HP magnetization is governed by T_1 relaxation. Similarly, the hyperpolarized signal is non-renewable after RF excitations. Therefore, the HP magnetization (M_z) and the resulting MR signal (M_{xy}) are characterized by

$$M_z(t)[N] = M_{z,HP} \cdot e^{-t/T_1} \cdot \cos^{N-1}\theta \tag{1.39}$$

$$M_{xy}(t)[N] = M_{z,HP} \cdot e^{-t/T_1} \cdot \cos^{N-1}\theta \cdot \sin\theta \tag{1.40}$$

Where t represents the time since the beginning of acquisition, N represents the Nth RF excitation in the series, and θ is the flip angle. The effect of RF excitation and T_1 relaxation on HP magnetization and the resulting signal dynamics is illustrated in **Figure 1.9** [19].

Sequence design: Compared to the snap-shot nature of conventional ^{1}H anatomic imaging, HP ^{13}C MR requires dynamic imaging of multiple ^{13}C-labeled metabolites of different resonance frequencies. Therefore, HP ^{13}C MR acquisitions need to be highly efficient to achieve adequate SNR, spectral separation, as well as temporal and spatial resolution for accurate quantification of metabolic imaging metrics. Here, I will briefly review three broad classes of acquisition strategies.

For more in-depth discussions on HP ^{13}C MR imaging acquisition methods, readers are referred to a recent review paper by Gordon et al. [20].

Localized MR spectroscopy, also known as Chemical Shift Imaging (CSI) or MR Spectroscopic Imaging (MRSI), is perhaps the most intuitive method for HP ^{13}C MR acquisition. As metabolites appear as various peaks on the spectra, no prior knowledge about the spectral composition other than spectra width is required to initiate the study. In addition to its relatively straightforward data presentation, spectroscopy requires less stringent RF pulse designs due to its wide-band excitation and less stringent gradient requirements due to the lack of frequency encoding steps. However, spectroscopy is an inherently slow acquisition method due to its need of extensive phase encoding steps to achieve spatial localization and spectral encoding to differentiate various metabolites (**Figure 1.10A**). For example, a 2D CSI acquisition of one slice of an 8-by-8 matrix requires 64 RF excitations, which not only prolongs the total scan time but also depletes the nonrenewable HP signal. Therefore, fast readout trajectories, such as echo planar [21], spiral [22], or concentric ring readouts [23] (**Figure 1.10B**), and acceleration techniques, such as compressed sensing [24] or parallel imaging [25], are often used in dynamic HP ^{13}C MR spectroscopy studies to improve the sampling speed and the spatial resolution and coverage.

The alternative to spectroscopy is metabolite-specific imaging approach that generates images where the intensity corresponds to the HP signal of metabolites. Compared to spectroscopy, the imaging approach is generally faster (by reducing the number of excitations and applying spatial encoding during readout), thereby allowing higher spatial resolution and mitigating T_1 signal decay. Moreover, the imaging approach has more streamlined quantification compared to spectroscopy, as magnitude image can be directly visualized and quantified. The fast readout trajectories and acceleration techniques mentioned in the preceding paragraph can also be employed here to further improve acquisition speeds. Additionally, fast spin echo (FSE) sequences and balanced steady state free precession (bSSFP) sequences have been used in HP ^{13}C MRI studies, for their efficient utilization of transverse magnetization and their intrinsic SNR advantages. A hybrid sequence of FSE and echo planar imaging (EPI) was used in the work presented in Chapter 3, and a bSSFP sequence was used in the work presented in Chapter 4. The main challenges for metabolite-specific imaging are the need for spectral-spatial RF pulses that selectively excite the resonance frequency of a specific metabolite (i.e., a narrow excitation bandwidth) within a target volume [27] and the
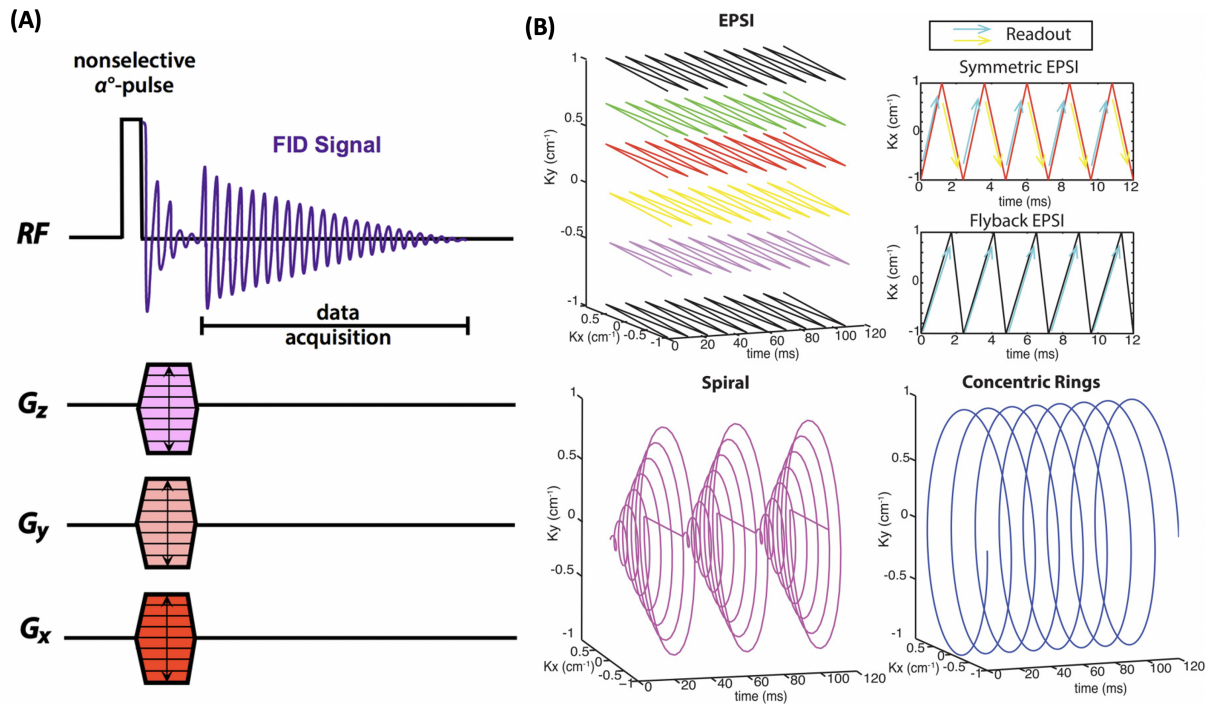
Figure 1.10: MR Spectroscopic Imaging (MRSI) sequences. (A) A representative 3D CSI sequence using nonselective volume RF excitation and stepped phase-encoding gradients along x, y, z directions. A 2D CSI uses slice-selective RF excitation and stepped phase encoding along x, y directions. Adapted from Allen D. Elster, MRIquestions.com [26]. (B) K-space trajectories of EPSI, spiral, and concentric rings spectroscopic imaging: the arrows illustrate the readout directions for both symmetric EPSI and flyback EPSI; for symmetric EPSI, different color represent even/odd echoes for reconstruction. Adapted from Jiang et al., 2016 [23].

demanding requirement of gradient performance for spatial encoding due to the low gyromagnetic ratio of ^{13}C.

Another acquisition method is model-based spectroscopy approach, such as iterative decomposition with echo asymmetry and least squares estimation (IDEAL), where multiple echoes are acquired, and the signal intensity of each metabolite is reconstructed using prior knowledge of chemical shifts [22]. The acceleration lies in that fewer echoes are needed due to this prior knowledge. However, the echo spacing needs to be carefully chosen, which becomes challenging when the spectral region is crowded with multiple resonances.

Parameter design: After the selection of an acquisition method, sequence parameters need to be chosen wisely to ensure efficient utilization of HP signal and optimal detection of biological processes. A variable flip angle (VFA) scheme is often used to compensate for the loss of magnetization due to T_1 relaxation and previous RF excitations [28]. By progressively increasing the flip angle, the VFA approach aims to achieve a relatively constant signal amplitude across k-space encodings of a single slice or across a dynamic acquisition series. The main drawback for the VFA approach is its sensitivities to inhomogeneous B_1 fields and the timing of bolus arrival [29]; therefore, it should ideally be used in conjunction with advanced B_1 calibrations or with smaller RF coils with good B_1 filed homogeneity. Moreover, the effect of VFA on the signal of downstream metabolic products must be addressed in the metabolic quantification algorithm [19, 30].

While every effort should be made to decrease the time interval between the injection product leaving the polarizer and its administration, acquisition delays after the start of injection, ranging from a few seconds to half a minute, could preserve HP magnetization and allow better detection of downstream metabolites. However, longer acquisition delays could cause missing the wash-in phase of the bolus characteristics. A recent study demonstrated the feasibility of using bolus tracking techniques to automatically optimize the acquisition timing [31]. Additional consideration of the trade-offs among the SNR per voxel, spatial resolution, and temporal resolution should be made when designing acquisition parameters. In practice, exploratory studies should be performed to better understand the hemodynamics of the subject and the metabolic profile of the target organ system; this empirical data will guide the design of optimal acquisition parameters.

1.2.2 Imaging Tumor Metabolism and Microenvironment

Metabolic reprogramming is a hallmark of cancer development [32, 33]. In particular, the up-regulation of aerobic glycolysis (Warburg effect), lactate production from pyruvate, and lactate acid efflux[29] could be an adaptation of cancer cells in response to the increased energy demand [34]. The exported lactic acid contributes to the acidification of the extracellular space [35], and could be recycled as fuels by neighboring cells that are capable of oxidative phosphorylation, known as *lactate shuttle theory* [36, 37]. The enhanced glycolysis provides carbon sources for various anabolic processes to support cell proliferation [38]. For instance, the glycolysis pathway can be diverted to pentose phosphate pathway (PPP) to produce nicotinamide adenine dinucleotide phosphate (NADPH), which provides reducing equivalents for biosynthesis of nucleotide and amino acids in highly proliferating cells. Moreover, the pyruvate-to-lactate conversion is coupled with the interconversion between the nicotinamide adenine dinucleotide pair ($NADH/NAD^+$), a critical cellular redox capacity modulator [39]. Recent research found the up-regulation of glycolysis in cancer was primarily driven by the increased demand of NAD^+ for excessive oxidative reactions in cancer cells, rather than the demand of adenosine triphosphate (ATP) [40]. The metabolic reprogramming involving lactate production and efflux aids in cancer cell survival, tumor growth, and metastasis [41, 42, 43]. Clinically, increased tumor lactate production has been found to be associated with poor prognosis and therapeutic resistance [44, 45, 46] and has been investigated as a potential therapeutic target [47, 48].

Angiogenesis is another hallmark of cancer development that facilitates the delivery of oxygen and nutrients to the tumor and the removal of metabolic waste from the tumor [32]. For instance, intratumoral microvascular density has been shown to be a prognostic factor in cancer [49]. Imaging plays an important role in assessing angiogenesis: increased vascularity is characterized by early, focal enhancement on dynamic contrast enhanced (DCE) MR scans, which has been incorporated into standard clinical prostate MR exams and reporting systems [50]. Paradoxically, tumor perfusion can be *defective* in aggressive tumors as newly formed vessels are premature, leaky, and tortuous with excessive, irregular branching [51, 52]. As a result, the tumor blood flow is heterogeneously distributed, causing certain regions to exhibit decreased blood flow, increased interstitial pressure,

---

[29]Note that pyruvate-to-lactate conversion consumes a H^+ rather than produces acid; the H^+ that is co-exported with lactate anion out of the cell is produced by the upstream glycolysis and ATP hydrolysis.

and inefficient oxygen and nutrient exchange [32, 53] and eventually, the vascular supply cannot meet the demand of cancer growth.

Hypoxia is a key feature of many human cancers and has been implicated as an important biological modulator of cancer aggressiveness and treatment response [54, 55, 56]. Hypoxia is associated with impaired diffusion caused by increased cellularity and decreased perfusion caused by defective vessels. Moreover, hypoxia drives glycolysis via hypoxia-induced factor 1-α (HIF1-α), a master transcription regulator [34]. The relationship among metabolism, perfusion, and hypoxia has been studied in locally advanced breast cancer [57, 58], advanced cervical carcinomas [59], and lung cancer [60] using multi-probe positron emission tomography (PET): the phenomena of perfusion-metabolism mismatch – high metabolism relative to low perfusion – has been found to be associated with treatment resistance and poor clinical outcomes. In a recent preclinical study, a similar metabolism and perfusion phenotype was observed in a transgenic prostate cancer mouse model using the combined HP ^{13}C pyruvate and urea MR [24].

Tumor microenvironment consists of a heterogeneous group of cancer cells, host cells (such as fibroblasts and immune cells), extracellular matrix and molecules, and the surrounding vasculature [61]. The biological focus of this dissertation is the interplay among metabolism, perfusion, hypoxia, and redox capacity (**Figure 1.11**). In addition to biological factors discussed above, the distribution of the injected probe is affected by the volume and compactness of the extracellular space. Hence, HP ^{13}C MR signal could potentially inform on tissue cellularity, stroma density, and matrix stiffness, which are highly relevant to solid tumor progression, such as pancreatic cancer [62, 63]. Moreover, the pathological features in tumor vasculature and extracellular space affect drug delivery and therapeutic responses [64], and the relationship between perfusion and stromal density have been studied using contrast-based perfusion imaging techniques [65]. Finally, the tumor microenvironment, including vasculature and extracellular matrix, is modulated by therapies such as radiation [66], making it desirable imaging target for evaluating therapeutic responses.

In this dissertation, three HP ^{13}C MR imaging probes and techniques were systemically investigated: dehydroascorbic acid (DHA) to image redox capacity, pyruvate to image glycolytic metabolism, and urea to image tissue perfusion and microenvironment. Specifically, I performed technical developments to optimize the probe formulations, imaging acquisition methods, and data analysis frameworks; performed preclinical validations to demonstrate the usefulness of these imag-

25
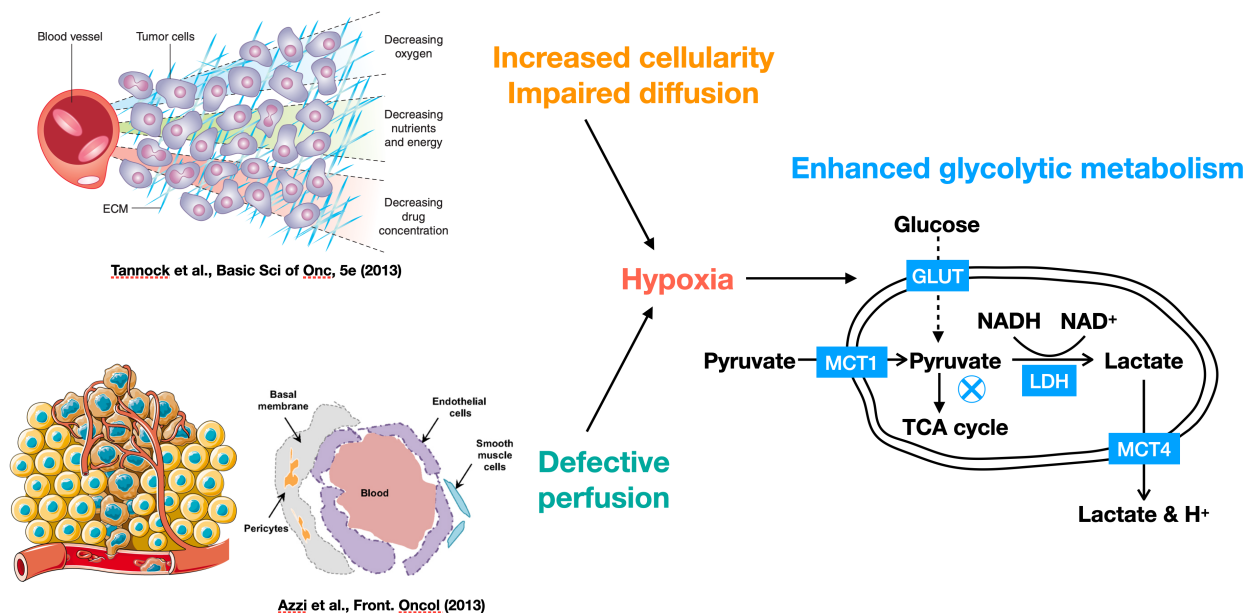
Figure 1.11: The interplay among tumor metabolism, perfusion, hypoxia, extracellular space, and redox capacity. The tissue cellularity increases during tumor proliferation, leading to impaired diffusion of oxygen and nutrients. Tumor progression requires angiogenesis to meet increased demands of oxygen and nutrients; however, the newly formed vasculature is leaky and immature, leading to defective perfusion. Together, these morphologic and physiologic changes cause hypoxia, an important biological modulator that further upregulates the already enhanced glycolytic metabolism. As the result of metabolic reprogramming, cancer cells prefer glycolysis over oxidative phosphorylation via the TCA cycle, even in the presence of oxygen. Pyruvate, the product of glycolysis or injected exogenously as an imaging probe, is predominately converted into lactate, which is subsequently co-exported out of the cell with proton (H^+), leading to acidification of the extracellular environment. The pyruvate-to-lactate conversion is also modulated by cellular redox capacity via the nicotinamide adenine dinucleotide pair (NADH/NAD$^+$). Abbreviations: GLUT, glucose transporter; MCT, monocarboxylate transporter; LDH, lactate dehydrogenase; TCA, tricarboxylic acid. Top figure on the left was adapted from Tannock et al., 2013 [67]; bottom left figure was adapted from the templates in ChemDraw software, and bottom right figure was adapted from Azzi et al., 2013 [68].

ing probes in animal models; and finally, performed translational studies to obtain regulatory approvals to conduct clinical investigations of the combined HP ^{13}C pyruvate and urea MR. The multi-probe imaging approach presented in this dissertation highlights the unique capability of HP ^{13}C MR and could potentially provide a comprehensive evaluation of intertwined biological processes in health and disease.

1.2.3 Path to Clinical Translation

HP [1-^{13}C]pyruvate is the most studied HP ^{13}C probe to date. Motivated by the promising preclinical evidence, extensive efforts are being made to translate this technology for clinical use. As of 2021, more than 400 HP [1-^{13}C]pyruvate MR exams have been performed at 10 centers around the world to evaluate its utility in assessing prostate cancer [69], brain tumors [70], cardiac metabolism [71], breast cancer [72], renal tumors [73], and more. Additionally, HP [2-^{13}C]pyruvate has also been used to investigate mitochondrial metabolism in the human brain [74]. The final two chapters of this dissertation aim to translate the first non-pyruvate probe, HP ^{13}C urea, to clinical research. Despite these advances, several challenges need to be addressed in the clinical translation process of HP ^{13}C MR.

From a scientific perspective, a thorough understanding of imaging mechanisms gained from basic science research and clinical trials is essential for the technique to be adopted for routine clinical use. The measured HP ^{13}C pyruvate-to-lactate conversion rate has been found to be affected by membrane transporter expressions (monocarboxylate transporters, MCTs) [75, 76], the enzymatic activity (lactate dehydrogenase, LDH) [24, 77], and the availability of co-factors (NADH) at the cellular level [78, 79, 80, 77]; perfusion and the volume of probe distribution at the tissue level [24]; variabilities in cardiovascular and respiratory activities at the whole body level [75]. Recent research even suggested that the injected HP ^{13}C pyruvate doses were in excess to the endogenous pool and could inhibit the lactate production rate [81]. Moreover, assumptions are included in kinetic models to improve their generalizability, reproducibility, and stability, such as assuming the pyruvate-to-lactate conversion is a first-order reaction (meaning that the kinetic rate is linearly associated with the concentration of pyruvate) and setting fixed relaxation rates for metabolites [30]. Understanding the relevant biological underpinnings and the quantification framework is essential for interpreting HP ^{13}C pyruvate MR findings.

From a practical perspective, HP ^{13}C MRI is high-end imaging exam that requires not only the state-of-the-art MR scanner but also a dedicated polarizer priced at the million-dollar range. Moreover, a HP ^{13}C MRI study requires the interprofessional collaboration among physicians, scientists, engineers, pharmacists, technologists, and nurses that is only feasible at academic medical centers. Therefore, streamlining the HP ^{13}C MR imaging probe production process, acquisition protocols, and quantifying and reporting imaging data would be crucial to the dissemination of the technology for wider use. Finally, as indicated in a recent white paper [82], the evidence of clinical utility in Phase II and III clinical trials will be required for the Food and Drug Administration (FDA) to approve HP ^{13}C pyruvate MR for routine clinical use.

Chapter 2: Imaging Glutathione Depletion in the Rat Brain Using Ascorbate-Derived Hyperpolarized MR and PET Probes

Abstract: Oxidative stress is a critical feature of several common neurologic disorders. The brain is well adapted to neutralize oxidative injury by maintaining a high steady-state concentration of small-molecule intracellular antioxidants including glutathione in astrocytes and ascorbic acid in neurons. Ascorbate-derived imaging probes for hyperpolarized ^{13}C magnetic resonance spectroscopy and positron emission tomography have been used to study redox changes (antioxidant depletion and reactive oxygen species accumulation) *in vivo*. In this study, we applied these imaging probes to the normal rat brain and a rat model of glutathione depletion. We first studied hyperpolarized [1-^{13}C]dehydroascorbate in the normal rat brain, demonstrating its robust conversion to [1-^{13}C]vitamin C, consistent with rapid transport of the oxidized form across the blood-brain barrier. We next showed that the kinetic rate of this conversion decreased by nearly 50% after glutathione depletion by diethyl maleate treatment. Finally, we showed that dehydroascorbate labeled for positron emission tomography, namely [1-^{11}C]dehydroascorbate, showed no change in brain signal accumulation after diethyl maleate treatment. These results suggest that hyperpolarized [1-^{13}C]dehydroascorbate may be used to non-invasively detect oxidative stress in common disorders of the brain.

2.1 Introduction

Reactive oxygen species (ROS) are expected products of oxidative metabolism, and must be tightly regulated in the normal brain. Several pathways are required to maintain redox homeostasis, in particular the glutathione-glutaredoxin and thioredoxin-thioredoxin reductase systems [83]. These systems maintain high steady-state concentrations of small-molecule antioxidants including reduced glutathione (GSH) and vitamin C (VitC). Glial cells harbor a high concentration (in the mM range) of GSH, while neurons capture the majority of the VitC in the central neural system [84, 85]. Although the reasons for this partitioning are only partially understood, these antioxidants are considered critical in both health and disease. Oxidative stress, marked by increased ROS production and GSH consumption, is implicated in various neurodegenerative and neuropsychiatric disorders such as Parkinson's disease, Alzheimer's disease, multiple sclerosis, and schizophrenia [86, 87]. Therefore, non-invasive evaluation of brain antioxidants could provide critical insights into these disease processes.

The relationship between VitC and its oxidized counterpart dehydroascorbic acid (DHA) has been extensively studied. In contrast to VitC, which is slowly imported via sodium-dependent vitamin C transporter-2 (SVCT-2) and maintained at high steady-state concentrations in the brain [88], DHA is a transient species with remarkably different transport properties despite its structural similarity to VitC. DHA readily crosses the blood-brain barrier (BBB), actively transported by glucose transporters (GLUTs) as shown in **Figure 2.1a** [89, 90, 91]. Once transported into cells, DHA undergoes a GSH-dependent, two-electron reduction to VitC, catalyzed by redox enzymes including glutaredoxin, omega-class glutathione transferases and protein-disulfide isomerase [92, 93, 94, 95]. This GSH-dependent conversion is one of the motivations for studying ascorbate-derived imaging agents, whose interconversion depends on both the concentration of GSH and the presence or absence of reactive oxygen species [96, 97]. In particular, [1-^{13}C]DHA, a ^{13}C enriched version of dehydroascorbic acid, has been studied with hyperpolarized (HP) ^{13}C magnetic resonance (MR) in preclinical models of cancer, diabetes, acute kidney injury, and fatty liver disease [97, 98, 99, 100, 101, 102]. In addition, ascorbates labeled for positron emission tomography (PET), namely [1-^{11}C]DHA and [1-^{11}C]VitC, have recently been synthesized and studied in ROS-producing immune cells *in vitro* [103]. Together, these studies suggest that ascorbate-derived imaging methods may be
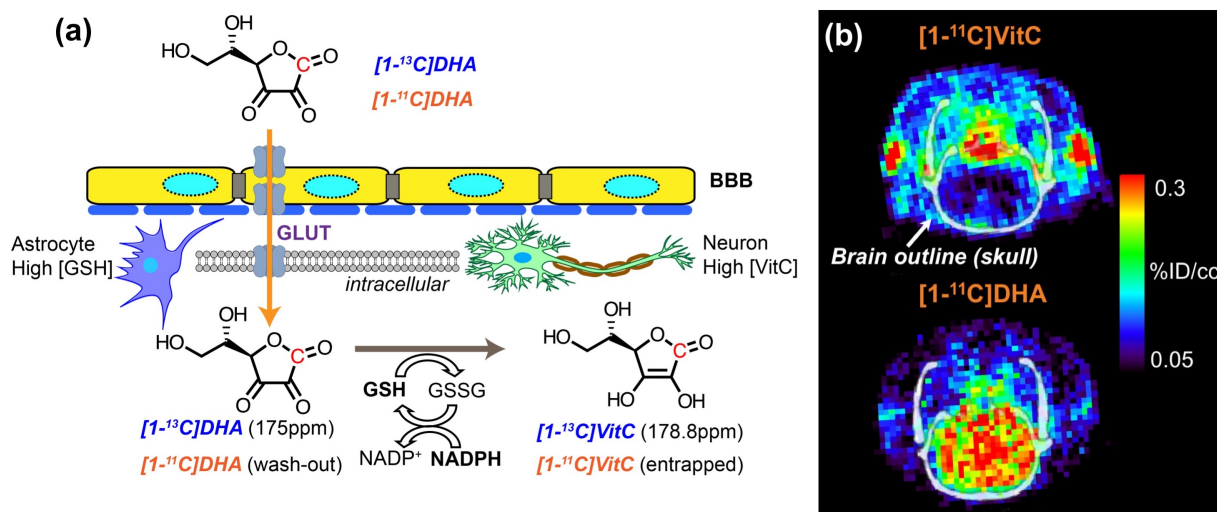
Figure 2.1: Ascorbates as redox imaging probes. (a) Dehydroascorbate (DHA) can traverse the blood-brain-barrier, enter cells via glucose transporter (GLUT) 1,3,4 and be rapidly reduced to ascorbic acid (vitamin C, VitC) by intracellular antioxidants including glutathione (GSH), which is coupled with the pentose phosphate pathway via NADPH. The conversion from hyperpolarized [1-^{13}C]DHA to [1-^{13}C]VitC can be monitored by MR spectroscopy, taking advantage of their unique chemical shifts. The C1 position of DHA and VitC can also be labelled with ^{11}C for PET and biodistribution studies. (b) In these PET images (adapted from Carroll et al. [103]), the accumulation of [1-^{11}C]DHA in the normal rat brain is compared to that of [1-^{11}C]VitC in the normal rat brain. In normal rats, higher brain signal for [1-^{11}C]DHA is expected since it readily crosses the blood-brain barrier and is transported into cells via GLUT transporters. In contrast, transport of VitC into the brain via sodium-dependent vitamin C transporter-2 (SVCT2) is a slower process. Unlike measuring the real-time conversion rate by hyperpolarized MR, PET and biodistribution with [^{11}C]ascorbates measures the uptake and retention of ^{11}C radiopharmaceuticals.

able to image oxidative stress *in vivo*. In particular, DHA-derived imaging agents were designed to image intracellular redox capacity, typically defined as the concentration of intracellular reducing equivalents and the ability to regenerate them. We therefore compared these methodologies in an animal model of pharmacologic glutathione depletion, to determine if ascorbate-derived HP MR or PET probes could detect the modulation of redox capacity.

Although [1-^{13}C]DHA and [1-^{11}C]DHA are chemically and biochemically equivalent, the techniques used to study them *in vivo* are considerably different. HP ^{13}C MR via dissolution dynamic nuclear polarization (dDNP) is an emerging imaging technology that allows direct visualization of metabolic conversion of ^{13}C-enriched molecules, and has been applied extensively to study metabolism in cells, tissues, animal models, and patients [104, 105, 106]. dDNP transfers po-

larization from electron spins to ^{13}C nuclei spins at extreme low temperature (0.8–1.3 K) through microwave irradiation, providing more than 10,000-fold MR signal enhancement of ^{13}C-labelled substrates [10]. The HP substrate can be subsequently injected into a living system and its conversion to other metabolites can be monitored by MR spectroscopy in a rapid, real-time manner. HP MR with [1-^{13}C]DHA takes advantage of the chemical shift between [1-^{13}C]DHA and [1-^{13}C]VitC (3.8 ppm) and the drastic signal enhancement (approximately 10% polarization, $>10^4$-fold at 3 Tesla) provided by dDNP to enable *in vivo* interrogation of redox capacity. Since the hyperpolarized signal lifetime is prescribed by the T_1 of the substrate (approximately 57 s for [1-^{13}C]DHA at 3 Tesla), *in vivo* HP ^{13}C signal can be observed for approximately 1 to 2 minutes at most [96]. Therefore, the real-time detection of [1-^{13}C]DHA to [1-^{13}C]VitC *in vivo* is primarily a kinetic measurement that depends on substrate transport and the availability of intracellular reducing equivalents.

In contrast, PET is an established metabolic imaging technology whereby a positron-emitting isotope, such as ^{11}C or 18F, is incorporated into a drug or metabolite of interest, and usually imaged following a significant delay depending on the half-life of the radioactive isotope. Therefore, the primary determinants of image contrast are the transport and retention/entrapment of the radiopharmaceutical, and the clearance of nonspecific signal. As shown in **Figure 2.1b**, PET images of rat brains demonstrated the distinctive difference in accumulated signal between [1-^{11}C]DHA and [1-^{11}C]VitC, as previously reported, reflecting their differential transport across the blood-brain barrier and cellular membrane [103]. In the case of [1-^{11}C]DHA, the radiopharmaceutical is expected to be entrapped inside the cell once it is reduced to [1-^{11}C]VitC, a charged molecule at physiological pH, and unreacted [1-^{11}C]DHA may be washed out. We hypothesized that retention of [1-^{11}C]DHA would depend partially on intracellular reducing agents including GSH [107], and therefore may also be modulated following glutathione-depletion.

In this study, we aimed to characterize ascorbate-derived HP ^{13}C MR and ^{11}C PET probes for brain imaging, and take advantage of their different capabilities to assess *in vivo* redox capacity of the rat brain. First, we studied the transport, compartmentalization, and biodistribution of both DHA and VitC in normal rat brain with HP ^{13}C MR and ^{11}C PET probes. Then we modulated GSH content in rats by pharmacological treatment and studied the changes in DHA to VitC conversion in the brain using both HP ^{13}C MR and ^{11}C PET probes. Specifically, four groups of Sprague-Dawley rats were studied using: (I) two-dimensional (2D) chemical shift imaging (CSI) with HP

[1-^{13}C]DHA and [1-^{13}C]VitC separately to determine the transport and compartmentalization of ascorbates in the head region (n = 6 for DHA, n = 6 for VitC); (II) one-dimensional (1D) slice-selective dynamic spectroscopy with HP [1-^{13}C]DHA, at 24 hours before and 2 hours after diethyl maleate (DEM) intraperitoneal injection (4.6 mmol/kg) [108], to measure the real-time DHA to VitC conversion rate (n = 4); (III) biodistribution using [1-^{11}C]DHA and [1-^{11}C]VitC, respectively, to determine the accumulation of ascorbate-derived probes in the brain and other organs (n = 3 each); (IV) biodistribution with [1-^{11}C]DHA in rats with DEM treatment as in group (2) to measure ^{11}C probe accumulation following glutathione depletion (n = 3). Additionally, 1D slice-selective dynamic spectroscopy with HP [1-^{13}C]DHA at 60% concentration of Group II was performed to demonstrate DHA to VitC reaction order (n = 3), and an *in vitro* GSH assay was performed on brain tissues collected from normal and DEM-treated rats to validate the redox modulation by DEM (n = 7 each).

2.2 Results

2.2.1 Behavior of HP ^{13}C DHA and VitC *in vivo* is consistent with known features of blood-brain barrier penetration and transport

Both HP [1-^{13}C]DHA and HP [1-^{13}C]VitC were administered separately to normal rats (group 1). Following HP [1-^{13}C]DHA injection, its reduction to [1-^{13}C]VitC was observed in the brain, demonstrated by the presence of a new downfield resonance (approximate 3.8ppm) in the ^{13}C MR spectrum (n = 6). For HP [1-^{13}C]DHA study, the DHA resonance was observed in most tissue voxels including brain and its surrounding tissues (muscle and vasculature), while the VitC metabolite was only observed in the brain voxels (**Figure 2.2a**) with VitC/(DHA + VitC)= 0.48 $\pm$ 0.15 (estimated from 18 brain voxels), consistent with penetration of DHA across the blood-brain barrier. In contrast, when HP VitC is injected, the 2D CSI (n = 3) found drastically lower VitC signal in the brain (mostly below quantification limit) than in surrounding tissues and no oxidation to DHA (**Figure 2.2b**). These data are consistent with the slower transport of VitC across the blood-brain barrier, and the high reducing capacity of the normal brain [90].
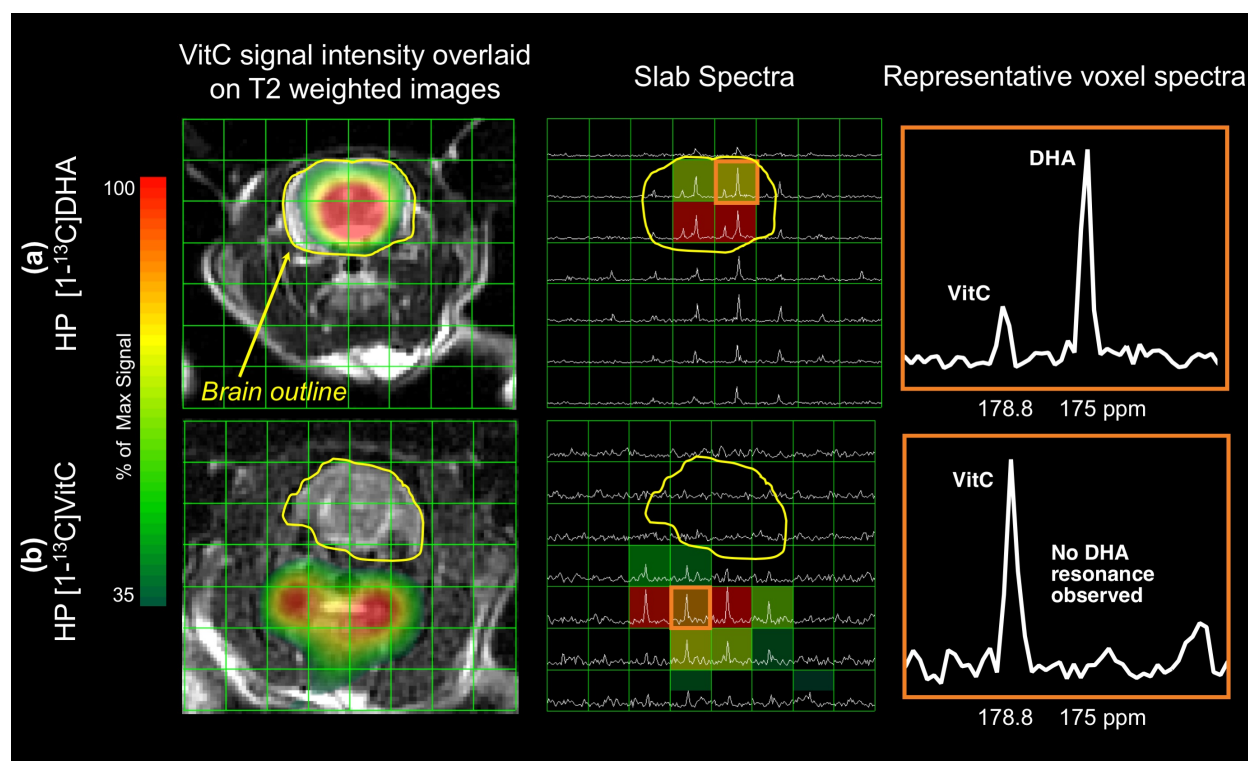
Figure 2.2: 2D Chemical Shift Imaging with hyperpolarized ^{13}C ascorbates reveals different transport and compartmentalization of dehydroascorbate (DHA) and vitamin C (VitC). (a) Injection of hyperpolarized [1-^{13}C]DHA, with conversion to VitC in the normal rat brain. The VitC resonance is only observed in voxels corresponding to the brain as shown in the VitC signal intensity map and slab spectra, while the DHA resonance is observed both in the brain and surrounding tissue. A representative voxel corresponding to brain tissue shows both a resonance corresponding to the introduced hyperpolarized [1-^{13}C]DHA and its metabolite [1-^{13}C]VitC. **(b)** Injection of hyperpolarized [1-^{13}C]VitC in normal rats. Lower (in this case negligible) VitC signal is seen in voxels corresponding to brain as shown in the VitC signal intensity map and slab spectra, and no oxidation to DHA is observed. A representative voxel corresponding to tissues in the neck show a resonance corresponding to the introduced hyperpolarized [1-^{13}C]VitC without evidence of metabolic conversion.

2.2.2 Glutathione depletion via diethyl maleate results in a lower rate of DHA-to-VitC conversion

Using a 1D dynamic HP [1-^{13}C]DHA study, we investigated whether the DHA to VitC conversion rate is correlated with GSH content in the rat brain (group 2). We adopted a variable flip angle scheme to account for the non-renewable nature of hyperpolarized signal and to utilize signal-to-noise ratio (SNR) efficiently since the T_1 of [1-^{13}C]VitC is relatively short (29.1 s, *in vitro* at 3T) [98]. Dynamic spectra of the rat brain showed that the [1-^{13}C]VitC signal gradually increases during the acquisition window used (**Figure 2.3**), suggesting VitC production rate is greater than signal decay rate mediated by T_1 relaxation. Because VitC signal is mainly from in the brain while DHA signal is from both the brain and surrounding tissues on the 1D slab spectra, we focused the analysis on the kinetic rates of VitC production as opposed to including both DHA and VitC in the kinetic model or using ratiometric approach.

We found the apparent VitC production rate (k$_{app}$) decreased by nearly 40% from 6.94 $\pm$ 1.52 s^{-1} to 4.03 $\pm$ 2.83 s^{-1} ($P = .0293$) after DEM treatment (**Figure 2.4a**). The apparent *in vivo* T_1 of VitC was estimated to be 7.80 $\pm$ 1.28 s (n = 9) using a subset of data (3 datasets were excluded due to poor fitting quality), and we found kinetic rate (k) decreased by nearly 50% from 14.15 $\pm$ 2.93 s^{-1} to 7.48 $\pm$ 1.80 s^{-1} ($P = .0218$) after DEM treatment (**Figure 2.4b**). Correspondingly, the *in vitro* GSH assay showed that brain GSH content in the DEM-treated rats is significantly lower than in the control rats (5.99 $\pm$ 0.64 vs. 12.31 $\pm$ 0.75 µmol/gram of protein, n = 7, $P <$ .0001) (**Figure 2.4c**).

To validate our kinetic modeling of the DHA to VitC conversion, dynamic 1D spectroscopy was performed on a separate cohort of rats (n = 3) with 18 µmoles HP DHA (approximately 60% dose of the control/baseline group). We found there was no statistically significant difference between the control/baseline group and lower dose group in k$_{app}$ (4.94 $\pm$ 1.04 vs. 4.38 $\pm$ 0.70 s^{-1}, $P =$ .678), or k (11.22 $\pm$ 1.74 vs. 0.94 $\pm$ 1.86 s^{-1}, $P = .917$) as well as the sum of VitC signal (510.3 $\pm$ 65.06 vs. 507.6 $\pm$ 73.94 A.U., $P = .9792$) (**Figure 2.4d–g**), suggesting that DHA dose used in our experimental set-up was in excess and not a rate limiting factor for VitC production.
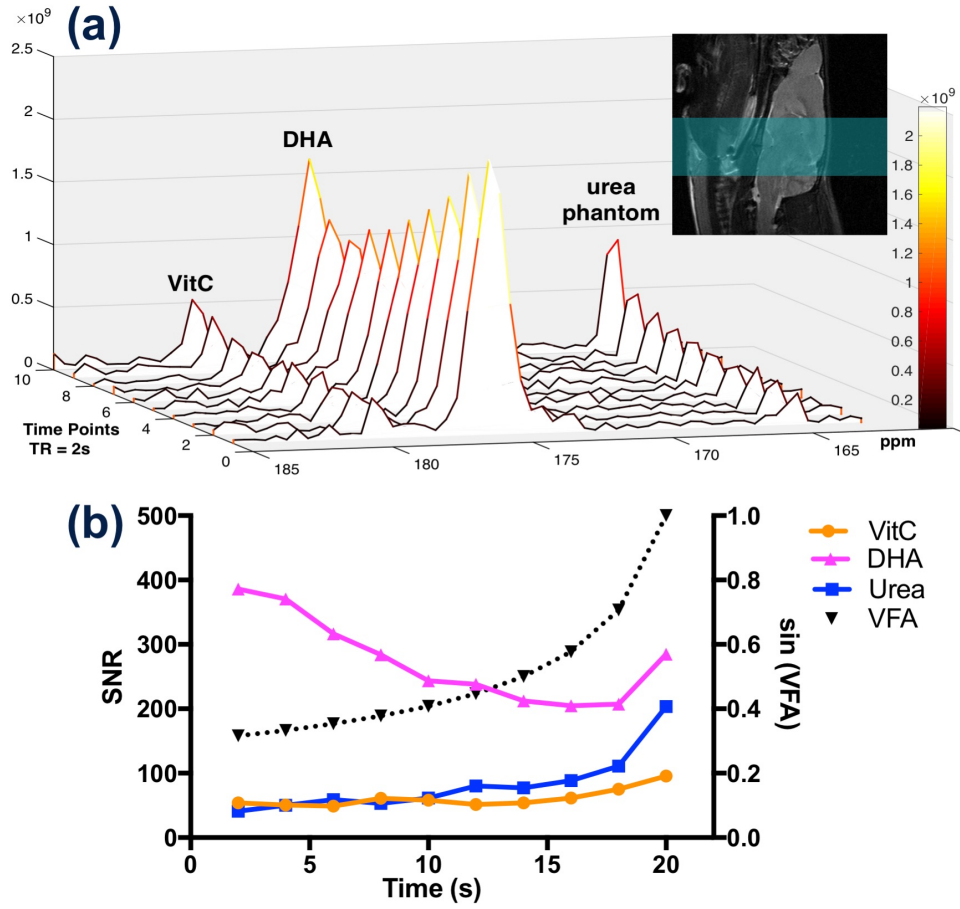
Figure 2.3: Dynamic 1D slice-selective spectroscopy reveals real-time hyperpolarized [1-^{13}C]dehydroascorbate (DHA) to [1-^{13}C]vitamin C (VitC) conversion. MR spectra of a normal rat brain is shown in (a), and signal-to-noise ratio quantification of DHA, VitC, and urea phantom (solid line), as well as variable flip angle (VFA) scheme (dash line), are plotted in (b). Hyperpolarized [1-^{13}C]VitC signal in a normal rat brain gradually increases over time despite the rapid longitudinal relaxation (*in vitro* T_1 about 29.2 s at 3 Tesla), and hyperpolarized [1-^{13}C]DHA signal gradually decreases due to metabolic conversion and longitudinal relaxation (*in vitro* T_1 about 56.5 s at 3 Tesla). Signal corresponding to the [^{13}C]urea phantom (placed next to the rat head) also gradually increases, demonstrating the VFA scheme. A sagittal T_2-weighted image demonstrates the imaging slab (highlighted region).
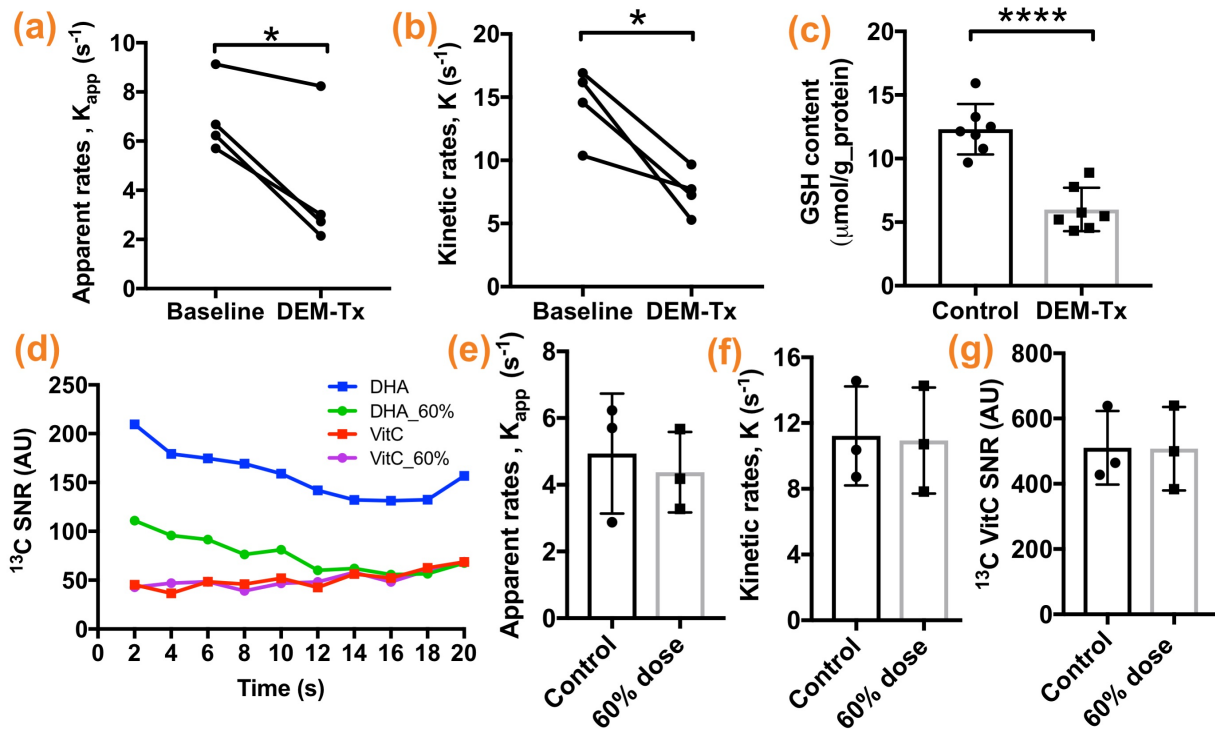
Figure 2.4: Glutathione depletion via diethyl maleate (DEM) results in a significantly lower rate of [1-¹³C]dehydroascorbate (DHA) to [1-¹³C]vitamin C (VitC) conversion. Both apparent VitC production rate (k_{app}) and kinetic rate (k) of VitC production in the brain decreased significantly after DEM treatment (a,b), consistent with significantly lower brain GSH content in DEM-treated rats compared to control rats (c). To demonstrate DHA to VitC reaction order, 1D spectroscopy was performed on a separate cohort of rats with HP [1-¹³C]DHA at 60% of the usual dose. The average signal of [1-¹³C]DHA and [1-¹³C]VitC at each time point were plotted (d), and VitC signal appears unchanged with decreased DHA dose. The resulting k_{app}, k, and total ¹³C VitC SNR are not significantly different from the control group (e,f,g). ($*P < .05$, $****P < .0001$).

2.2.3 ^{11}C Biodistribution studies showed expected differences between [1-^{11}C]DHA and [1-^{11}C]VitC, but no effect of diethyl maleate treatment on [1-^{11}C]DHA brain accumulation

The biodistribution of [1-^{11}C]DHA or [1-^{11}C]VitC was compared by ex vivo biodistribution analysis on harvested normal rat tissues 1 hour following administration (group 3, n = 3 each). In addition, [1-^{11}C]DHA was administrated to DEM-treated rats (group 4, n = 3) to study the effect of GSH content on ^{11}C radiopharmaceutical accumulation. Biodistribution of ^{11}C radiopharmaceutical in three groups of rats are shown in Figure 2.5. [1-^{11}C]VitC showed lower uptake/retention in the brain than [1-^{11}C]DHA (0.25 ± 0.012 vs. 0.49 ± 0.075 % Injection Dose(ID)/g, $P = .0330$), consistent with our HP MR observations and our previously reported PET imaging study (**Figure 2.1b**). However, lung and liver showed significantly higher uptake/retention for [1-^{11}C]VitC than [1-^{11}C]DHA (lungs: 2.10 ± 0.12 vs. 0.42 ± 0.066 %ID/g, $P = .0002$; liver: 3.57 ± 0.30 vs. 2.12 ± 0.39 %ID/g, $P = .0408$). For the glutathione modulation study using [1-^{11}C]DHA, no significant difference was found in radiopharmaceutical accumulation for major organs between control and DEM-treated subjects (0.49 ± 0.075 vs. 0.62 ± 0.14 %ID/g, $P = .449$).

2.3 Discussion

Non-invasive *in vivo* evaluation of brain redox capacity and oxidative stress could provide insights into neurological disease progression and therapeutic response. In this study, we used ascorbate-based imaging probes to study brain redox capacity leveraging both HP-MR and PET modalities. We first demonstrated that HP [1-^{13}C]DHA is readily converted to HP [1-^{13}C]VitC in the normal brain, evidenced by 2D chemical shift imaging revealing both DHA and VitC resonances in voxels corresponding to brain tissues following [1-^{13}C]DHA injection. This finding is consistent with the penetration of DHA through BBB and its rapid entry into cells. In contrast, when HP [1-^{13}C]VitC was administered, lower hyperpolarized signal was seen in brain voxels and no oxidation to HP [1-^{13}C]DHA was observed. These findings reflect the slow cellular transport process of VitC via SVCT2 against a concentration gradient, and the role of VitC as an antioxidant reservoir that is not easily oxidized. These features represent the major shortcomings of [1-^{13}C]VitC as a HP MR probe for imaging the brain.
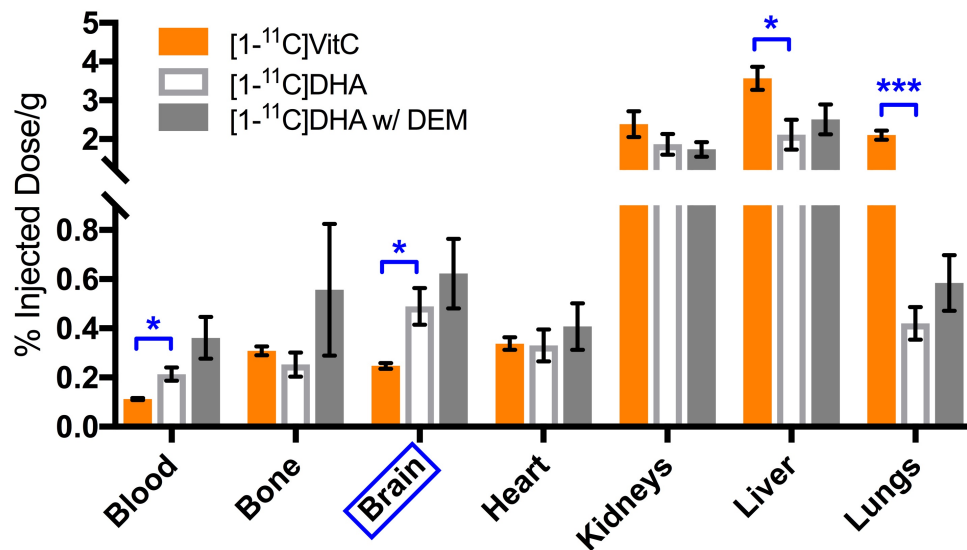
Figure 2.5: Biodistribution studies revealed differential accumulation of ^{11}C dehydroascorbate (DHA) and vitamin C (VitC) in normal rat brain but no effect of diethyl maleate (DEM) treatment. Gamma counting of harvested brains showed a significantly higher signal accumulation for [1-^{11}C]DHA than [1-^{11}C]VitC in the normal brain 1 hour following radiopharmaceutical administration. In addition, there was significantly higher uptake/retention for [1-^{11}C]VitC versus [1-^{11}C]DHA in the lungs and liver in normal rats. In the DEM-treated rats with [1-^{11}C]DHA, no significant differences were found in ^{11}C radiopharmaceutical uptake/retention between normal and DEM-treated rats in major organs, including the brain ($^*P < .05$, $^{***}P < .001$).

After characterizing the transport and compartmentalization of DHA and VitC, we modulated GSH content with DEM treatment which depletes GSH by direct conjugation [108], and studied the changes in DHA to VitC kinetic rates using dynamic HP ^{13}C MR spectroscopy. 2D CSI with radiometric quantification has lower reproducibility due to sensitivity to small differences in acquisition timing and substrate delivery, demonstrated by the variabilities in VitC/DHA ratios in 6 normal rats. Therefore, we adopted 1D slab dynamic acquisition approach with variable flip angle scheme for efficient SNR usage, which is important given the short T_1 of [1-^{13}C]VitC, to study the effect of redox modulation. In dynamic spectra of normal brain, there was observable real-time production of VitC; we also observed that DHA signal is about 5 times higher than VitC signal, suggesting that cellular transport and/or enzyme and cofactor turnover rate are likely rate-limiting factors for the observed VitC production. In other words, these data suggested that the DHA dose was in excess and not a rate-limiting factor in our experimental set-up. To demonstrate the reaction order, we performed dynamic spectroscopy with lower (60%) doses of [1-^{13}C]DHA and found that the kinetic rates of VitC production and sum of VitC SNR are independent of DHA concentration, which validated the pseudo-zero-order kinetic model. To quantify *in vivo* reaction kinetics, we generated two kinetic parameters (reported in Methods section): apparent VitC production rate (k_{app}) is a straightforward parameter that reflects the rate of product accumulation, assuming T_1 relaxation equally affects the control and DEM-treated groups; whereas kinetic rate (k) was generated by non-linear fitting and takes account of T_1 relaxation. We found that DHA to VitC conversion rate correlated with the brain GSH content, as evidenced by significantly reduced kinetic parameters (k_{app} and k) after DEM treatment that depletes GSH by more than 50%.

There are several important considerations and limitations of our dynamic [1-^{13}C]DHA MR study. First, each animal was subjected to two intravenous injections of [1-^{13}C]DHA, an oxidant that could deplete GSH, 24 hours apart between baseline and post-DEM-treatment imaging [94]. However, Weber et al. have demonstrated that rat brain GSH content returns to normal 24 hours after DEM treatment, a prototypical GSH deleting agent that directly conjugates with GSH and is more potent than DHA [108]. Furthermore, depletion of GSH by DHA could induce increases in other intracellular reducing equivalents (such as thioredoxins) whose pool size would be expected to impact the rate of DHA to VitC reduction. Timm et al. have shown that DHA administration resulted in a rapid increase in GSSG/GSH ratio and pentose phosphate pathway (PPP) flux in cells

and tumors [102]. It can be argued that the initial DHA administration for baseline imaging could upregulate PPP flux and other reducing equivalents, which would be a confounding factor for our study. Nevertheless, the DEM treatment seemed to offset the increase in PPP flux and other reducing equivalents as the VitC production rate decreased significantly. Second, the supraphysiologic concentration of administered HP [1-^{13}C]DHA could saturate the transporter or relevant enzymes and create a rate-limiting condition, or result in substrate inhibition and decrease of enzymatic flux. Third, unlike the first-order reaction model, the kinetic parameters generated from pseudo-zero-order model are highly influenced by the numerical scale (i.e. SNR), which could potentially explain the inter-subject variability. For this reason, our dynamic acquisition and analysis scheme could only detect the *relative changes* in GSH content, but not the absolute concentration.

Another important consideration is the physiologic effect of DEM treatment in rats. We noted that rats became lethargic after DEM treatment. Numerous studies have explored the potential toxic effects of DEM in the heart and lung, and the dose we used was approximately 40% of the LD$_{50}$ reported for oral administration to rats [109, 110, 111, 112]. We also observed that the total ^{13}C SNR was approximately 35% lower on average in DEM-treated than normal rats despite similar DNP solid state buildup, suggesting less HP ^{13}C substrate was delivered to the imaging slab. Although we have demonstrated that the rate of VitC production is independent of DHA dose administered in our supraphysiologic dose range, it is still possible that lower DHA substrate delivery contributed to the lower VitC production rate.

In addition to ascorbate-derived probes designed for HP MR, we also leverage ^{11}C radiopharmaceuticals, namely [1-^{11}C]DHA and [1-^{11}C]VitC, to study the uptake and biodistribution of ascorbates. [1-^{11}C]VitC showed lower accumulation than [1-^{11}C]DHA in the brain, consistent with HP ^{13}C MR findings and previously reported PET imaging data [103], but higher retention in the lung and liver 1 hour after administration, possibly due to high expression of SVCT in these tissues [113, 114, 115]. [1-^{11}C]DHA reduction to [1-^{11}C]VitC represents a potential trapping mechanism [103, 107], with unreduced [1-^{11}C]DHA likely washed out of the cell. In the DEM redox modulation study using [1-^{11}C]DHA, we initially hypothesized that the lower brain GSH content in DEM-treated cannot adequately reduce [1-^{11}C]DHA to [1-^{11}C]VitC, and un-reacted [1-^{11}C]DHA would be washed out resulting less [1-^{11}C]VitC retention (lower gamma counting). However, there was no difference in ^{11}C radiopharmaceutical retention rate in major organs between the normal and

DEM-treated groups.

There are several important differences between HP ^{13}C MR and ^{11}C biodistribution studies that could explain the inconsistent findings. As discussed in Methods section, ^{11}C radiopharmaceuticals were administrated at a considerably lower pharmacologic dose compared to HP ^{13}C probes (0.16 µmol vs. 30 µmol). It is possible that residual GSH in DEM-treated rats is adequate to reduce the lower pharmacologic dose of DHA used in ^{11}C studies. More importantly, the two technologies differ significantly in their mechanisms of generating image contrast and timing, making direct comparison of data difficult. Biodistribution studies were performed at 1 hour after DHA administration as compared to the 1 minute kinetic analysis applied to HP MR studies. Hence, it appears that although [1-^{11}C]VitC was likely generated at a slower rate in GSH-depleted animals, there was insufficient washout of unreacted [1-^{11}C]DHA to yield observable differences in ^{11}C accumulation. It is possible that dynamic PET imaging or biodistribution studies by gamma counting at earlier time points could reveal subtle differences in the radiopharmaceutical accumulation rate in the brain. Overall, our results suggested that the [1-^{11}C]DHA was insensitive to changes in redox capacity in this pharmacologic GSH depletion model using our experiment set-up. This highlights the potential value in studying real-time substrate conversion by HP MR as opposed to probe retention rate by biodistribution of radiopharmaceutical or PET imaging analysis.

In conclusion, we demonstrated the transport and biodistribution features of DHA and VitC in the brain by both HP ^{13}C MR and ^{11}C PET probes, and found that the kinetic rates of [1-^{13}C]DHA to [1-^{13}C]VitC conversion correlated with brain GSH content. These studies suggest that hyperpolarized [1-^{13}C]DHA can assess brain redox capacity non-invasively, and potentially allow visualization of oxidative stress in numerous brain pathologies.

2.4 Methods

Dynamic Nuclear Polarization (DNP). Both [1-^{13}C]DHA and [1-^{13}C]VitC were prepared, polarized, and dissolved in aqueous media as previously described [96]. A 2.2 M solution of [1-^{13}C]DHA dimer (ISOTEC, Sigma Aldrich, Miamisburg, OH) in dimethyacetamide (DMA) containing 15 mM OX063 trityl radical (GE Healthcare, Menlo Park, CA) was polarized on a HyperSense DNP instrument (Oxford Instruments, Abingdon, UK) operating at 3.35 Tesla and 1.3 K, achieving

approximately 10% polarization after 1 hour microwave irradiation (determined by separate NMR studies using the same material). The frozen sample was then rapidly dissolved in distilled water containing 0.3 mM ethylenediaminetetracetic acid (EDTA) with a final concentration of $15 - 22$ mM and pH of 5.5. For all *in vivo* studies, approximately 30 µmoles of [1-^{13}C]DHA ($1.3 - 2.0$ ml) were administered intravenously to rats. Similarly, a 2.2 M solution of [1-^{13}C]VitC (Omicron Biochemicals, South Bend, IN) was prepared as a sodium salt in NaOH/water/DMSO, polarized, and dissolved in 100 mM phosphate buffer to a final pH of 7.0. For 2D CSI studies, approximately 100 µmoles of HP [1-^{13}C]VitC were administered intravenously.

^{11}C radiopharmaceutical synthesis. [1-^{11}C]VitC were synthesized from L-xylosone and [^{11}C]HCN precursors using a GE PETtrace cyclotron at our on-site radiopharmaceutical facility as previously described [103]. Overall, [1-^{11}C]VitC was obtained with a decay-corrected radiochemical yield of $35.8 \pm 18\%$ and a specific activity of 1.7 ± 0.4 mCi/µmol (n = 3). [1-^{11}C]DHA was obtained by oxidation of [1-^{11}C]VitC with a decay-corrected radiochemical yield of $25.8 \pm 2.6\%$ and a specific activity of 1.85 ± 0.5 mCi/µmol (n = 6).

MR studies. All animal experiments were approved by the University of California, San Francisco Institutional Animal Care and Use Committee (IACUC) and performed in accordance with IACUC protocols. Rats were placed under 1.5–2% isoflurane anesthesia and administered 30 µmoles HP [1-^{13}C]DHA or 100 µmoles HP [1-^{13}C]VitC solution via tail-vein catheter for both 2D CSI studies and dynamic 1D spectroscopy. For group (1) rats (n = 6 for DHA and n = 3 for VitC), two-dimensional single time-point CSI was performed on a GE Signa 3 Tesla MR scanner using a dual-tuned ^{1}H-^{13}C coil with the following parameters: voxel size = $5 \times 5 \times 20$ mm, TE/TR = 135/210 ms, flip angle = 20°, spectral bandwidth/resolutio n = 5000/9.77 Hz, and 25 s acquisition delay after the start of injection. For group (2) rats, one-dimensional slice-selective dynamic spectroscopy with HP [1-^{13}C]DHA was performed using a similar set-up on a GE Signa 3 Telsa (n = 2 before and after DEM treatment) and a Bruker Biospec 3 Tesla MR scanner (n = 3 before DEM treatment, n = 2 after DEM treatment, n = 3 for 60% dose experiments), with the following parameters: spectral bandwidth/resolution = 25 kHz/12.2 Hz, slice thickness = 10 mm, TR = 2 s, 10 repetitions, RF-compensated variable flip angle scheme [116, 117], and 25 s acquisition delay after the start of injection. Axial and sagittal T_2-weighted anatomic images were acquired with a fast spin echo sequence prior to HP ^{13}C studies and used to prescribe the spectroscopy slab.

Rats were fasted for 8 hours before HP ^{13}C MR studies to reduce glucose competition with DHA for GLUTs as previously reported [96, 99, 118].

^{11}C biodistribution studies. Rats were placed under 1.5–2% isoflurane anesthesia and administered 304 ± 78 µCi [1-^{11}C]DHA or 360 ± 180 µCi [1-^{11}C]VitC via tail vein catheters (for group 3 and 4 rats). Animals were subsequently sacrificed at 1 hour after radiopharmaceutical injection, and internalized radioactivity was immediately measured on their harvested organs using a Hidex automatic gamma counter (Turku, Finland) (n = 3 each).

Reduced glutathione (GSH) quantification assay. *In vitro* GSH quantification assay was performed using a commercial available kit (Abcam, Cambridge, MA). Brain tissues were collected from rats and snap-froze in -80 °C immediately upon extraction. A non-fluorescent dye that becomes strongly fluorescent upon reacting with glutathione was added to the tissue supernatant after deproteinization (Abcam, Cambridge, MA), and the fluorescent signal was read by a microplate reader (Infinite M200, Tecan Group Ltd., Mannedorf, Switzerland) at Ex/Em = 490/520 nm. In parallel, a bicinchoninic acid assay (BCA) protein quantification assay (Abcam, Cambridge, MA) was performed using the same tissue supernatant before deproteinization, and GSH concentration was normalized to protein content and reported in the unit of µmol/gram of protein.

Data analysis. 2D CSI data was reconstructed and overlaid on axial anatomic images using open-source software SIVIC [119]; the peak heights of DHA and VitC resonances were manually quantified on the magnitude spectrum. The metabolite ratio, VitC/(DHA + VitC), was calculated for each voxel. For 1D dynamic MR spectroscopy data, SNRs of DHA and VitC resonances for each time point were quantified based on the fit peak integral in MestreNova12 (Mestrelab, Madrid, Spain), and were subsequently used to generate kinetic parameters in MATLAB 2017b (MathWorks, Natick, MA)). We demonstrated that the DHA to VitC conversion in this experiment was a pseudo-zero-order reaction as shown in Results section, and generated two kinetic parameters based on a zero-order kinetic model assuming no back conversion from VitC to DHA: (1) apparent VitC production rate (k_{app}) via linear fitting of VitC signal and normalized to total VitC SNR, and (2) kinetic rate (k) via non-linear least square fitting of VitC signal with the Trust-Region algorithm to the following equations:

$$\frac{dM_z}{dt} = k + \frac{1}{T_1}M_z \tag{2.1}$$

$$M_{z,n} = \frac{M_{xy,n}}{\sin\theta_n \prod_{i=1}^{n-1}\cos(\theta_i)} \tag{2.2}$$

where Mz is longitudinal magnetization, Mxy is transverse magnetization (observed signal), n is the index of time points, and $\theta = arctan(1/\sqrt{N-n})$ is the flip angle. Dynamic data was first fit into kinetic models with T_1 as an unknown parameter to estimate apparent *in vivo* T_1 of VitC, which was subsequently incorporated into the kinetic model as a fixed parameter to generate k assuming T_1 is the same across the subjects. Apparent kinetic rate (k_{app}) reflects the rate of observed VitC signal change caused by both T_1 relaxation and VitC production from DHA, while k reflects only the VitC production rate.

A paired Student's t-test was used to compare kinetic parameters before and after DEM treatment. An unpaired Student's t-test was used to compare the GSH content of rat brains with and without DEM treatment and biodistribution of [1-^{11}C]ascorbates. All statistical analyses were performed using GraphPad Prism 7d (La Jolla, CA). All quantitative results are reported and graphed as mean $\pm$ standard deviation; $P < .05$ were considered statistically significant, and our P values for biodistribution analysis were not adjusted for multiple comparisons.

Chapter 3: Simultaneous Metabolic and Perfusion Imaging Using Hyperpolarized ^{13}C MRI can Evaluate Early and Dose-Dependent Response to Radiation Therapy in a Prostate Cancer Mouse Model

Abstract

Purpose: To investigate use of a novel imaging approach, hyperpolarized (HP) ^{13}C magnetic resonance imaging (MRI) for simultaneous metabolism and perfusion assessment, to evaluate early and dose-dependent response to radiation therapy (RT) in a prostate cancer mouse model.

Methods and Materials: Transgenic Adenocarcinoma of Mouse Prostate (TRAMP) mice (n = 18) underwent single-fraction RT (4-14 Gy steep dose across the tumor) and were imaged serially at pre-RT baseline and 1, 4, and 7 days after RT using HP ^{13}C MRI with combined [1-^{13}C]pyruvate (metabolic active agent) and [^{13}C]urea (perfusion agent), coupled with conventional multiparametric ^{1}H MRI including T_2-weighted, dynamic contrast-enhanced, and diffusion-weighted imaging. Tumor tissues were collected 4 and 7 days after RT for biological correlative studies.

Results: We found a significant decrease in HP pyruvate-to-lactate conversion in tumors responding to RT, with concomitant significant increases in HP pyruvate-to-alanine conversion and HP urea signal; the opposite changes were observed in tumors resistant to RT. Moreover, HP lactate change was dependent on radiation dose; tumor regions treated with higher radiation doses (10-14 Gy) exhibited a greater decrease in HP lactate signal than low-dose regions (4-7 Gy) as early as 1 day post-RT, consistent with lactate dehydrogenase enzyme activity and expression data. We also found that HP [^{13}C]urea MRI provided assessments of tumor perfusion similar to those provided by ^{1}H dynamic contrast-enhanced MRI in this animal model. However, apparent diffusion coefficient, a conventional ^{1}H MRI functional biomarker, did not exhibit statistically significant changes within 7 days after RT.

Conclusion: These results demonstrate the ability of HP ^{13}C MRI to monitor radiation-induced physiologic changes in a timely and dose-dependent manner, providing the basic science premise for further clinical investigation and translation.

3.1 Introduction

Radiation therapy (RT), including external beam RT and brachytherapy, is the standard management option for both localized and advanced prostate cancer (PCa) [120, 121]. Despite the technical advances in RT, treatment failure and disease recurrence are common and place a significant burden on care of patients with PCa [122, 123]. Specifically, treatment failure at the targeted tumor site is the primary mode of PCa recurrence after RT, suggesting inadequate targeting, dose delivery, and intrinsic radio-resistance [124, 125, 126]. Although a lower prostate-specific antigen (PSA) nadir is associated with improved outcomes, absolute PSA levels are inadequate to distinguish treatment failure from treatment success. In addition, post-RT PSA decreases are slow, taking an average of 18 months before reaching the nadir; therefore, they are unable to provide early or tumor-specific evaluations [127]. These clinical challenges have motivated the development of imaging technologies that can detect early and localized RT response or failure.

Imaging has played an expanding role in RT planning and evaluation. Increasingly, molecular and functional imaging modalities, including positron emission tomography and ^{1}H multiparametric magnetic resonance imaging (MRI), have been applied to guide RT planning, evaluate post-RT response, and identify cancer recurrence [128, 129, 130, 131]. Hyperpolarized (HP) ^{13}C MRI is a paradigm-shifting molecular imaging technology for cancer diagnosis and therapy monitoring with a unique ability to study real-time metabolism and perfusion simultaneously. HP ^{13}C MRI is enabled by dissolution dynamic nuclear polarization, which provides greater than 5 orders of magnitude signal enhancement for ^{13}C enriched, nonradioactive imaging agents [10, 132]. HP [1-^{13}C]pyruvate MRI has allowed direct visualization of glycolic metabolism in patients with PCa [69], and numerous clinical studies are ongoing to characterize cancer aggressiveness and response to targeted therapies [82, 13]. HP [1-^{13}C]pyruvate can be copolarized and imaged with HP [^{13}C]urea to assess metabolism and perfusion simultaneously, providing new measures of cancer aggressiveness and therapy response [133, 24, 134, 135].

Radiation induces cell cycle arrest, senescence, apoptosis, and eventual cell death [136, 137], resulting in decreased glycolytic flux; therefore, a decrease in HP ^{13}C pyruvate-to-lactate conversion rate may reflect metabolic remission after RT. In contrast, high tumor lactate content after RT and the associated lactate dehydrogenase (LDH) overexpression have been shown to be associated

with a radio-resistant phenotype [45, 46, 138]. These differential metabolic profiles between radiosensitive and radio-resistant tumors provide a strong rationale to study lactate metabolism for RT assessment. In addition, the pyruvate-to-lactate conversion rate also depends on the concentration of nicotinamide adenine dinucleotide (NADH), a cofactor in the LDH-mediated reduction of pyruvate. Because NADH modulates the cellular reducing potential, the rate of HP ^{13}C pyruvate-to-lactate reduction might also reflect oxidative stress induced by ionizing radiation [139]. RT also causes complex changes to tissue perfusion and cellularity [140, 141]. As [^{13}C]urea is a metabolically inactive agent without background signals, HP MRI can trace the vascular delivery and interstitial distribution of injected HP [^{13}C]urea agent, thereby assessing tissue perfusion similar to dynamic contrast-enhanced (DCE) MRI with gadolinium-based contrast agent. Thus, HP [1-^{13}C]pyruvate and [^{13}C]urea are ideal imaging probes to study the biological processes implicated in RT resistance and response.

In this study, we applied HP MRI using combined [1-^{13}C]pyruvate and [^{13}C]urea to evaluate early and dose-dependent tumor response to RT. We also incorporated DCE MRI and diffusion-weighted imaging (DWI), 2 clinical standard techniques in multiparametric ^{1}H MRI, to assess changes to the tumor microenvironment and to investigate their concordance with HP data. We hypothesized that (1) dual-agent HP ^{13}C and multiparametric ^{1}H MRI could detect altered tumor physiology within days after RT and (2) these changes would be associated with both therapeutic response and radiation dose.

3.2 Methods and Materials

Study design. All animal procedures were approved by our institutional animal care and use committee. Transgenic Adenocarcinoma of Mouse Prostate (TRAMP, C57BL/6xFVB, Roswell Park Cancer Institute, Buffalo, NY) mice (n = 18) underwent single-fraction RT and were imaged serially using HP ^{13}C MRI and multiparametric MRI including T_2-weighted imaging, DCE MRI, and DWI. Imaging study time points included pretherapy and 1, 4, and 7 days posttherapy. Mice were euthanized for tissue collection on days 4 (n = 4) and 7 (n = 7).

RT was delivered with a microSelectron brachytherapy system (Elekta/Nucletron, Veenendaal, the Netherlands) with a high-dose-rate applicator and Ir-192 as the radiation source. A 10-Gy

radiation dose in a single fraction was prescribed to a 3 mm depth, providing a steep dose gradient across the tumor ranging from 4 to 14 Gy. Treatment-planning CT images (Siemens, Malvern, PA) and radiation dose distribution maps (Oncentra Brachy software, Elekta/Nucletron) were obtained to investigate dose-dependent tumor response.

Imaging methods. All MRI experiments were performed on a 14.1 Tesla Varian MR microimaging system (Agilent Technologies, Santa Clara, CA). Dynamic nuclear polarization was performed on a HyperSense polarizer (Oxford Instruments, Abingdon, UK): [1-^{13}C]pyruvic acid and [^{13}C]urea were copolarized and subsequently injected intravenously, as described previously [142]. Metabolite-specific imaging was performed using a single-shot, 3-dimensional (3D) GRadient And Spin Echo (GRASE) sequence to image HP [1-^{13}C]lactate, [1-^{13}C]alanine, [1-^{13}C]pyruvate, [^{13}C]urea, and HP001 (a frequency-calibration phantom) sequentially, as described previously.[20,21] Detailed imaging methods, including multiparametric MRI, are reported in the Supplementary Information **Section 3.6.1**.

Image analysis. Tumor volumes were measured on T_2-weighted MRI using in-house developed software (BRIMAGE). All other image analyses were performed on a pixel-by-pixel basis using MATLAB 2018b (MathWorks, Natick, MA). Normalized [1-^{13}C]lactate signal (nLac) was calculated as the percentage of lactate to pyruvate and its downstream metabolites, "lactate/(pyruvate + lactate + alanine)," and [^{13}C]urea signal was normalized to the sum of [^{13}C]urea signal within the imaging volume (lower abdomen and pelvis of the mouse) to account for variations in polarization levels and transfer time. Signal-to-noise ratio (SNR) was calculated using Rician noise for magnitude images, and only voxels with SNR greater than 3 were included [143, 144]. HP [1-^{13}C]alanine has considerably lower signal than other metabolites and is quantified as a percentage of tumor voxels with SNR greater than 3.

Semiquantitative analysis of DCE was based on GBCA concentration, including initial area under the curve (iAUC; sum of 90 seconds from the start of injection) as well as wash-in and wash-out slopes (in milli-Molars per minute). Detailed DCE image analysis methods are reported in the Supplementary Information **Section 3.6.2**. For DWI analysis, apparent diffusion coefficients (ADC; $\times 10^{-3}$ mm^2/s) were estimated on the basis of linear fitting of diffusion-weighted signal of 4 b-values to the equation $S = S_0 \cdot exp(-ADC \cdot b)$ using VNMRJ software (Agilent Technologies).

Radiation dose maps were co-registered with MRI scans using a rigid registration algorithm

based on Mattes Mutual information registration metric using an open-source software 3D Slicer.33 To mitigate the registration error, we grouped the radiation dose ranges into only 3 categories (high, 10-14 Gy; intermediate, 7-10 Gy; low, 4-7 Gy), rather than performing a linear dose-response correlation. A subset of mice (n = 7) did not have congruent radiation dose maps. Tumor regions of interest (ROIs) were manually drawn on the T_2-weighted, DWI, and DCE images and then applied to ^{13}C images. The means of imaging quantifications of the whole tumor and tumor regions treated with low (4-7 Gy), intermediate (7-10 Gy), and high (10-14 Gy) radiation doses were calculated.

Biological correlations. TRAMP tumors were harvested at 4 (n = 4) or 7 days (n = 7) after RT. Tumor tissues corresponding to high and low radiation doses were excised after review of the corresponding T_2-weighted MRI scans and registered dose maps before dissection; the intermediate zones were avoided, only comparing the tumor cross-sectional specimens of high-dose (ventral) versus low-dose (dorsal) regions, which were spatially well separated because of the directionality of the radiation dose gradient. In addition, 1 group of untreated TRAMP tumors (n = 11) of similar tumor stage was harvested as untreated control. Immunohistochemistry (IHC) was performed, including anti-Ki-67 and anti-caspase-3/ASP175 staining; gene expression assays for relevant transporters and enzymes in glycolic metabolism, including lactate dehydrogenase-α, -β(LDH-A,B) and monocarboxylate transporters 1 and 3/4 (MCT1, 3/4); and LDH enzyme activity assay. Quantifications of IHC staining were obtained by visual microscopic inspection to assess percentage of positively stained cells, using iterative inspections at various magnification levels over an entire tumor cross-section. Detailed methods are reported in the Supplementary Information **Section 3.6.3**.

Statistical analysis. Changes in imaging quantifications of the whole tumor were evaluated using multilevel regression analyses (Supplementary Information **Section 3.6.3** and **Table S.3.1**). The relationship between imaging quantifications and radiation doses was evaluated using a repeated measures one-way analysis of variance test for each time point, followed by multiple comparisons using Tukey's methods. A linear regression analysis with a clustered variance structure was used to examine the relationship between variables containing repeated measurements such as HP [^{13}C]urea and DCE quantifications. A paired Student's t test was used to compare biological correlative measurements from regions treated with high and low radiation doses, and an unpaired t test was used to compare treated versus untreated control tumors. Data are reported as mean $\pm$

standard deviation for descriptive statistics or estimate $\pm$ standard error for regression analysis. P values less than .05 are considered statistically significant. All statistical analyses were performed using Stata 16 (StataCorp, College Station, TX) and Prism 8 (GraphPad, San Diego, CA).

3.3   Results

3.3.1   Changes in tumor metabolism and perfusion by hyperpolarized ^{13}C MRI are indicative of post-RT response

Modeled after the revised Response Evaluation Criteria in Solid Tumors (RECIST) criteria,34 mice with increased tumor volumes, as measured on T_2-weighted MR images 4 days after RT, were considered non-responders; all others were considered responders. Of 18 RT-treated mice, 14 were responders with the following tumor volume changes: 70.3% $\pm$ 16.7% of baseline at day 4 ($P <$ .0001) and 73.4% $\pm$ 11.1% at day 7 ($P =$ .0002); 4 were non-responders: 115.5% $\pm$ 7.1% at day 4 ($P =$ .090) and 140.3% $\pm$ 7.1% at day 7 ($P =$ .0008; **Figure S.3.1**). Responders and non-responders had similar baseline tumor volumes (2.61 $\pm$ 1.82 vs 2.81 $\pm$ 1.95 cm^3; $P =$ .85). **Figure 3.1** shows a representative serial imaging study using HP ^{13}C and multiparametric ^{1}H MRI in a mouse responding to RT.

Pyruvate-to-lactate conversion is the major energy-producing metabolic flux in aerobic glycolysis and is NADH-dependent. For responders, normalized HP [1-^{13}C]lactate (arbitrary unit) did not change substantially at day 1 ($P =$ .97; n $=$ 16), but it decreased significantly at day 4 by 0.05 $\pm$ 0.02 ($P =$ .023; n $=$ 15) and by 0.11 $\pm$ 0.02 at day 7 ($P <$ .0001; n $=$ 11; **Figure 3.2A**). In contrast, no significant changes were observed in non-responders at all three follow-up time points. A multilevel regression analysis revealed that nLac decreased significantly for responders ($P <$ .0001), but it increased slightly for non-responders ($P =$ .32), and their rates of change were significantly different ($P =$ .021; **Figure S.3.2A**).

We also evaluated the pyruvate-to-alanine conversion, an alternative and competing metabolic flux to pyruvate-to-lactate conversion. In contrast to post-RT [1-^{13}C]lactate changes, [1-^{13}C]alanine (% of voxels with detectable alanine; **Figure 3.2B**) increased 4.29% $\pm$ 3.64% at day 1 ($P =$ .25), 10.96% $\pm$ 3.76% at day 4 ($P =$ .006), and 11.68% $\pm$ 4.21% at day 7 ($P =$ .0086), with no significant changes for non-responders. A multilevel regression analysis revealed that HP alanine increased

51
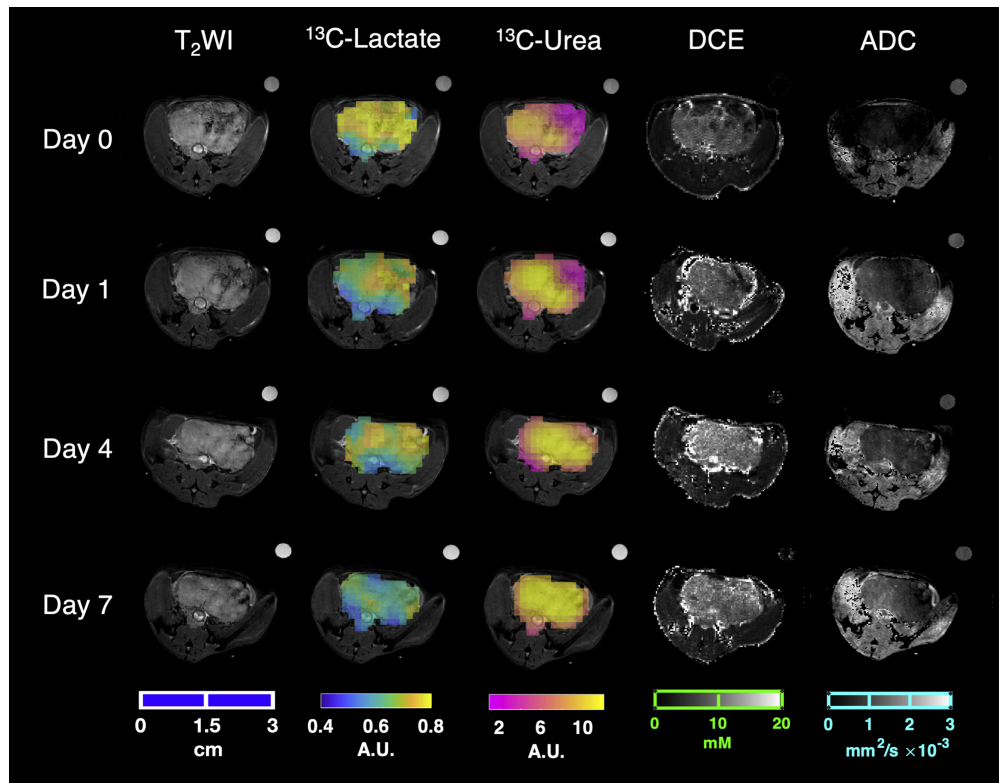
Figure 3.1: Representative images from a serial magnetic resonance imaging (MRI) study of a mouse prostate tumor responding to radiation therapy (RT). Tumor volume and hyperpolarized (HP) [1-^{13}C]lactate decreased after a single fraction RT administered on Day 0, whereas perfusion increased, as shown using HP [^{13}C]urea and dynamic contrast enhanced MRI. There was also an increase in the apparent diffusion coefficient in this tumor, which is inversely correlated with cellularity. A frequency-calibration phantom for HP ^{13}C scans can be seen in the upper right corner of the images.
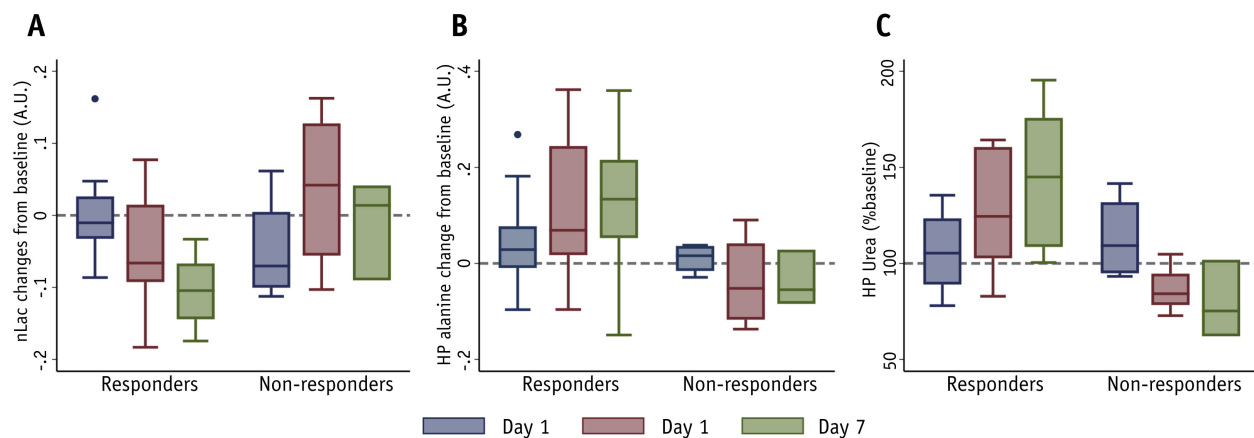
Figure 3.2: Changes in normalized hyperpolarized (HP) ^{13}C lactate, alanine, and urea after radiation therapy. (A) There is an apparent decrease in lactate, (B) an increase in alanine, and (C) increase in perfusion as seen in HP [^{13}C]urea in responders after radiation therapy. In contrast, there were no apparent changes in nonresponders (day 7 has 3 data points, with overlapping range bars and quantile bars). Multilevel regression analyses revealed a significant decrease in lactate and significant increases in alanine and urea for responders, and their directions and rates of change were significantly different from nonresponders.

significantly after RT in responders ($P = .0017$) and slightly decreased in non-responders ($P = .32$), with significantly different rates of change ($P = .013$; **Figure S.3.2B**).

HP [^{13}C]urea was coinjected with HP [1-^{13}C]pyruvate as an extracellular perfusion agent. For the responders, normalized HP [^{13}C]urea signal (arbitrary unit) slightly increased by $4.22\% \pm 7.13\%$ at day 1 relative to baseline ($P = .56$), but it increased significantly by $24.81\% \pm 7.34\%$ at day 4 ($P = .0017$) and $38.34\% \pm 8.24\%$ at day 7 ($P < .0001$; **Figure 3.2C**). A multilevel regression analysis (**Figure S.3.2C**) revealed that the normalized [^{13}C]urea signal increased significantly in responders ($P < .0001$), but it decreased significantly in non-responders ($P = .0037$), with significantly different rates of change ($P < .0001$). Finally, at pre-RT baseline, there were no significant differences between responders and non-responders in HP lactate, HP alanine, or HP urea ($P = .14$, .83, and .085, respectively).

3.3.2 DCE and DWI ^{1}H MRI corroborate HP ^{13}C MRI assessments of tumor physiology and microenvironment after RT

^{1}H DCE MRI and DWI were used to further evaluate tumor physiology and microenvironment changes after RT as a companion to HP ^{13}C MRI. For responders (n = 12), GBCA accumulation (iAUC; **Figure S.3.3A**) significantly increased ($P = .0003$) and wash-in slope (**Figure S.3.3B**)

significantly increased ($P = .0002$), with significantly enhanced wash-out slope (**Figure S.3.3C**; $P = .0075$), indicative of increased contrast delivery and clearance after RT. The non-responders (n = 4) showed the opposite changes: iAUC slightly decreased ($P = .39$) and wash-in slope slightly decreased ($P = .50$), with significantly different rates of change from responders ($P = .0072$ and .0099, respectively). The changes in wash-out slopes were not significantly different between responders and non-responders ($P = .32$). There were no significant differences at baseline between responders and non-responders in iAUC, wash-in slopes, or wash-out slopes ($P = .25, .22$, and $.90$, respectively). Finally, HP [^{13}C]urea signal significantly correlated with iAUC ($P = .049$) despite their considerably different imaging contrast mechanisms, quantification methods, and numerical scales (**Figure S.3.3D**).

As a functional imaging technique, DWI generates ADC maps that assess tissue cellularity. We found ADC ($\times 10^{-3}$ mm^2/s) to be slightly decreased in responders ($P = .17$; n = 14) and slightly increased in non-responders ($P = .15$; n = 4); the differences in ADC changes were close to statistical significance ($P = .057$; **Figure S.3.4**). Moreover, non-responder tumors had significantly lower ADCs at pretherapy baseline compared with responders (by $0.31 \pm 0.13 \times 10^{-3}$ mm^2/s; $P = .025$).

3.3.3 Intratumoral changes in hyperpolarized ^{13}C pyruvate-to-lactate conversion are radiation dose-dependent

Through radiation dose mapping, each tumor was segmented into high- (10-14 Gy), intermediate- (7-10 Gy), and low-dose (4-7 Gy) regions as shown in **Figure 3.3A**. Because we sought to investigate the localized dose-dependent tumor response to RT, responders or non-responders were not distinguished for dose analysis. We found that the magnitude of nLac changes from baseline was significantly associated with radiation dose (ANOVA: day 1, $P = .045$, n = 11; day 4, $P = .040$, n = 10; day 7, $P = .0003$, n = 9). High-dose regions showed significantly greater nLac decrease than low-dose regions as early as day 1, and the effect size also increased over time (**Figure 3.4B**: day 1, $P = .038$, Cohen's d = .71; day 4, $P = .042$, d = .75; day 7, $P = .0022$, d = 1.22; P values are adjusted for multiple comparisons). Furthermore, the decrease in nLac in the high-dose region at day 1 ($P = .07$) is an early indication of tumor response to RT, with subsequent significant decreases on days 4 and 7 ($P = .038$ and $.0003$, respectively). Intermediate-dose regions also showed a slight
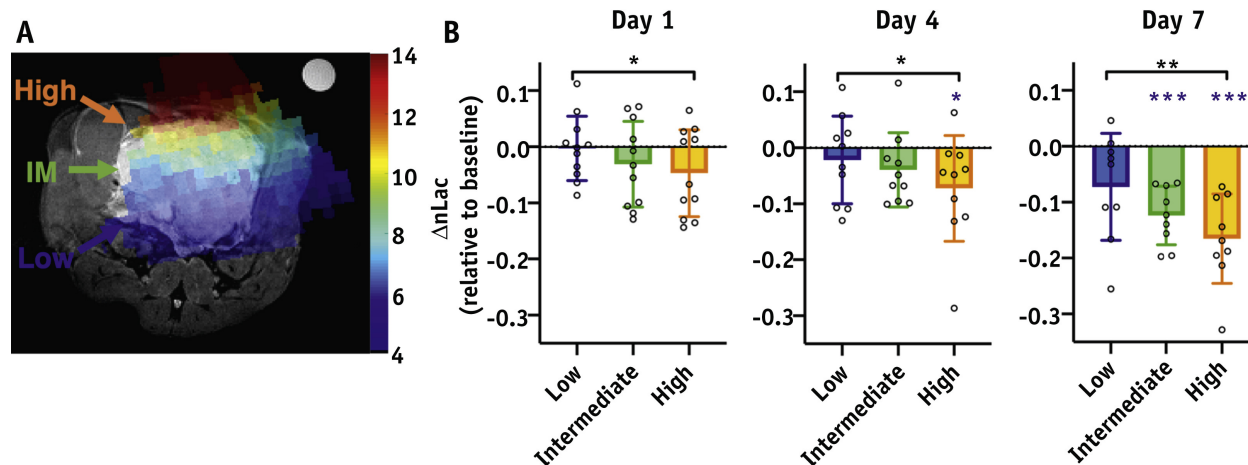
Figure 3.3: Intratumoral dose-dependent changes in HP ^{13}C pyruvate-to-lactate conversion. (A) A representative radiation dose distribution map is overlaid on a T_2-weighted magnetic resonance image. (B) There were significant associations between radiation dose and normalized HP lactate (nLac) changes at all time points. Moreover, high-dose regions (10-14 Gy) showed a greater magnitude of decreases in nLac compared with low-dose regions (4-7 Gy) as early as day 1. High-dose regions also showed significantly decreased nLac from baseline at days 4 and 7, and intermediate-dose regions also showed significantly decreased nLac from baseline at day 7. $*P < .05$; $*P < .01$; $***P < .001$. Black asterisks indicate significant differences between high and low dose; blue asterisks indicate significant changes from baseline. (Abbreviations: IM, intermediate; nLac, normalized [1-^{13}C]lactate signal.)

decrease at day 4 ($P = .092$) and a significant decrease at day 7 ($P = .0001$), but there were no significant changes in the low-dose regions. Because the intratumoral heterogeneity at pretherapy baseline is a confounding factor, we compared multiple baseline MRI quantifications among 3 dose regions and found no significant difference in baseline intratumoral nLac ($P = .10$). Comparisons of other baseline MRI quantifications are reported in **Figure S.3.5**.

3.3.4 *Ex vivo* correlative studies showed dose-dependent decreases in markers of tumor proliferation and glycolysis after radiation therapy

In tumor regions treated with high-dose radiation, the histologic sections showed hypocellularity with necrosis and fibrosis (**Figure 3.4A**, H&E), nuclear shrinkage, and vacuolation; low-dose regions showed similar changes but to a lesser degree. In contrast, the untreated control tumor exhibited high cellularity, nuclear atypia, and no vacuolation on histology. Quantitively, high-dose regions showed significantly higher necrosis and fibrosis than low-dose regions and untreated controls did (**Figure 3.4B**; $P = .0024$ and $.029$, respectively), and significantly lower anti-Ki-67 staining
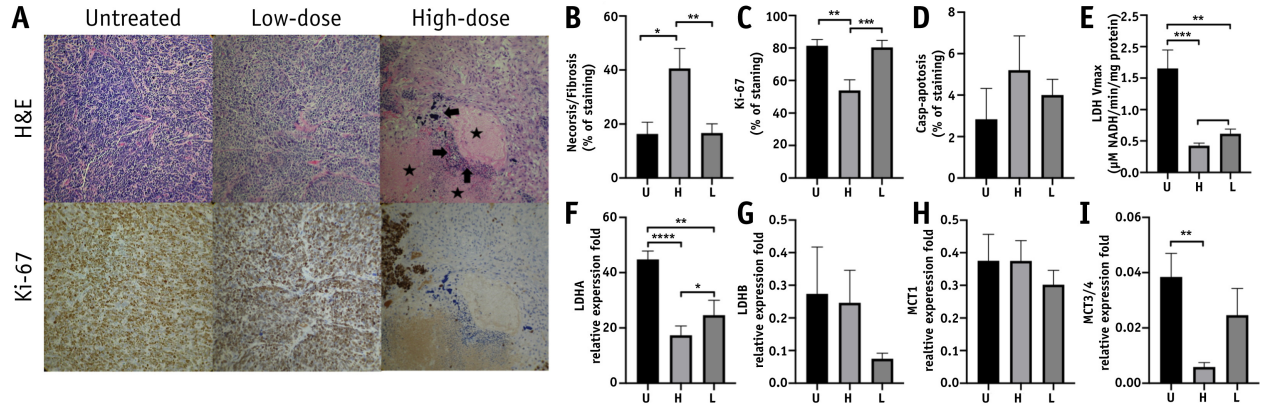
Figure 3.4: Dose-dependent changes in immunohistochemical and molecular markers.
(A) Tumor regions treated with high radiation dose showed significantly more necrosis or fibrosis (arrows indicate frank necrosis; stars indicate frank fibrosis) on H&E staining and (B) lower Ki-67 (a proliferation marker) staining (C) compared with their corresponding low-dose regions and a separate cohort of untreated TRAMP tumors (original magnification ×20). (E) Moreover, high-dose tumor regions showed lower lactate dehydrogenase (LDH) activity, (F) LDHA expression, and (I) MCT3/4 expression compared with low-dose regions, consistent with the decreased hyperpolarized ^{13}C lactate signal observed in the high-dose regions. (D) In addition, high-dose regions showed slightly higher anti-caspase-3 (an apoptosis marker) staining, (G) higher LDHB expression, and (H) lower MCT1 expression compared with low-dose regions or untreated tumors, but these differences were not statistically significant. ($*P < .05$; $**P < .01$; $***P < .001$; $****P < .001$. Abbreviations: H, high; H&E, hematoxylin and eosin; L, low; U, untreated.)

(Fig. 4C; $P = .0002$ and $.0018$, respectively). High-dose regions also showed non-significantly higher anti-Caspase-3 staining (an apoptosis marker) compared with untreated tumors (**Figure 3.4D**).

The high-dose regions showed decreased LDH enzyme activity compared with low-dose regions and untreated tumors (V_{max}, μM NADH/min/[protein]; $P = .042$ and $.0001$, respectively) and LDHA expression (relative expression fold; $P = .022$ and $P < .0001$, respectively), as shown in **Figure 3.4E, F**. Similarly, the low-dose region showed lower LDH activity and LDHA expression compared with untreated tumors ($P = .0067$ and $.0014$, respectively). Moreover, there was a weak correlation between LDH activity and HP ^{13}C lactate signal change on a per-subject basis ($P = .16$). We also found the expression of LDHB, the competing isoform to LDHA, was slightly higher in the high-dose regions than in low-dose regions, but the difference was not statistically significant (**Figure 3.4G**). In addition, there was no significant differences in MCT1 (the transporter responsible for pyruvate import) among 3 groups (**Figure 3.4H**), but high-dose regions exhibited significantly lower expression of MCT 3/4 (the transporter responsible for lactate export) compared

56

with low-dose regions and untreated tumors ($P = .16$ and $.0054$, respectively; **Figure 3.4I**).

3.4 Discussion

Although enormous progress has been made in RT precision and efficacy, many patients still experience cancer recurrence after RT. Noninvasive, sensitive imaging markers of tumor response to RT are needed to personalize patient care. In this study, we used HP ^{13}C and multiparametric ^{1}H MRI to characterize early and dose-dependent tumor response to RT, accomplished by co-administration of HP [1-^{13}C]pyruvate and HP [^{13}C]urea in TRAMP mice that were also imaged with DCE MRI and DWI. We found that in TRAMP tumors responding to RT, HP [1-^{13}C]lactate production decreased significantly, with a concomitant increase in alanine production and tumor perfusion as measured by both HP ^{13}C urea and DCE MRI. In contrast, the opposite changes were observed in tumors that did not respond to RT. The MRI changes after RT are consistent with the tumor pathophysiology and their response to radiation. Glycolytic metabolism and perfusion are interrelated and central to tumor biology [46]. Radiation-induced DNA damage causes cell cycle arrest or death, effectively halting tumor proliferation and metabolic demands. The decreased HP ^{13}C pyruvate-to-lactate conversion is consistent with the decreased LDHA expression and LDH enzyme activity. Moreover, radiation-induced reactive oxygen species deplete NADH [145], the cofactor required for pyruvate-to-lactate conversion, thus contributing to the decreased lactate production.

The transamination of pyruvate to alanine is an alternative and competing enzymatic flux to the reduction of pyruvate to lactate, and we found that HP lactate and alanine changed in the opposite directions after RT, consistent with the observation when NAD biosynthesis was inhibited in a prior study [80]. Radiation-induced inflammation is a confounding factor for interpretation of HP lactate. The activation and infiltration of immune cells (which are highly metabolic active) could elevate the HP ^{13}C lactate signal in tumor tissue responding to RT. However, the significantly decreased post-RT lactate suggests that metabolic remission is the predominate biological process responsible for the HP ^{13}C lactate change. Finally, the increased tumor perfusion seen with HP [^{13}C]urea MRI and DCE might be related to increased permeability from radiation-induced vascular damage and inflammation. Overall, the synergy between metabolic and perfusion imaging is evident

in this study, providing sharp contrasts and sensitive metrics for therapy evaluation. Together, these results suggest that decreased lactate production, increased alanine production, and increased perfusion are acute tumor response to effective RT. Conversely, increased lactate production with decreased alanine production and perfusion are indicative of aggressive and radio-resistant tumor phenotypes.

With a radiation dose mapping technique, we found a continuum of radiation dose-dependent effect in HP ^{13}C lactate decreases (high-dose regions exhibit greater changes than intermediate-dose regions, which show greater changes than low-dose regions), consistent with dose-dependent changes in cell proliferation, and LDH expression and activity observed in the ex vivo correlative studies. Moreover, this localized dose dependency was observable as early as day 1 and became more evident at days 4 and 7. The large effect size (Cohen's d >1.2) of HP [1-^{13}C]lactate change at day 7 after RT, an optimal intervention window, marks HP [1-^{13}C]lactate as a desirable imaging marker for further clinical investigation. With the wide use of dose escalation techniques, a dose-dependent functional imaging metrics could be an invaluable tool for RT planning and evaluation. However, few imaging studies have explored the radiation dose-dependent effects [146, 147]. Our study, for the first time, demonstrated the radiation dose-dependent effects in a tumor model using noninvasive *in vivo* imaging techniques.

The HP ^{13}C MRI findings should be interpreted in the context of other preclinical studies. Matsuo et al [148] found that 5 Gy irradiation caused increased tumor HP lactate production and decreased perfusion 24 hours after RT. In addition, Sandulache et al [139] showed that 5 Gy irradiation caused a transient decrease (about 30 minutes) in HP lactate signal in cancer cells. The RT regimens used in these 2 studies correspond to the low-dose tumor regions in our study. In a few low-dose tumor regions, we observed slightly increased lactate production on days 1 and 4 (**Figure 3.1**); however, for the whole cohort, no significant changes in the low-dose regions were observed. These data suggest that higher radiation doses are required to render metabolic changes detectable by HP [1-^{13}C]pyruvate MRI. Indeed, Day et al [78] showed that when rats bearing glioma tumors were treated with 15 Gy radiation, HP ^{13}C lactate signal diminished significantly 3 days after RT, with associated prolonged survival. In addition, Chen et al [79] observed a decreased HP ^{13}C lactate-to-pyruvate ratio 4 days after 8 Gy irradiation but found no significant changes in perfusion.

In this study, we adopted multiparametric ^{1}H MRI – namely, DCE MRI and DWI – as companion imaging markers, and we compared HP ^{13}C MRI against clinical standard techniques for RT assessments. DCE MRI demonstrated the same contrastive perfusion changes between responders and non-responders, and there was a correlation between DCE iAUC and HP ^{13}C urea MRI on a per-subject basis, validating the efficacy of HP ^{13}C urea MRI as a perfusion imaging technique. The main advantage of HP [^{13}C]urea is that it can be combined with other HP ^{13}C probes in a single imaging session, providing assessments of probe delivery and tissue perfusion in addition to metabolic pathways. Moreover, compared with Gd-based DCE MRI, urea is an endogenous compound with almost no toxicity.

RT renders complex tissue microenvironment changes such as cellular edema in the short term (lowering ADC) and decreased cellularity long term (increasing ADC). Thus, this opposing change complicates the interpretation of ADC in the context of RT assessment. Although we found that non-responders had significantly lower baseline ADC than responders did, there were no significant changes in ADC after RT; in fact, ADC slightly decreased for responders and increased for non-responders. Previous literature has reported that a lower post-RT ADC indicates favorable outcomes in patients with glioma [141, 149], whereas an increased post-RT ADC is a favorable prognostic factor in patients with hepatocellular carcinoma [150]. This study suggests that HP ^{13}C MRI could provide diagnostic information that is potentially unavailable from conventional ^{1}H multiparametric MRI.

Our study has several limitations. First, animal models do not fully recapitulate human tumor biology. Hypoxia is a common feature of rodent tumors, especially for large-sized tumors [151]. Ventral sides of tumors (high-dose regions) experience more diffusion-limited hypoxia and are therefore more radio-resistant; indeed, we found that baseline high-dose tumor regions had a slightly lower lactate metabolism, significantly lower urea perfusion, significantly slower DCE wash-out slopes, and significantly higher cellularity compared with lower dose regions (dorsal side; Fig. E5).

Despite the potential radio-resistant phenotypes, we observed a greater magnitude of lactate decrease in the high-dose regions, suggesting that HP ^{13}C lactate is a sensitive marker for RT response. Moreover, given the high cellularity of TRAMP tumors, perfusion imaging metrics are heavily weighted by extracellular space and interstitial volume [24], in contrast to human tumors in which enhanced vascularization is the underlying pathophysiology. Another limitation of the study

is that DCE, DWI, dose mapping, or tissue collection were not performed for all subjects because of technical and logistical constraints. However, because each analysis was relatively independent, the unbalanced sample size should not significantly affect the main findings. Moreover, statistical significance should be interpreted with caution given the relatively small sample sizes; additional studies are needed to validate the observations, especially in clinical settings. Finally, we used multiple follow-up studies to characterize the post-RT changes, which are not clinically feasible. In future clinical studies, simple pre- and post-RT comparisons should be performed.

3.5   Conclusion

We demonstrated that simultaneous metabolic and perfusion imaging with HP ^{13}C MRI could assess early and dose-dependent tumor response to RT in a PCa mouse model. This report highlights the clinical translation potential of HP ^{13}C MRI, which is currently being investigated at multiple sites as a cancer diagnosis and therapy monitoring tool. The findings of this study provided the basic science premise for further clinical investigation. With tumor-specific functional evaluations provided by metabolic and perfusion imaging, radiation oncologists could potentially personalize treatment regimens, verify radiation dose delivery, and discern treatment response or failure.

3.6 Supplementary Information

3.6.1 Methods: Imaging Protocol and Parameters

Hyperpolarized ^{13}C MRI. Dynamic nuclear polarization of ^{13}C-enriched substrates was performed on a HyperSense™ polarizer (Oxford Instruments, Abingdon, UK); 24 µL neat [1-^{13}C]pyruvic acid (with 16.5 mM GE trityl radical and 1.5 mM Gd-DOTA) and 55µL [^{13}C]urea (6.4 M in glycerol, with 17.5 mM OX63 radical and 0.2 mM Gd-DOTA) were co-polarized by sequentially freezing pyruvic acid and urea to the cryovial. After approximately 1 hour of polarization, the frozen sample was rapidly dissolved in 4.5 mL heated buffer (40 mM Tris-HCl, 80 mM NaOH, and 0.3 mM Na$_2$EDTA), resulting in an 80 mM sodium [1-^{13}C]pyruvate and 75 mM [^{13}C]urea solution at a physiologic temperature and pH, and 350uL of which was immediately injected into the mouse via tail vein over 15 s. Following the injection of HP ^{13}C substrates, ^{13}C metabolite-specific imaging was performed using a single-shot, three-dimensional (3D) GRadient And Spin Echo (GRASE) sequence to image HP [1-^{13}C]lactate, [1-^{13}C]alanine, [1-^{13}C]pyruvate, [^{13}C]urea, and HP001 (a frequency-calibration phantom) sequentially with a 1.25 mm isotropic resolution as previously described. The images were acquired at 45 s after the start of the injection with 0.78 s total scan time. The acquisition timing after HP ^{13}C agent injection was chosen based on a pilot study where 5 TRAMP mice were imaged by 1D slice-selective dynamic spectroscopy to achieve optimal and stable lactate signal. The 3D GRASE ^{13}C magnitude images were reconstructed to a 1.25 cc isotropic resolution.

Multiparametric ^{1}H MRI. T_2-weighted axial anatomical images were acquired for co-localization with ^{13}C images and radiation dose maps using a multi-slice spin-echo pulse sequence of following parameters: 90° flip angle, TE/TR = 20/1200ms, 40 × 40 mm FOV, 256 × 256 matrix size, 0.1563 × 0.1563 mm2 in-plane resolution, and 1.25 mm slice thickness. DWI was performed using a similar multi-slice spin-echo sequence with single direction diffusion-sensitizing gradients and b-values of 18.60, 181.74, 324.49, 508.03 s/mm^2. All ^{1}H spin-echo sequence acquisitions are performed prior to HP MRI studies and with respiration gating.

DCE MRI was performed after HP ^{13}C imaging with a multi-slice gradient echo sequence of the following parameters: TE/TR =1.11/39 ms, 40° flip angle, 128 × 128 matrix, 40 ×40 mm^2 FOV, 0.3125 × 0.3125 mm^2 in-plane resolution, 1 mm slice thickness with 0.25 mm gap, total 10 slices,

40 dummy scans, and 5 s temporal resolution with total 50 time points. After the five baseline scans, a bolus of Gd-DTPA (0.27 mmol/kg, Magnevist®, Bayer Healthcare, Whippany, NJ) was injected via the tail vein over 15 s followed by 150 μL of saline flush. Before DCE scans, native T_1 maps were acquired using the same gradient echo sequence with variable flip angles of 2, 5, 15, 25, 35, and 50 degrees.

3.6.2 Methods: Analysis of Dynamic Contrast Enhanced (DCE) MRI

The MR signal for spoiled gradient echo sequence is defined by

$$S = S_0 \cdot \sin\theta \cdot \frac{1 - e^{-TR/T_1}}{1 - \cos\theta \cdot e^{-TR/T_1}} \cdot e^{-TE/T_2^*} \tag{3.1}$$

Where S is the MR signal, S_0 is the native equilibrium longitudinal magnetization, θ is the flip angle, TR is repetition time, TE is echo time, T_1 is longitudinal relaxation constant, T_2^* is the transverse relaxation constant. Since $TE << T_2^*$, the equation above can be rewritten as

$$\frac{S}{\sin\alpha} = m \cdot \frac{S}{\tan\alpha} + S_0 \cdot (1 - m) \tag{3.2}$$

where m is e^{-TR/T_1} and can be estimated by linear fitting MR signal obtained with gradient echo sequence of variable flip angles to the rewritten equation, resulting in native T_1 maps, which was subsequently used to estimate post-contrast T_1 by solving the following question

$$\frac{S(t)}{S_{pre}} = \frac{1 - e^{-TR/T_1(t)}}{1 - e^{-TR/T_{10}}} \cdot \frac{1 - \cos\theta \cdot e^{-TR/T_{10}}}{1 - \cos\theta \cdot e^{-TR/T_1(t)}} \tag{3.3}$$

where S_{pre} is baseline MR signal prior to contrast agent injection, and T_{10} is native T_1. The concentration of Gadolinium-based contrast agent (GBCA) was then estimated by the change is in T_1 after GBCA administration using

$$r_1 \cdot C(t) = \frac{1}{T_1(t)} - \frac{1}{T_{10}} \tag{3.4}$$

Where r1 is 3.58 $s^{-1}mM^{-1}$ [152].

The following semi-quantitative parameters were calculated based on dynamic GBCA concen-

tration: 1) area under the curve (AUC): sum of GBCA concentration of all time points; 2) initial area under the curve (iAUC): sum of GBCA concentration from contrast agent arrival to 90s after the arrival; 3) wash-in slope: approximate derivative of dynamic GBCA concentration curve from bolus arrival to the peak; 4) wash-out slope: the slope of linear regression of GBCA concentration from the time of peak enhancement to the last time point, with positive slopes (persistent enhancement) allowed.

3.6.3 Methods: Biological Correlation

Tissue collection and histopathology. For each high and low dose tumor region, part of tissue was formalin-fixed and paraffin-embedded (FFPE) for histological analysis, and the other part was quick-frozen for transcriptomic analysis. FFPE tissue blocks were cut into 5 µm thick sections on a Leica microtome (Buffalo Grove, IL, USA), then stained with hematoxylin and eosin (H & E), anti-Ki-67, and anti-caspase-3 (ASP175) monoclonal antibodies. The tumor histopathology was evaluated, and the percentage of cells with immunohistochemical staining was graded by a medical oncologist. The percentages of poorly differentiated cells were similar among high-dose, low-dose, and control tumors (high: $97.25 \pm 2.92\%$, low: $96.88 \pm 1.96\%$, control: $95.20 \pm 7.05\%$), suggesting that treated tumors are of similar histological grades as untreated control tumors.

Gene expression analysis. Total RNA was extracted and purified from frozen tissues with RNeasy procedure kit (Qiagen, Germantown, MD). The quality of RNA was confirmed using an RNA 6000 Nano Chip kit (Agilent, Santa Clara, CA). Reverse transcription was performed using the iScript cDNA Synthesis kit (Bio-Rad Laboratories, Hercules, CA). Quantitative PCR was performed in triplicate for the lactate dehydrogenase-α (LDH-A), lactate dehydrogenase-β(LDHB), the monocarboxylate transporters 1, 2, and 4 (MCT1, 2, 4), Hif1-α, VEGF, glucose transporter 1 and 5 (Glut1,5), and hexokinase 2 (HK2) on an ABI 7900HT RT-qPCR system (Applied Biosystems, Foster City, CA). L19, a nonregulated ribosomal housekeeping gene, was used as the reference gene for expression quantification.

LDH enzyme activity assay. Frozen tissue was analyzed for LDH activity using a colorimetric assay, as previously described. The maximum velocity (V_{max}) was estimated using the Lineweaver-Burke plot. The protein concentration of tissue supernatant was also quantified with a Bradford protein assay (Bio-Rad Laboratories, Hercules, CA) as a normalization reference.

3.6.4 Methods and Results: multilevel regression analyses

Multilevel regression analyses were performed to examine the temporal changes and the interaction between time and response using the means of whole-tumor imaging metrics. This linear mixed model analysis was performed using `mixed` function in Stata 16 (StataCorp LLC, College Station, TX), We specified an unstructured covariance model with random intercepts at level two (individual tumor/animal level) and allowing random slopes did not improve the model assessed by Akaike Information Criterion, AIC). We employed a restricted maximum likelihood estimation (RMLE) algorithm for model fitting and the Kenward-Roger method for small sample inference. The statistical analysis output are reported in the Table S1.

When "time" was used as a categorical variable (each time point as a group compared to baseline), changes relative to baseline were obtained and reported in the main text. When "time" was used as a continuous variable, the overall linear trends in imaging parameters after radiation therapy (RT) were obtained. For responders (n = 14), normalized [1-^{13}C]lactate (nLac) decreased significantly at a rate of .0163 $\pm$ .0031/day ($P < 0.00005$) from a baseline of .6714 $\pm$ .0191. In contrast, nLac of responders slightly increased at a rate of .0053 $\pm$ .0052/day ($P = 0.3195$) from a baseline of .6118 $\pm$ .0340. The baselines of responders and non-responders were not significantly different ($P = .1413$). Moreover, there was a significant interaction between "time" and "response" ($P = .0010$), suggesting the significantly different post-RT changes in nLac between responders and non-responders.

The opposite changes were observed for [1-^{13}C]alanine and [^{13}C]urea. For responders, normalized alanine (percentage of voxels with detectable alanine) significantly increased after radiotherapy at a rate of .0176 $\pm$ .0053/day ($P = .0017$) from a baseline of .1447 $\pm$ .0367; normalized urea (arbitrary units) significantly increased at a rate of .3283 $\pm$ .0597 ($P < .0001$) from a baseline of 5.7093 $\pm$ 0.4934. In contrast, non-responders showed slightly decreased alanine at a rate of .0090 $\pm$ .0088/day ($P = .3162$) from a baseline of .1606, and also significantly decreased urea at a rate of .3084 $\pm$ .1000/day ($P = .0037$) from a baseline of 7.5549 $\pm$ .8840. There were also significant interactions between time and response for both alanine and urea ($P = .0132$ and $P < .0001$, respectively), suggesting responders and non-responders have distinct changes in alanine and urea after RT. The urea and alanine baseline differences between responders and non-responders were not statistically

significant ($P = .7737$ and $P = .0851$, respectively). The linear changes of hyperpolarized ^{13}C MR estimated from multilevel regression were shown in **Figure S.3.2**.

Similar procedures were performed to analyze changes in dynamic contrast enhanced (DCE) MR parameters and apparent diffusion coefficient (ADC) maps, and the regression results were shown in **Figure S.3.3** and **Figure S.3.4**. Briefly, we observed significant increases in DCE initial area under the curve (iAUC) and the wash-in slopes for responders, and these changes were significantly different from non-responders. DCE wash-out slopes were significantly enhanced for responders, and also slightly enhanced for non-responders; the interaction between time and response were not significantly different for wash-out slopes. No significant differences between responders and non-responders were found in DCE parameters. ADC slightly decreased for responders and slightly increased for non-responders, and the interaction between time and response was close to statistical significance.

Table S.3.1: Multilevel regression analysis of imaging metrics to evaluate changes after radiation therapy.

Imaging Metrics	Responders: rate of change (/day)	Non-responders: rate of change (/day)	Rate of changes difference*	Baseline difference*
Lactate (A.U.)	-.0163 ± .0031 ($P < .0001$)	.0053 ± .0052 ($P = .3195$)	.0215 ± .006 ($P = .0010$)	.6714 ± .0191 vs. .6118 ± .0340 ($P = .1413$)
Alanine (A.U.)	.0176 ± .0053/day ($P = .0017$)	- .0090 ± .0088 ($P = 0.3162$)	-.0266 ± .0103 ($P = .0132$)	.1447 ± .0367 vs. .1606 ± .0657 ($P = .8343$)
Urea (A.U.)	.3283 ± .0597 ($P < 0.0001$)	-.3084 ± .1000 ($P = .0037$)	-.6367 ± .1165 ($P < .0001$)	5.7093 ± .4935 vs. .1606 ± .0657 ($P = .0851$)
iAUC (mM)	.2214 ± .0053 ($P = .0003$)	-.0788 ± .0901 ($P = .3878$)	-.3002 ± .1058 ($P = .0072$)	3.7482 ± .3672 vs. 4.6077 ± .6408 ($P = .2589$)
Wash-in (mM/min)	.0910 ± .0222 ($P = .0002$)	.0246 ± .0326/ ($P = .5018$)	-.1156 ± .0425 ($P = .0099$)	1.4542 ± .1384 vs. 1.8092 ± .2417 ($P = .2171$)
Wash-out ($\times 10^{-2}$ mM/min)	-.1286 ± 0.0455 ($P = .0075$)	-.0414 ± .0741 ($P = .5795$)	.0871 ± .0870 ($P = .3227$)	-1.3914±.3112 vs. -1.3122±.5429 ($P = .9006$)
ADC ($\times 10^{-3}$ mm^2/s)	-.0193 ± .0137 ($P = .1660$)	.0370 ± .0253 ($P = .1505$)	.0563 ± .0288 ($P = .0566$)	.9366 ± .0637 vs. .6290 ± .1149 ($P = .0270$)

*the difference between responders and non-responders

3.6.5 Supplementary Figures
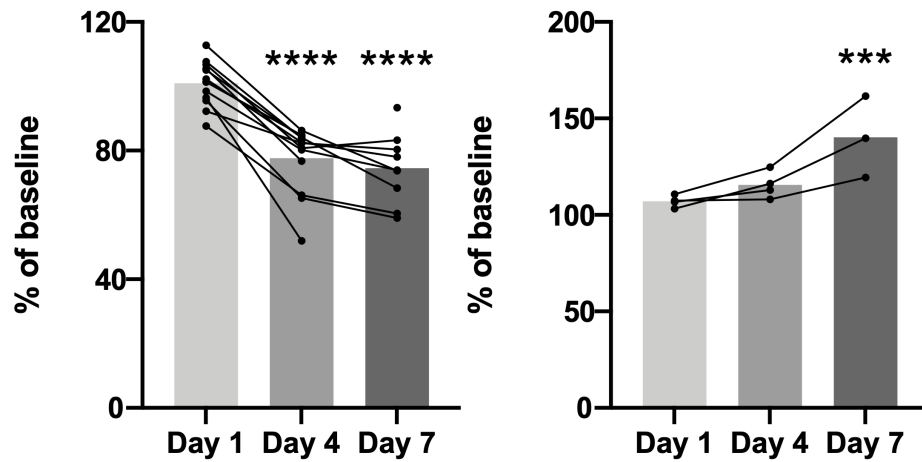
Figure S.3.1: Changes in tumor volume following radiotherapy. Fourteen mice showed significantly decreased tumor volume (responders), while 4 mice shown continued tumor growth after radiotherapy (non-responders) (*$P < .05$, ***$P < .001$, ****$P < .0001$).
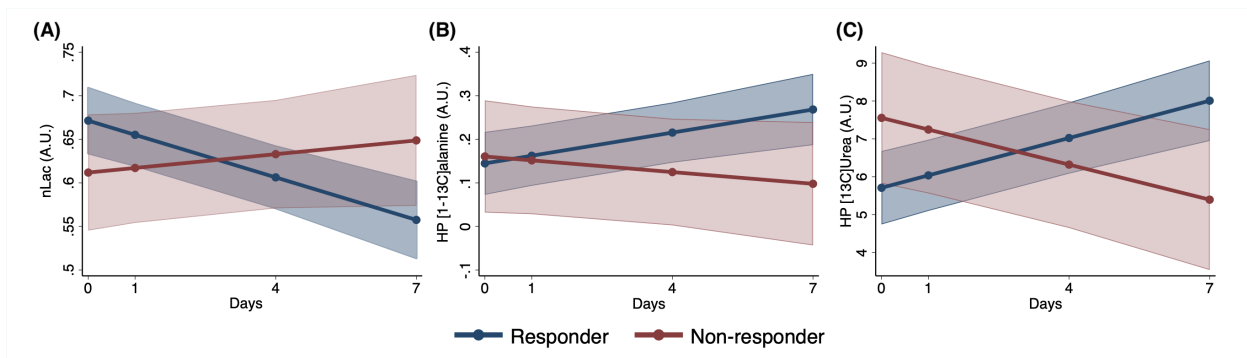
Figure S.3.2: Linear changes in normalized hyperpolarized (HP) [1-^{13}C]lactate (nLac), [1-^{13}C]alanine, and [^{13}C]urea after radiotherapy was estimated by multilevel analyses. After radiotherapy, tumors responded well for therapy (responders) showed significantly decreased HP lactate signal, and significantly increased HP alanine signal and HP urea signal; moreover, the rates of these changes were significantly different from non-responders.
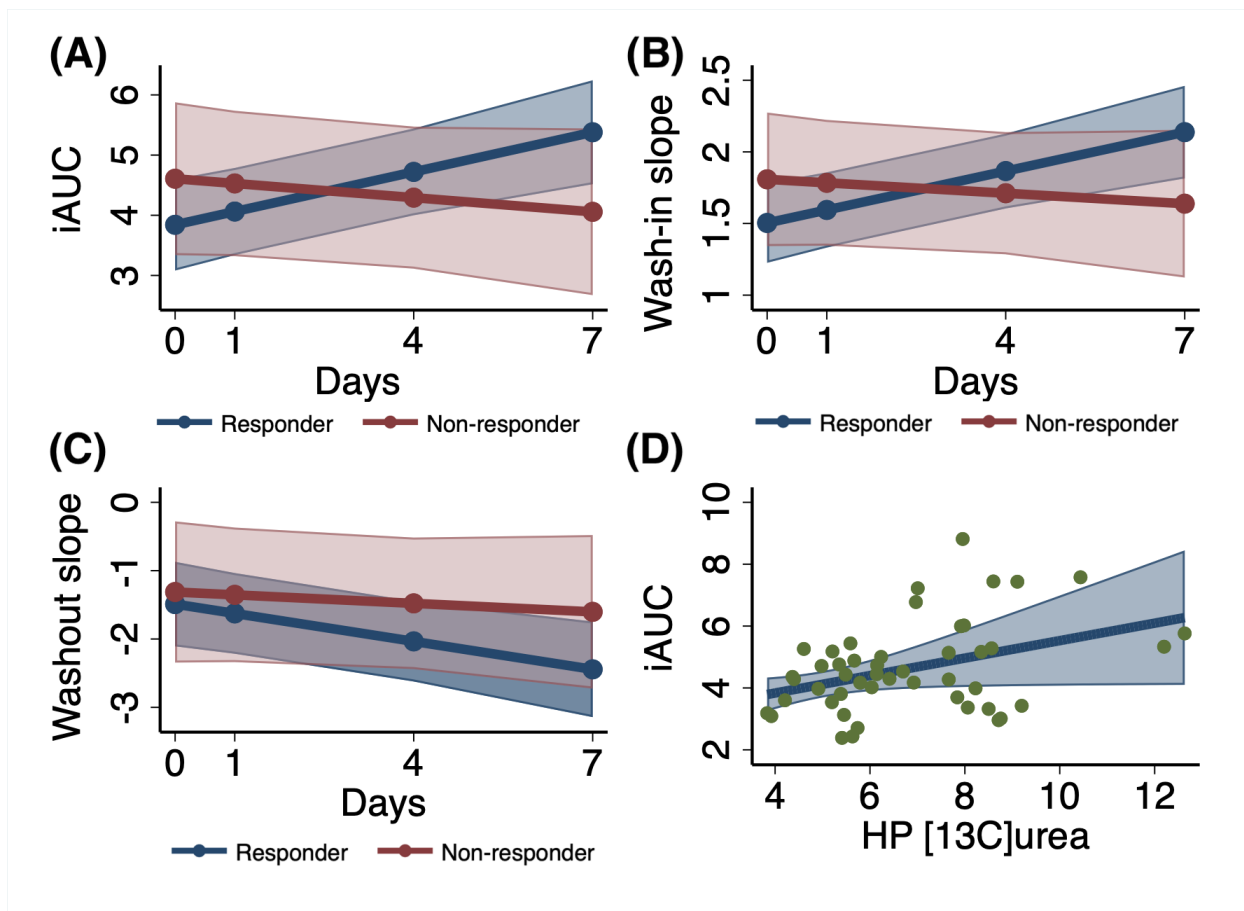
Figure S.3.3: Hyperpolarized (HP) [^{13}C]urea and dynamic contrast enhanced (DCE) MR provide corroborative measurements of tumor perfusion. (A, B, C) Consistent with HP [^{13}C]urea findings, DCE parameters, including initial area under the curve (iAUC, mM), wash-in slopes (mM/min), and wash-out slopes ($\times 10^{-2}$ mM/min), demonstrated significantly enhanced perfusion after radiotherapy for responders; moreover, these changes were significantly different from non-responders. (D) Despite their considerably different imaging contrast mechanisms, quantification methods, and numerical scales, HP [^{13}C]urea signal showed a significant correlation with DCE iAUC.
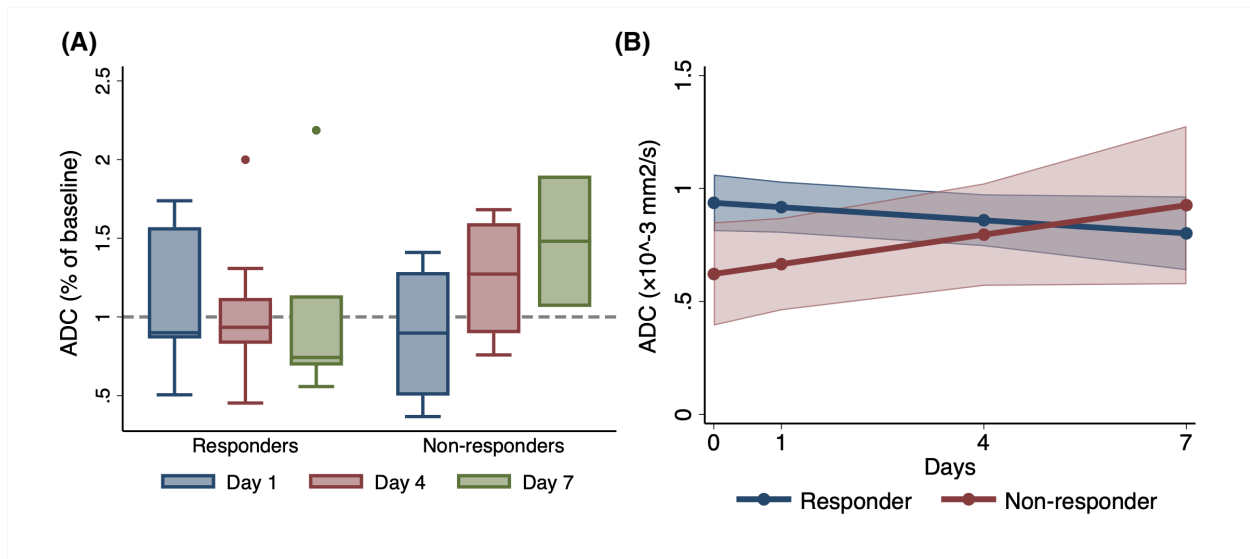
Figure S.3.4: Apparent diffusion coefficient (ADC) changes after radiation therapy (RT). (A) Box plots shows the distribution of ADC changes across follow-up time points, contrasting responders and non-responders. (B) Linear ADC changes for responders and non-responders estimated from multilevel regression: ADC slightly decreased in responders ($P = 0.1660$) and slightly increased in non-responders ($P = 0.1505$); their rates of change were not statistically significant ($P = 0.0566$). Moreover, the responder tumors had significantly higher ADC than non-responders ($P = 0.00253$), as shown by the distinct intercepts on the regression plot.
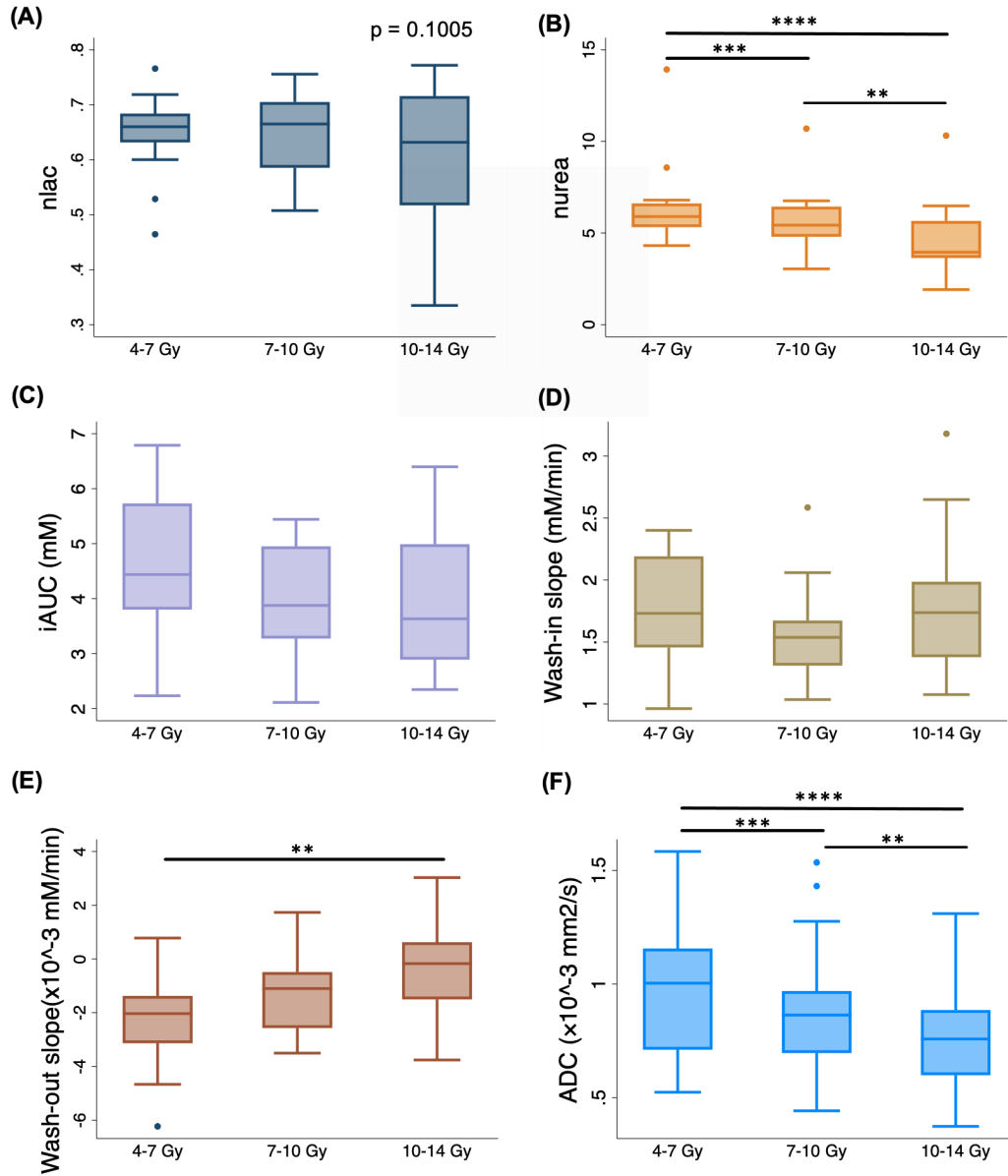
Figure S.3.5: Intratumoral heterogeneity at baseline pre-radiotherapy scans. Tumor regions treated with high-dose radiation (10-14 Gy) had significantly lower normalized hyperpolarized [^{13}C]urea (nurea), slower DCE wash-out slopes, and lower apparent diffusion coefficient (ADC) than regions treated with lower dose (intermediate: 7-10 Gy, low: 4-7 Gy). No significant differences were observed in normalized HP [1-^{13}C]lactate (nLac), initial area under the curve (iAUC), and DCE wash-in slope among high-dose, intermediate-dose, and low-dose regions. (A) Lactate: repeated measures ANOVA, $P = 0.1005$. (B) Urea: $P < 0.00005$; high vs low: -1.93 $\pm$ 0.27, $P < 0.00005$; high vs intermediate: -1.07 $\pm$ 0.27, $P = 0.0012$; intermediate vs. low: -0.86 $\pm$ 0.27, $P = 0.0095$. (C) iAUC (mM): $P = 0.0592$. (D) DCE wash-in slope (mM/min): $P = 0.2206$. (E) DCE wash-out slopes (x 10-2 mM/min): $P = 0.0027$, high vs low: 1.87 $\pm$ 0.47, $P = 0.0021$; high vs. intermediate 0.81 $\pm$ 0.47, $P = 0.2764$; intermediate vs. low: 1.06 $\pm$ 0.0021, $P = 0.1040$. (F) ADC ($\times$ 10-3 mm2/s): $P < 0.00005$; high vs low: -0.196 $\pm$ 0.025, $P < 0.00005$; high vs. intermediate: 0.092 $\pm$ 0.025, $P = 0.0012$; intermediate vs. low: 0.075 $\pm$ 0.023, $P = 0.0003$) (** $P< 0.01$, *** $P < 0.001$, **** $P < 0.0001$).

Chapter 4: Clinical Translation of Hyperpolarized ^{13}C Pyruvate and Urea MRI for Simultaneous Metabolic and Perfusion Imaging

Abstract

Purpose: The combined hyperpolarized (HP) ^{13}C pyruvate and urea MRI has provided a simultaneous assessment of glycolytic metabolism and perfusion for improved cancer diagnosis and therapeutic evaluation in preclinical studies. This work aims to translate this dual-probe HP imaging technique to clinical research.

Methods: A co-polarization system was developed where [1-^{13}C]pyruvic acid (PA) and [^{13}C, ^{15}N$_2$]urea in water solution were homogeneously mixed and polarized on a 5 T SPINlab™ system. Physical and chemical characterizations and the toxicology study of the combined probe were performed. Simultaneous metabolic and perfusion imaging was performed on a 3 T clinical MR scanner by alternatively applying a multi-slice 2D spiral sequence for [1-^{13}C]pyruvate and its downstream metabolites and a 3D balanced steady-state free precession (bSSFP) sequence for [^{13}C, ^{15}N$_2$]urea.

Results: The combined PA/urea probe has glass-formation ability similar to neat PA and can generate nearly 40% liquid-state ^{13}C polarization for both pyruvate and urea in 3-4 hours. A standard operating procedure for routine on-site production was developed and validated to produce 40 mL injection product of approximately 150 mM pyruvate and 35 mM urea. The toxicology study demonstrated the safety profile of the combined probe. Dynamic metabolite-specific imaging of [1-^{13}C]pyruvate, [1-^{13}C]lactate, [1-^{13}C]alanine, and [^{13}C, ^{15}N$_2$]urea was achieved with adequate spatial (2.6 mm × 2.6 mm) and temporal resolution (4.2 s), and urea images showed reduced off-resonance artifacts due to the J_{CN} coupling.

Conclusion: The reported technical development and translational studies will lead to the first-in-human dual-agent HP MRI study and mark the clinical translation of the first HP ^{13}C MRI probe after pyruvate.

4.1 Introduction

With cancer therapeutic advancements contributing to a decrease in cancer mortality rate [153], new diagnostic tools are needed to guide treatment selection and disease management. *In vivo* tumor biology assessment afforded by molecular imaging is essential for tumor phenotype characterization and early evaluation of therapeutic response or resistance. Metabolism and perfusion are desirable imaging targets as altered cellular metabolism and tissue perfusion are mechanistically involved in cancer pathophysiology [154, 32, 155]. Combined metabolic and perfusion imaging techniques, such as [^{15}O]water and [^{18}F]fluorodeoxyglucose (FDG) positron emission tomography (PET), have been used clinically to identify aggressive breast [156], lung [157], and cervical [59] tumors and to evaluate tumor response to therapy [158, 159]. However, multi-probe PET scans require multiple imaging sessions as the scanner cannot differentiate signals from multiple radiopharmaceuticals. In contrast, hyperpolarized (HP) ^{13}C MR has the unique capability of simultaneous multi-probe imaging: MR spectroscopic imaging can distinguish the signal of ^{13}C-labeled metabolic products by their unique chemical shifts, allowing real-time assessment of multiple metabolic fluxes and physiologic processes. For instance, ^{13}C-labeled pyruvate and urea can be co-polarized and co-administered in a single imaging session (**Figure 4.1a**) [142], and have been used extensively in preclinical studies [160, 161, 24, 134, 135, 77, 162]. Two HP ^{13}C pyruvate isotopomers, [1-^{13}C]pyruvate and [2-^{13}C]pyruvate, are currently used in clinical trials to image tumor metabolism for improved diagnosis and therapeutic evaluation [82, 13], setting the stage for the clinical translation of other HP imaging probes.

In this work, we aim to translate a dual-probe HP imaging technique using [1-^{13}C]pyruvate and [^{13}C, ^{15}N$_2$]urea for simultaneous metabolic and perfusion imaging (**Figure 4.1a**). Pyruvate is a critical intermediate in cellular energy metabolism, positioned at the intersection of several metabolic pathways. The conversion rates from pyruvate to lactate, alanine, CO_2/bicarbonate, and other Krebs's cycle intermediates reflect the expression and activity of relevant transporters and enzymes. Unlike HP ^{13}C pyruvate, HP ^{13}C urea is a metabolically inactive, extracellular probe; its MR signal is not affected by metabolic conversions but reflects blood flow, tissue perfusion, and volume of distribution [163, 160, 24, 77]. The synergy between HP ^{13}C pyruvate and urea MR is evident, as metabolism and perfusion often have opposite changes in disease progression and ther-

apeutic response, such as enhanced metabolism but defective perfusion in high-grade compared to low-grade tumors [24, 134, 158, 60], and decreased metabolism but increased perfusion in therapeutic responders compared to non-responders [77, 57]. The combined HP ^{13}C pyruvate and urea MR could also evaluate tumor hypoxia, a critical biological modulator of cancer progression and treatment response [24, 60, 164]. Moreover, HP ^{13}C urea could potentially improve the analysis of HP ^{13}C pyruvate metabolism kinetics by providing independent assessments on bolus arrival and vascular input. Additionally, [^{13}C, ^{15}N$_2$]urea has the advantage of longer T_1 at low field (mitigating polarization loss during sample transfer) and long T_2 (allowing higher *in vivo* signal) compared to [^{13}C]urea [165]. Taken together, the preclinical evidence provided a strong rationale for the clinical investigation of simultaneous metabolic and perfusion MR with HP [1-^{13}C]pyruvate and [^{13}C, ^{15}N$_2$]urea.

Herein, we report the technical development and translational studies towards dual-probe HP MR human imaging. First, we developed a co-polarization system for ^{13}C pyruvate and urea compatible with the clinical polarizer. We then systematically characterized the probe performance, identified and quantified the impurities in the injection product, and developed standard operating procedures (SOP) for routine on-site production of sterile co-polarized probes. Finally, we performed toxicology and preclinical imaging feasibility studies for clinical translation.

4.2 Methods and Materials

Co-polarization system for clinical studies. In preclinical studies, ^{13}C urea powder is dissolved in an excipient such as glycerol that provides glass-forming ability, which ensures the proximity between ^{13}C nuclei and electrons at DNP conditions. Next, neat pyruvic acid (PA) and urea/glycerol solution, each mixed with an electron paramagnetic agent (EPA), such as the trityl radical (AH111501 sodium), are sequentially frozen in the cryovial with minimal or no contact with each other [142]. This approach requires delicate manual manipulation of the cryovial and loading samples in frozen state into the polarizer, making it unsuitable for routine on-site production for clinical use. Additionally, glass-forming excipients are often exogenous compounds with high osmolality, which are undesirable for human injection.

Based on these considerations, the co-polarization system was re-designed to eliminate glass-
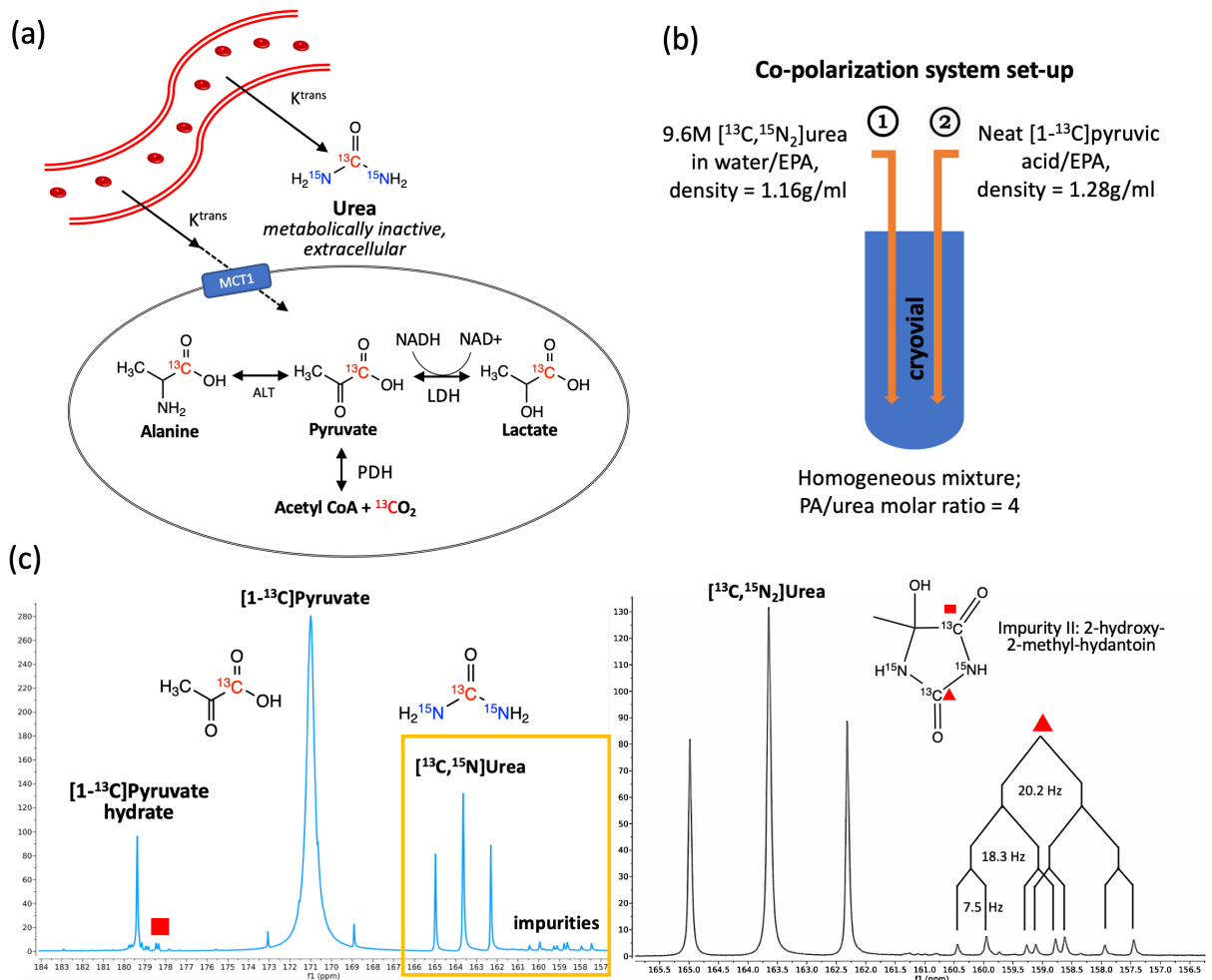
Figure 4.1: (a) Imaging mechanism: hyperpolarized ^{13}C pyruvate and urea are intravenously administered in a single bolus, then leave the vasculature and enter the extracellular space. Pyruvate can enter the cell (at a slower rate compared to vascular delivery) and be metabolized into lactate, alanine, or CO_2/bicarbonate, evaluating multiple metabolic fluxes. In contrast, urea is predominately extracellular and metabolically inactive, serving as a perfusion sensing probe. (K^{trans}, vascular transfer constant; MCT, monocarboxylate transporter; LDH, lactate dehydrogenase; ALT, alanine transaminase; PDH, pyruvate dehydrogenase). (b) Co-polarization system set up: urea/water/EPA mixture (lower density) is loaded into cryovial first, then pyruvic acid (PA)/EPA mixture is added (higher density), resulting in a homogeneous mixture of PA and urea with a molar ratio of 4:1. (c) Representative ^{13}C NMR spectra of hyperpolarized [1-^{13}C]pyruvate and [^{13}C, ^{15}N$_2$]urea. The right spectrum zooms in the boxed region of the left spectrum, showing urea and Impurity II with corresponding coupling constants (J_{CN} = 20.2 Hz, J_{CN} = 18.3 Hz, J_{CC} = 7.5 Hz).

forming excipients and sequential freezing of the cryovial (**Figure 4.1b**). To prepare the imaging probes for DNP, [^{13}C, ^{15}N$_2$]urea(GMP grade) was first dissolved in water (approximately 1:1 weight ratio) to generate a 9.6 M urea solution, then mixed with AH111501 (12.5 mM) before being loaded into the cryovial. Next, neat [1-^{13}C]PA (GMP grade) and AH111501 (12.5 mM) mixture was loaded on top of urea solution. PA can penetrate the urea layer due to its higher density (1.28 g/mL) than urea solution (1.16 g/mL), resulting in a homogeneous mixture consisting of approximately 10M [1-^{13}C]PA, 2.5 M [^{13}C, ^{15}N$_2$]urea, and 12.5 mM AH111501 in the cryovial.

Differential Scanning Calorimetry (DSC). Glass forming ability of the combined PA/urea imaging probe was characterized by DSC (TA instrument, New Castle, DE). Neat PA and PA/urea mixture with a wide range of PA/urea concentration ratios (from 9.4:1 to 0.96:1) were studied, with a cycling temperature of -90 to 40 °C. Detailed parameters are reported in Supplementary Information **Section 4.5.1**.

Hyperpolarization. Approximately 1.1 ml combined ^{13}C PA and urea (ISOTEC, Sigma-Aldrich, Miamisburg, OH) was polarized on a 5T SPINlab™ system (GE Healthcare, Waukesha, WI) with a high magnetic field (5 T), extreme-low temperature (0.8 K), and 139.97 GHz microwave irradiation for 3-4 hours, then rapidly dissolved in 41 ml super-heated (130 °C), pressurized sterile water and subsequently neutralized using equivalent NaOH and Tris.

Colorimetric quantification of urea concentration. Samples with unknown urea concentration were mixed at a 1:1 v/v ratio with a dye solution consisting of 1.2 M p-Toluenesulfonic acid and 10 mM 4-(Dimethylamino)cinnamaldehyde (DMAC) in a cuvette of 1 cm in length. Absorbance at 527 nm wavelength was measured using a spectrophotometer (DH-2000-BAL, Ocean Insights, Orlando, FL), and the urea concentration was derived by comparing the measured absorbance to a calibration curve previously acquired using the same experimental set up (**Figure S.4.3**).

Nuclear Magnetic Resonance (NMR) spectroscopy. Hyperpolarized ^{13}C NMR spectroscopy was acquired on a 1.4 T bench-top NMR system (Oxford Instruments, UK) with the following parameters: 5° flip angle, 8000 Hz spectral width, 0.125 Hz spectral resolution, 8.7 s temporal resolution for total 50 repetitions. After the HP acquisition, 10 % v/v D$_2$O and 1% v/v Gd-DTPA (Magnevist®, Bayer, Whippany, NJ) were added to the NMR tube to quantify the thermal equilibrium NMR signal (90° flip angle for 1000 averages). Longitudinal relaxation (T_1) time constants for [1-^{13}C]pyruvate and [^{13}C, ^{15}N$_2$]urea were estimated from dynamic HP signal

after corrections for RF depletions of the HP signal. Liquid-state polarization of the HP probe was estimated by comparing the first HP spectrum's signal to the thermal-equilibrium spectrum, then back-calculated to the time of dissolution using T_1 time constants estimated at 1.41 T. ^{13}C NMR spectroscopy of starting material and manual dissolution product was acquired at an 11.7 T system (Bruker Avance III) to corroborate with HP NMR studies. Detailed NMR methods are reported in Supplemental Information **Section 4.5.3**.

Liquid chromatography-mass spectrometry (LC-MS). Impurities in the co-polarized probes were analyzed using high-performance liquid chromatography (HPLC) coupled with quadrupole time-of-flight mass spectrometry (Q-TOF-MS) (**Figure S.4.11**). Two-µL samples were sent for analysis immediately after dissolution. A negative ionization mode was used. Impurity quantification (µg/ml) was obtained by spiking the sample with an internal reference standard (Impurity II) and referencing a calibration curve (**Figure S.4.12**).

Toxicology study. Four groups of male Sprague-Dawley rats (2-3 months old, 0.4-0.55 kg body weight) were intravenously injected with 2.5 ml over 10 s of the following solution: (I) saline control, n = 3; (II) HP co-polarized injection product (approximately 150 mM pyruvate, 35 mM urea), n = 10; (III) Impurity II (5-hydroxy-5-methyl-hydantoin; 40 mM in saline), n = 5; (IV) Impurity III (5-methyl-5-ureido-hydantoin; 20 mM in saline), n = 5. Given that the human injection dose used in HP pyruvate clinical studies is 0.43 ml/kg body weight, Group II (HP co-polarized group) received a greater than 10 times dose escalation, and Group III and IV (impurity groups) received a greater than 100 times dose escalation. Animals' vital signs, including heart rate, respiratory rate, and oxygen saturation, were recorded before, during, and 20 minutes after the intravenous injection using a pulse oximeter (MouseOx®; Starr Life Sciences Corp, Oakmont, PA). The animals were monitored for clinical signs of toxicity for two weeks after the injection, and their body weights were recorded during the monitoring period. Blood samples were collected before as well as 20 minutes and 2 weeks after the injection for complete blood counts (CBC) and liver-kidney function laboratory tests. The animals were sacrificed two weeks after injections for gross pathological examination.

In vivo **hyperpolarized ^{13}C MRI.** All animal experiments were performed according to the University of California, San Francisco Institutional Animal Care and Use Committee (IACUC) approved protocols. Adult Sprague-Dawley rats (n = 3) were imaged following HP co-polarized

76

injection on a 3 T clinical MR scanner (Discovery™ MR750; GE Healthcare, Milwaukee, WI). Adult rats were intravenously injected with 2.5 mL co-polarized [1-^{13}C]pyruvate and [^{13}C,^{15}N$_2$]urea produced using the SOP as described above. Then dynamic MR images of pyruvate, alanine, lactate, and urea were acquired with volumetric coverage of the rat's body. Pyruvate, lactate, and alanine images were acquired using a spiral GRE sequence as previously described [166], with the following design parameters: 80 Hz RF pulse passband, 25.17 ms pulse length, 22 ms readout duration, and 88 ms repetition time (TR). Urea images were acquired using a balanced steady state free precession (bSSFP) sequence and a non-spatially selective RF pulse with a 40 Hz passband and stopband and a 6 ms pulse length. The TR was designed to be 12.26 ms to minimize spectral banding artifacts perturbing other metabolites. The 3D stack-of-spiral readouts consist of 6 spiral readout interleaved per phase encoding step for 16 phase-encoding steps (slices), with a 4 ms readout duration in each step to mitigate off-resonance effects. The following acquisition parameters were used: flip angles of lactate, alanine, pyruvate, and urea were 30°, 30°, 8°, 50°; 2.6 × 2.6 × 21 mm spatial resolution; 4.2 s temporal resolution. ^{13}C dynamic MR acquisitions were automatically triggered after bolus arrival in the kidneys, using an autonomous scanning protocol, including real-time frequency and B$_1$ field calibration, implemented on the RTHawk platform (HeartVista, Los Altos, CA) as previously described [31].

4.3   Results

4.3.1   Imaging probe characterizations

Since stable glass formation is critical for dynamic nuclear polarization (DNP), we sought to characterize the glass-forming ability of the combined PA/urea probe using DSC. We found that PA/urea/water mixtures with various PA/urea ratios (2.2, 4, 5.8, and 9.4) can form a stable glass with glass transition temperatures (T$_g$) ranging from -70 to -80 °C. No crystallizations during repeated thaw-freeze cycles were observed (**Figure S.4.1**). The combined PA/urea probe exhibited similar glass transition behaviors to neat PA, the most commonly used HP imaging probe (**Figure S.4.1**).

We then characterized the polarization performance of the combined PA/urea probe on a 5 T SPINlab™ system (0.8 K). The combined PA/urea probe had a solid-state build-up constant of

6340 ± 1934 s (n = 20). After 3.5-4 hours of 139.87 GHz microwave irradiation, the co-polarization system produced liquid state polarization of $40.0 \pm 5.9\%$ for pyruvate, $39.1 \pm 7.3\%$ for urea (n = 21). A representative ^{13}C NMR spectrum of HP injection product acquired on a 1.4 T bench-top spectrometer is shown in **Figure 4.1c**.

4.3.2 Standard Operating Procedure (SOP) development

We developed and optimized an SOP for routine on-site production of sterile co-polarized probes using the hardware that are currently used in HP ^{13}C pyruvate clinical studies, following with Good Manufacturing Practice (GMP) outlined in the U.S. Code of Federal Regulation Title 21, Part 212. Briefly, after [1-^{13}C]PA and [^{13}C, ^{15}N$_2$]urea is combined in the cryovial, a purpose-built, disposable fluid path, which is also known as Pharmacy Kit (GE Healthcare, Milwaukee, WI), is assembled (**Figure 4.2**). The cryovial that contains combined PA/urea probe (referred to as "starting material") is loaded into a SPINlab™ polarizer. After 3.5-4 hours of microwave irradiation, the starting material is dissolved by superheated and pressurized Sterile Water for Injection (SWFI) in the dissolution syringe (Part A) by a computer-controlled process. The part A dissolution then pass through a size-exclusion filter that traps EPA, which precipitates in the presence of pyruvic acid. Next, the dissolution product is neutralized by NaOH and Tris in the receiver vessel (Part B), producing HP media at physiologic temperature and pH (referred to as "injection product"). Finally, the HP co-polarized injection product passes through a terminal sterility filter before being collected in the administering syringe. The materials used in the co-polarized probe formulation and fluid path assembly are reported in **Table 4.1**, and a flowchart of the production process is shown in **Figure 4.2b**. Neutralization media used in the receiver vessel (Part B) was designed to neutralize a wide range of pyruvic acid concentrations resulting from with the varying amount of combined PA/urea probe recovered from the cryovial. A bench-top titration experiment was performed to validate the pH buffer capacity of the neutralization media, which demonstrated the buffer system could neutralize a wide range of pyruvic acid concentrations (125-190 mM) (**Figure S.4.2**). The SOP was further validated by four consecutive successful Process Qualification trials (**Table S.4.1**), which reproducibly generated over 40 ml of injection product consisting of approximately 150 mM sodium [1-^{13}C]pyruvate and 35 mM [^{13}C,^{15}N$_2$]urea with physiological temperature and pH.
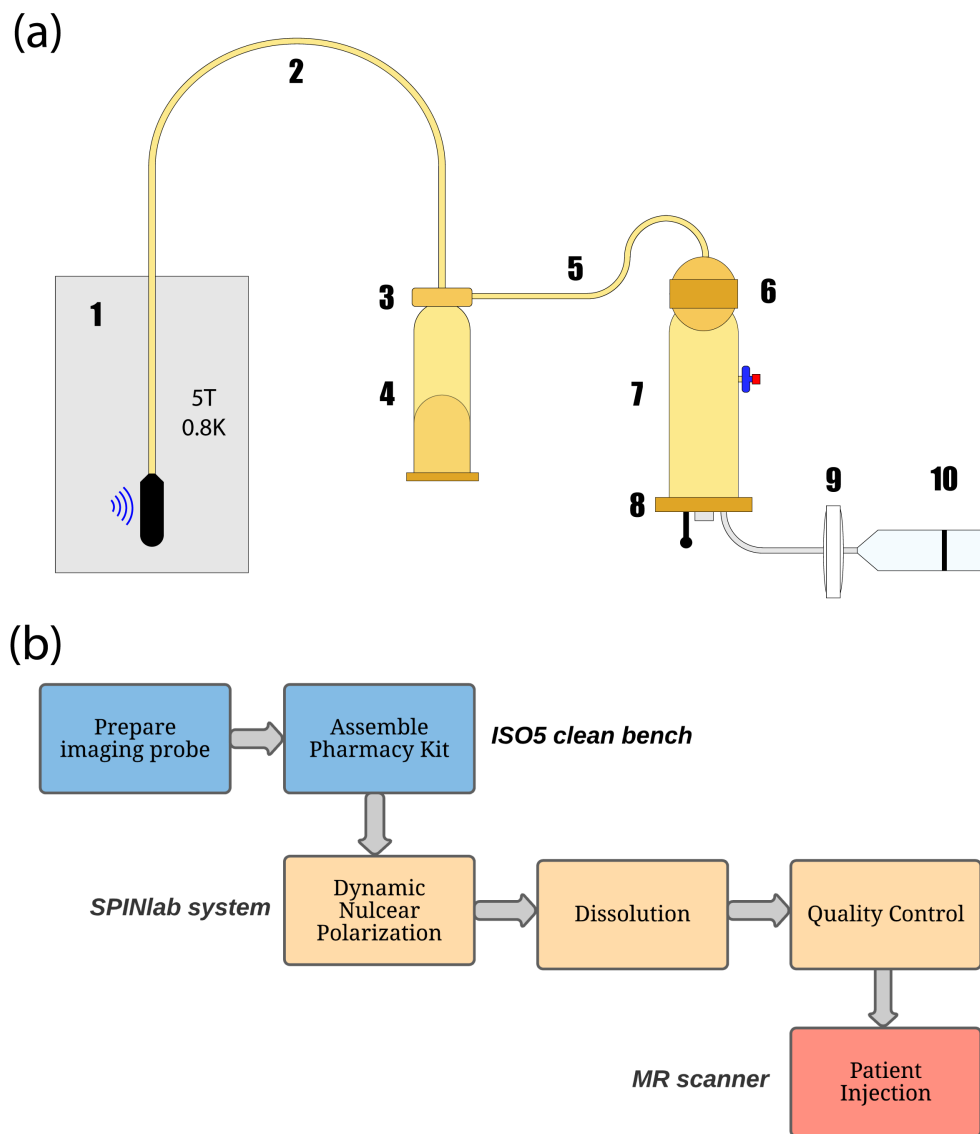
Figure 4.2: (a) Pharmacy Kit (fluid path) components: 1) cryovial in the SPINlab™ system with microwave irradiation; 2) dual-lumen dissolution tubing; 3) dissolution syringe valve; 4) dissolution syringe; 5) single-lumen transfer tubing; 6) electron paramagnetic agent (EPA) filter; 7) receiver vessel; 8) quality control (QC) plate with optical cuvette and NMR bulb; 9) sterility filter; 10) MedRad® syringe for patient administration. (b) Co-polarized probe production process flow chart.

Table 4.1: Pharmacy Kit (fluid path) composition for co-polarized [1-^{13}C]pyruvate and [^{13}C, ^{15}N$_2$]urea probes

Components	Chemical composition	Function
Cryovial	Neat [1-^{13}C]pyruvic acid* 1.098 g ($\pm$ 2%)	Metabolism-sensing probe
	9.6 M [^{13}C,^{15}N$_2$]urea in SWFI* 0.378 g ($\pm$ 2%)	Perfusion-sensing probe
	*Mixed with 12.5 mM trityl radical (AH111501) sodium salt	Electron paramagnetic agent
Dissolution syringe (Part A)	SWFI 41 g $\pm$ 0.05 g	Heated and pressurized to dissolve frozen contrast agent in the cryovial
Receiver vessel (Part B)	Neutralization media 13.50 $\pm$ 0.05g (consisting of 558 mM NaOH, 310 mM Tris, 351.4 mg/ml EDTA)	Neutralize pyruvic acid and pH buffer
	SWFI 19.35 $\pm$ 0.05g	Diluent

Abbreviation: SWFI, sterile water for injection.

4.3.3 Quality Control (QC) procedures

Immediately after dissolution, pyruvate concentration, residual EPA concentration, pH, temperature, and volume of HP co-polarized injection product were measured by the SPINlab™ QC system in an automated process and the analytical tests and the acceptable ranges are listed in **Table S.4.2**. The concentration of urea was indirectly estimated from pyruvate concentration based on the molar ratio of PA to urea in the formulation. A colorimetric method was developed to quantify urea concentration (**Figure S.4.3**) and found the indirect estimations agree with these post-dissolution quantifications (**Table S.4.1**). To ensure the injection product's sterility, the integrity of the terminal sterility filter was manually tested before releasing the injection product for administration. Endotoxin tests were also performed post-administration.

4.3.4 Impurity investigation

Multiple low-intensity impurity peaks neighboring pyruvate and urea peaks were observed on the ^{13}C NMR spectrum of co-polarized [1-^{13}C]pyruvate and [^{13}C, ^{15}N$_2$]urea (**Figure 4.1c**) but were not observed for individually polarized ^{13}C pyruvate or urea, suggesting that these impurities arose from the co-polarization process. To identify and quantify these impurities, three sets of ^{13}C NMR experiments were performed at 11.7T on the following samples: 1) raw materials ([^{13}C]urea, [^{13}C,^{15}N$_2$]urea, and [1-^{13}C]PA) for baseline structure elucidation and peak assignment (**Figure S.4.4**); 2) starting material for co-polarization (PA/urea mixture) for impurity identification and structure elucidation (**Figure S.4.4, S.4.5**); 3) neutralized [1-^{13}C]pyruvate and [^{13}C,^{15}N$_2$]urea injection product for impurity quantification. Three novel impurity (I, II, III) compounds were identified in the starting material and injection products based on their unique chemical shifts and J_{CC} and J_{CN} coupling constants (**Table S.4.3**); their presence were also confirmed by liquid chromatography-mass spectrometry (LC-MS). These impurities are likely to be the cross-reaction product of [1-^{13}C]pyruvic acid and [^{13}C,^{15}N$_2$]urea during the fluid path assembly process (**Figure 4.3**). Impurity II (5-hydroxy-5-methyl-hydantoin) was found to be the most prominent novel impurity compound in the injection product (1.71 ± 0.26% molar concentration by LC-MS, and 2% by NMR), while the percent molar concentration of Impurity I (2-hydroxy-2-ureido-propanoic acid) and Impurity III (5-methyl-5-ureido-hydantoin) were both estimated to be less than 0.5%.
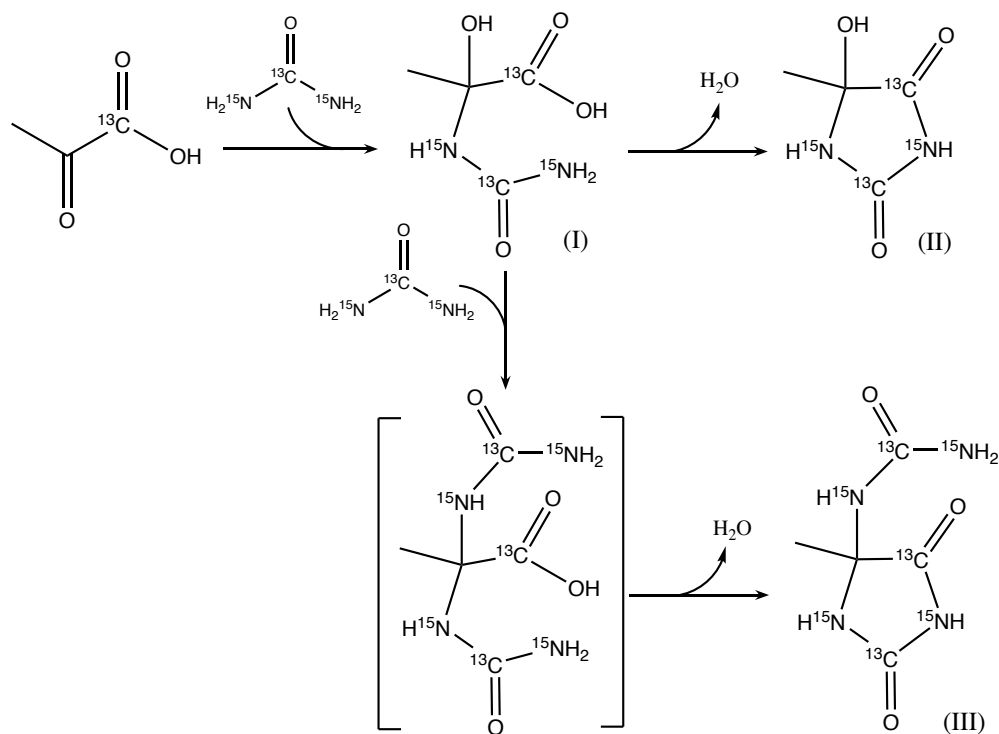
Figure 4.3: Impurity formation scheme in co-polarized [1-^{13}C]pyruvate and [^{13}C,^{15}N$_2$]urea. These reactions most likely occur in the cryovial at high-concentration conditions: the nucleophilic addition of urea (nitrogen) to pyruvic acid (C2 carbonyl carbon) yields Impurity I, an intermediate, which further undergoes intramolecular condensation between the carboxylate group and amide group, yielding Impurity II, a hydantoin. Impurity I can also undergo nucleophilic substitution with urea at C2 carbon before intramolecular condensation, yielding Impurity III, another hydantoin.

Further, only Impurity II was consistently observed on HP ^{13}C NMR spectra (**Figure 4.1c**) but not Impurity I and III, consistent with the finding that Impurity II is the predominant novel impurity in the dissolution product by NMR and LC-MS analyses. Detailed NMR impurity analyses are reported in Supplementary Information **Section 4.5.3**.

4.3.5 Toxicology study

We investigated the potential toxicities of the co-polarized injection products (the combination of pyruvate and urea) and the isolated novel impurity compounds. Four groups of Sprague-Dawley rats were injected with normal saline (n = 3), co-polarized injection product (n = 10) with a 10-fold dose escalation, or isolated Impurity II or III (n = 5 each) with a 100-fold dose escalation. All injections were well-tolerated, and no significant physiological effects were observed either acutely

or chronically for any group (**Table S.4.4, S.4.5, S.4.6**). No significant changes in body weight or mortalities were observed for any group during the 2-week monitoring period after the injection (**Table S.4.7**). Laboratory evaluations, including CBC (**Table S.4.8**) and liver-kidney function tests (**Table S.4.9**), also showed no significant acute or chronic deviations from the saline control group, the group baseline, or the reference range. No abnormalities of major organs were observed on gross pathological examination 2 weeks after the injection. Finally, no behavioral abnormalities were observed in the animals studied.

4.3.6   Imaging feasibility study

Although $[^{13}C,^{15}N_2]$urea offers the advantage of reduced HP signal loss during sample transfer, the AX_2 spin system of $[^{13}C,^{15}N_2]$urea ($J_{CN} = 20$Hz, **Figure 4.1c**) can cause significant off-resonance artifacts when long readout trajectories are used. Moreover, the *in vivo* spectral region of the HP co-polarization study is crowded with $[^{13}C]$bicarbonate (163 ppm), $[^{13}C,^{15}N_2]$urea (164 ppm), $[1-^{13}C]$pyruvate (171 ppm), $[1-^{13}C]$alanine (176 ppm), $[1-^{13}C]$pyruvate hydrate (181 ppm), and $[1-^{13}C]$lactate (183 ppm), making it challenging to perform dynamic, frequency-specific imaging with adequate spatial coverage and temporal resolution. In this study, we developed a 3D balanced steady-state free precession (bSSFP) sequence to image $[^{13}C,^{15}N_2]$urea MR, consisting of urea frequency-selective RF excitation pulses and interleaved stack-of-spiral readouts (**Figure 4.4a**) [166]. This acquisition method was designed to utilize HP signal efficiently, minimize RF perturbations to other metabolites, and mitigate off-resonance artifacts using repeated RF refocus pulses and a short readout duration (4 ms). The urea RF pulse excitation profile and resulting the magnetization responses of bSSFP sequence are shown in Supplementary Information **Figure S.4.13**. Pyruvate, lactate, and alanine were imaged using multi-slice spiral gradient echo (GRE) sequences as previously reported [166]. Simultaneous metabolic and perfusion imaging was achieved by alternatively applying multi-slice spiral GRE sequence for pyruvate and its metabolites and 3D bSSFP sequence for urea.

Compared to single-shot spiral GRE images of urea, bSSFP images showed superior image qualities with considerably reduced image blurring due to off-resonance artifacts, where the kidney cortex can be distinguished from the medulla (**Figure 4.4b,c**). In the images of sum metabolite signal of a kidney slice (**Figure 4.4c**), lactate signal predominates in the kidney, while pyruvate
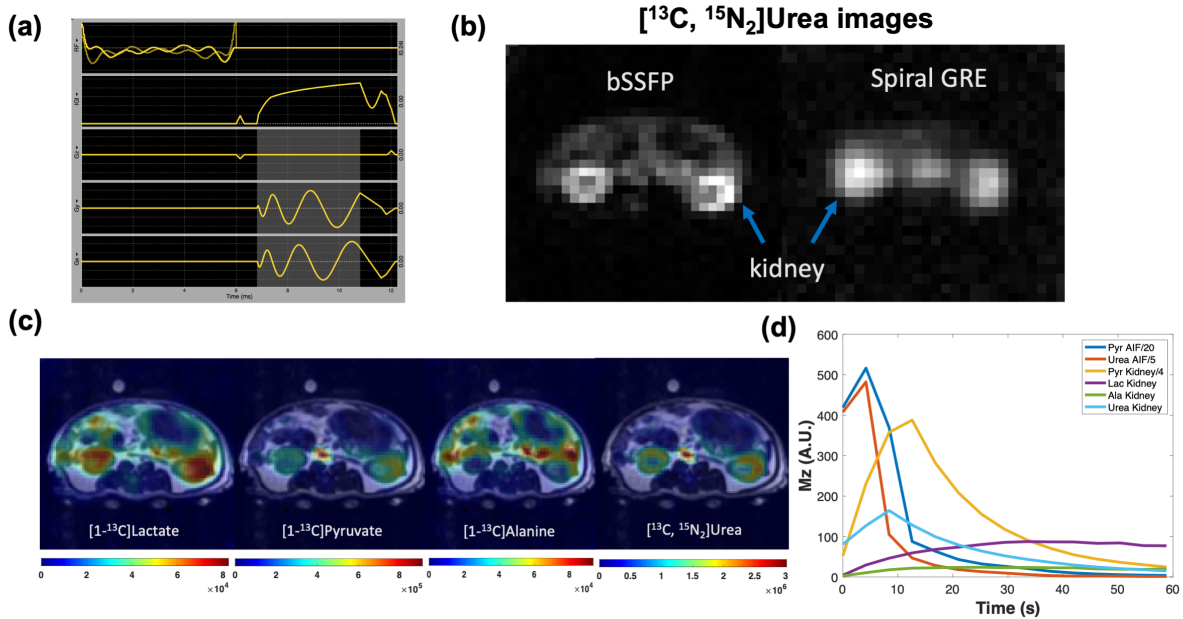
Figure 4.4: (a) A pulse sequence diagram of balanced steady-state free precession (bSSFP) sequence for hyperpolarized (HP) ^{13}C urea acquisition (highlighted area indicates readout duration). (b) bSSFP sequence produced superior image qualitity (signal-to-noise ratio, resolution, sharpness) compared to the single-shot spiral gradient echo (GRE) sequence. (c) Representative simultaneously acquired metabolism and perfusion images of an adult rat: sum HP signals of each metabolite were overlaid on T_2-weighted images; flip angles of lactate, alanine, pyruvate, and urea were 30°, 30°, 8°, 50°, with $2.5 \times 2.5 \times 21$mm spatial resolution and 4.2 s temporal resolution. (d) HP signal dynamics in the aorta and kidneys of an adult rat.

signal predominates in the vasculature (aorta and vena cava) and gastrointestinal tracts are highlighted on alanine images These findings are consistent with the imaging probe distribution and organ metabolic profiles. A plot of HP signal dynamics of pyruvate, lactate, alanine, and urea in the kidney and vasculature (aorta and vena cava) is shown in **Figure 4.4d**, where pyruvate and urea signals peak in about 5 s in the vasculature and in about 10 s in the kidney after the start of acquisition (with 5 s acquisition delay from the start of injection), whereas lactate and alanine signal gradually build up during the acquisition window.

4.4 Discussion

The interplay between metabolism and perfusion is involved in tumorigenesis, disease progression, and resistance to therapy, making metabolism and perfusion desirable cancer imaging markers.

However, combined metabolic and perfusion imaging often requires different imaging probes, acquisition techniques, or even modalities. HP ^{13}C MR is a promising molecular imaging technique to non-invasively study *in vivo* physiologic processes, with the unique capability of simultaneous multi-probe imaging. In this report, we present clinical translation efforts to incorporate a new perfusion-sensing probe, HP [^{13}C, ^{15}N$_2$]urea, into the existing HP ^{13}C pyruvate MR exams.

We first developed a co-polarization system for [1-^{13}C]PA and [^{13}C, ^{15}N$_2$]urea where PA provides glass-forming ability and eliminates the glass-forming excipient for urea. The short-range order in the glass, an amorphous state, ensures the uniform proximity of ^{13}C nuclei and unpaired electrons in the EPA, a requirement for dynamic nuclear polarization. PA, urea, and water can form an extensive hydrogen bonding network, preventing crystallization by raising the energy barrier for molecular reorganization and favoring glass formation [167, 168, 169]. Other attractive intermolecular forces such as dipole-dipole interactions among non-hydrogen bonding motifs in PA and urea also contribute to the glass forming ability [170]. Indeed, we observed that the combined PA/urea probe with a wide range of PA/urea ratios has a reliable glass-forming ability, with the glass transition temperature (T_g) similar to neat PA. Moreover, because the physical stability of glass below T_g is related to glass-forming ability [171, 172], the fact that the polarizer temperature (0.8 K) is well-below the T_g of the combined PA/urea probe (about 200 K) ensures the glass stability during DNP.

The 4 to 1 molar ratio of PA to urea in the formulation was chosen based on glass forming ability, target probe concentrations in the final injection product, and imaging feasibility. Quantification of metabolic fluxes requires sufficient *in vivo* SNR of downstream metabolic products of pyruvate (34). Since the starting material amount is limited by the cryovial volume, pyruvate content was prioritized for higher *in vivo* SNRs of pyruvate, lactate, and alanine. Further, since urea is dissolved in water, a higher urea content increases the water content of the formulation, increasing the likelihood of localized crystallization while reducing the glass forming ability. This formulation can generate nearly 40% liquid state ^{13}C nuclear polarization for both pyruvate and urea in 3.5–4 hours, comparable to the PA-alone formulation, and produce 40 mL of approximately 150 mM pyruvate and 35 mM urea in the final injection product. Although the final urea concentration is lower than previously reported in preclinical studies [161, 24, 134, 135, 77], the ^{15}N labeling renders [^{13}C, ^{15}N$_2$]urea with longer T_1 at low field (mitigating polarization loss during sample transfer) and

longer T_2 (higher *in vivo* signal) compared to [^{13}C]urea, compensating for the lower concentration.

We developed a SOP for routine on-site production to reproducibly generate sterile HP [1-^{13}C]pyruvate and [^{13}C, ^{15}N$_2$] urea injection products of acceptable probe concentration, pH, temperature, and volume with negligible residual EPA. There are several differences in the formulation and production processes for the combined PA/urea probe compared to PA-alone production. First, EPA concentration was reduced to 12.5 mM from 15 mM in PA-alone formulation because 15 mM EPA formulation was observed to have faster solid-state build-up but lower final polarization. The reduced EPA amount also facilitated its removal during the dissolution steps. Second, the amount of neutralization media in Part B receiver vessel was also reduced due to the reduced amount of PA in the cryovial. Third, the combined PA/urea probe was observed to be more viscous and have a higher heat capacity than neat PA due to extensive hydrogen bonding; thus, the SWFI amount in the Part A dissolution syringe (super-heated and pressurized) was increased to 41 g from 37.45 g to accommodate the increased heat capacity of the combined PA/urea probe compared to neat PA, which improved the sample recovery rate from the cryovial.

Pyruvic acid and urea can undergo slow cross-reactions under high concentration conditions [173], which motivated us to investigate impurities in the co-polarized probe. Integrating findings of hyperpolarized NMR, high resolution thermal equilibrium NMR, and LC-MS techniques, three novel impurity products were identified and quantified. The ^{13}C and ^{15}N labeling of the probes provided the sensitivity to identify impurities. J_{CC} and J_{CN} coupling patterns and constants are major clues to relate the unassigned resonance peaks on the HP NMR spectra (of the injection product acquired at 1.4 T) and the thermal equilibrium NMR spectra (of the starting material acquired at 11.7 T), and to infer their chemical structures. ^{13}C and ^{15}N labeled molecules have unique mass/charge ratio on LC-MS compared to their natural abundance counterparts, which confirmed the chemical structures identified by the NMR analysis. Moreover, the NMR and LC-MS techniques complemented each other's detection limit. Impurity I in the injection product was observed by NMR but not LC-MS, whereas Impurity III was observed by LC-MS but not NMR. Based on NMR and LC-MS, Impurity II was found to be the predominant impurity (1-2%) while Impurities I and III exist at lower concentrations ($< 0.5\%$). The quantitative impurity information further guided the design of the toxicology study.

Pyruvate and urea are endogenous molecules whose toxicity has been extensively studied. HP

^{13}C pyruvate injection (consisting of pyruvate, Tris, EDTA, and trace amount of AH111501) is currently used in clinical research studies, and its safety profile was previously reported in the Phase I clinical trial [69]. Intravenous urea has been administered clinically to treat glaucoma [174], cerebral edema [175, 176] and hyponatremia [177] at a dose of 1-1.5 g/kg body weight, about a thousand-fold higher than the HP co-polarized injection dose (0.8-1.3 mg/kg body weight of urea). Moreover, the parenteral urea drug product Ureaphil (Hospira) 40 g/vial was previously approved by the Food and Drug Administration (FDA). Therefore, we focused this toxicology study on investigating the potential toxicities of the HP co-polarized injection product and the isolated novel impurity compounds. Using injection products allows the characterization of biological effects of combined pyruvate and urea along with novel impurities. Two additional groups of rats were injected with Impurity II and III as isolated compounds to achieve further dose escalation. Impurity I was not studied as an isolated compound because of its negligible concentration and intermediate nature. No signs of toxicities associated with the combined pyruvate and urea probe were observed on any metrics studied, demonstrating its safety profile.

We further demonstrated the feasibility of simultaneous imaging [1-^{13}C]pyruvate, its downstream metabolites, and [^{13}C, ^{15}N$_2$]urea on a clinical MR scanner with adequate spatial coverage and temporal resolution. The AX$_2$ spin system of [^{13}C, ^{15}N$_2$]urea (1:2:1 peak ratio) modulates the urea signal, causing off-resonance artifacts. Moreover, at 25 ms after the start of spin system dephasing, spins of two side peaks are completely out of phase with spins of the central peak, creating a null signal in k-space (J_{CN} 20 Hz $\times$ 25 ms = 0.5 cycle/180°). In previous studies, bSSFP sequence with repeated RF refocus pulses and short readout durations to mitigate J_{CN} dephasing have been used to image [^{13}C, ^{15}N$_2$]urea [165, 178, 179]. However, in those studies there were no [1-^{13}C]pyruvate nor its downstream metabolites that could interfere with urea imaging. Moreover, those studies used cartesian readout trajectories with a long scan time, which is not feasible for 3D dynamic imaging. Based on these considerations, we developed a urea frequency-specific bSSFP sequence with a stack-of-spiral readout trajectory and short readout duration (4 ms) to mitigate off-resonance artifacts and avoid null signal points. Additionally, the bSSFP sequence offers a 2-3 fold SNR advantage compared to the spiral GRE sequence [166], and can further take advantage of the long *in vivo* T_2 (about 10 s) of [^{13}C, ^{15}N$_2$]urea by its efficient use of transverse magnetizations [165]. Pyruvate, alanine, and lactate images were sequentially acquired with a single-band spectral-

spatial RF excitation and a single-shot spiral readout. Two sequences, bSSFP for urea and spiral GRE for pyruvate and its metabolic products, were alternately applied to achieve simultaneous metabolic and perfusion imaging using commercially available software.

Our imaging approach has several limitations. First, the urea bSSFP sequence requires stringent RF pulse sequence design. The TR needs to be chosen carefully to avoid spectral banding artifact overlapping with non-urea metabolites. The bSSFP acquisition is also sensitive to B_0 inhomogeneity, which could cause the resonance frequencies of metabolites of interest inadvertently overlapping with the spectral banding artifact. Moreover, the urea RF pulse is not spatially selective because the long spectral-spatial RF pulse length is not compatible with the short TR of the bSSFP sequence. The non-spatial-selective RF pulse enforces a 3D acquisition, sensitive to flow effects. Second, the ^{13}C urea RF pulse has a passband and stopband of 40 Hz, leading to signal contamination from ^{13}C bicarbonate (80 Hz apart from urea at 3T). This urea bSSFP sequence might be acceptable for initial cancer imaging studies, where mitochondrial activities and bicarbonate signal are low, but needs to be further modified to image the brain, heart, and other organs where bicarbonate signals are not negligible. Third, although readout time is considerably reduced using stack-of-spiral readout trajectory, off-resonance imaging artifacts are not eliminated. Off-resonance corrections can be applied at the image reconstruction stage to improve image quality and metabolic quantification accuracy [180]. Finally, using two imaging sequences in a single imaging session requires specialized software and could complicate data analysis. A multi-echo acquisition approach (Iterative Decomposition of Echoes of Asymmetrical Length, IDEAL) that uses prior knowledge of chemical shifts and relative peak ratios of [^{13}C, ^{15}N$_2$]urea can achieve simultaneously image all metabolite using one acquisition sequence, but the long acquisition time is its main limitation [181].

Non-invasive assessments of *in vivo* metabolism and physiology afforded by HP ^{13}C MR can potentially facilitate initial diagnosis, treatment planning, and therapeutic evaluation for patients with cancer, providing an invaluable tool for precision medicine. The reported imaging technique leverages the unique capability of HP MR for multi-probe imaging to achieve a simultaneous assessment of glycolytic metabolism and perfusion, thereby providing a multimeric evaluation of tumor biology for patients with cancer in a single imaging session. To this end, we developed a formulation and an SOP that can reproducibly generate sterile co-polarized HP ^{13}C pyruvate and urea

solutions for human injection, as well as a novel imaging approach for simultaneous metabolic and perfusion imaging. In an upcoming clinical trial, the reported imaging technique will be used to image prostate cancer before surgery, with post-surgery imaging-biology correlation. This work also marks the clinical translation of the first HP MR probe after ^{13}C pyruvate.

4.5   Supplementary Information

4.5.1   Differential Scanning Calorimetry (DSC) Methods and Results.

A TA instrument Q2000 DSC (New Castle, DE) was used. The sample was loaded at room temperature, then heated to 40 °C and remained isothermal at 40 °C for 30 minutes. The system is then cooled to -90 °C and remained isothermal at -90 °C for 5 minutes, before heating to 40 °C again and remaining isothermal at 40 °C for 30 minutes to ensure complete sample melting. The above process was repeated twice for each sample. For all heating and cooling steps, a ramp rate of 5°C/min was used. The heat flow (W/g) was recorded during the above thermal transitions (**Figure S.4.1**), which demonstrated that pyruvic acid (PA) and urea mixture has good glass formation ability, with similar glass transition temperature (T_g) to near PA and no crystallization observed during the thermal cycle from 40 °C to -90 °C.
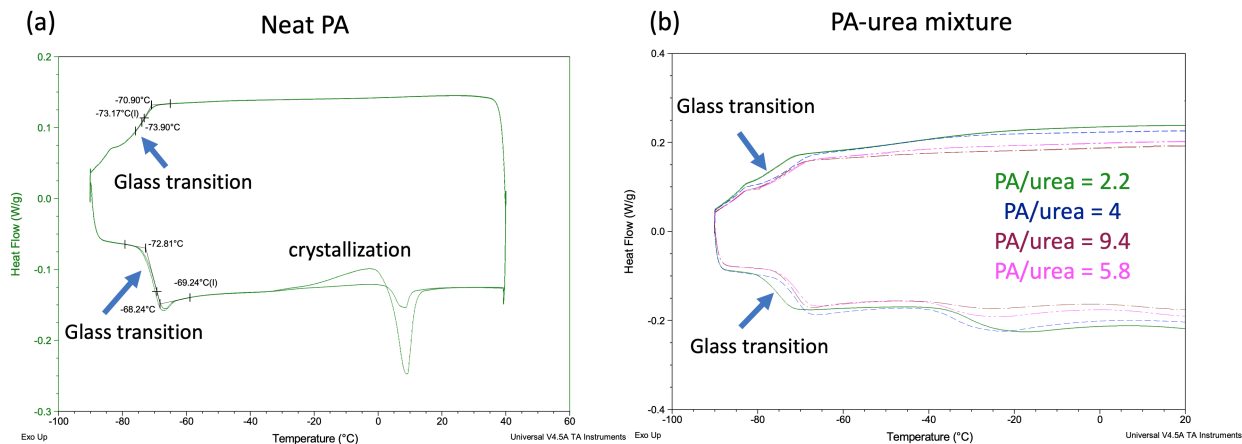
Figure S.4.1: Heat flow graph from Differential Scanning Calorimetry (DSC) studies. (a) Neat pyruvic acid (PA) showed glass transition from -70.9 °C to 73.9 °C and from -72.8 °C to -68.2 °C, and crystallization when heated above 0 °C. (b) PA and urea mixture with a wide range of PA/urea ratios showed similar glass formation around -70°C and no crystallization during the thermal cycle.

4.5.2 Standard Operation Procedure (SOP) Development and Validation

A set of experiments were performed to optimize and validate the procedures to produce sterile co-polairzed [1-^{13}C]pyruvate and [^{13}C, ^{15}N$_2$]urea injection product.
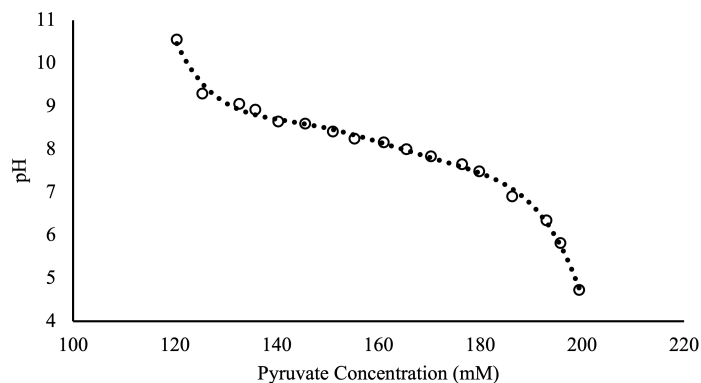
Figure S.4.2: Validation of buffer capacity in a titration experiment: the buffer system can neutralize a wide range of pyruvic acid concentration, an experimental variability depending on sample recovery rate.
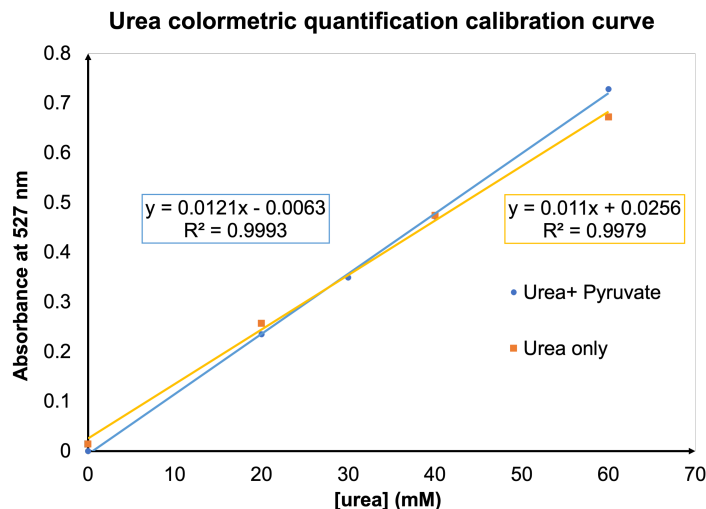
Figure S.4.3: The linear calibration curve for urea concentration quantification using optical absorbance methods. Urea reacts with 4-(Dimethylamino)cinnamaldehyde (DMAC) at the presence of p-Toluenesulfonic acid and forms a compound with unique absorbance at 525-529 nm. The presence of pyruvate (4:1 pyruvate to urea ratio) has minimal perturbation to urea concentration quantification between 20 to 40 mM (two lines nearly overlap), the target range of urea concentration in the co-polarized injection product.

Table S.4.1: Process Qualification (PQ) trials for co-polarized [1-^{13}C]pyruvate and [^{13}C, ^{15}N$_2$]urea production

Trial	Pyruvate QC (mM)	Urea indirect QC (mM)	Urea valida-tion (mM)	pH	EPA (μM)	Temp (°C)	Volume (ml)	Pyruvate polariza-tion	Urea polariza-tion	Sterility test
1	165	35	33.7	8.05	0.4	34.7	> 40	34.7 %	35.9 %	pass
2	151	34	34.3	8.17	0.7	34.4	> 40	36.6%	38.0%	pass
3	139	32	33.7	8.29	0.9	34	> 40	47.3%	47.9%	pass
4	166	37	43.0	7.7	1.5	37.5	> 40	40.9%	39.1%	pass

92

Process Qualification (PQ) trials to validate the Standard Operating Procedure (SOP) for routine on-site imaging probe production. The SPINlab™ quality control (QC) system reports pyruvate concentration, pH, electron paramagnetic agent (EPA) concentration, temperature, and volume. Ratiometric (indirect QC) quantification of urea was performed and found to be in agreement with measurements by photospectrometric method (validation). Percentage polarizations for pyruvate and urea were measured by ^{13}C NMR spectroscopy on a 1.4 T bench-top system. Sterility was assessed by manual integrity tests of the terminal sterility filter and endotoxin tests. All QC metrics for four trials met the pre-defined release criteria.

Table S.4.2: Quality Control (QC) tests for hyperpolarized [1-^{13}C]pyruvate and [^{13}C,^{15}N$_2$]urea injection product

Test	Analytical method	Target range
Pyruvate concentration	UV absorbance	125–195 mM
Residual trityl radical (AH 111501) concentration	Visible absorbance	5 µM
pH	Visible absorbance of ratiometric indicators	5.0–9.0
Drug product temperature*	IR pyrometry	25.0–40.0 °C
Drug product volume	Capacitive sensing	> 38 ml
Filter Integrity	Bubble point test	Manufacturer specification

*Specification to temperature is at the time of analysis.
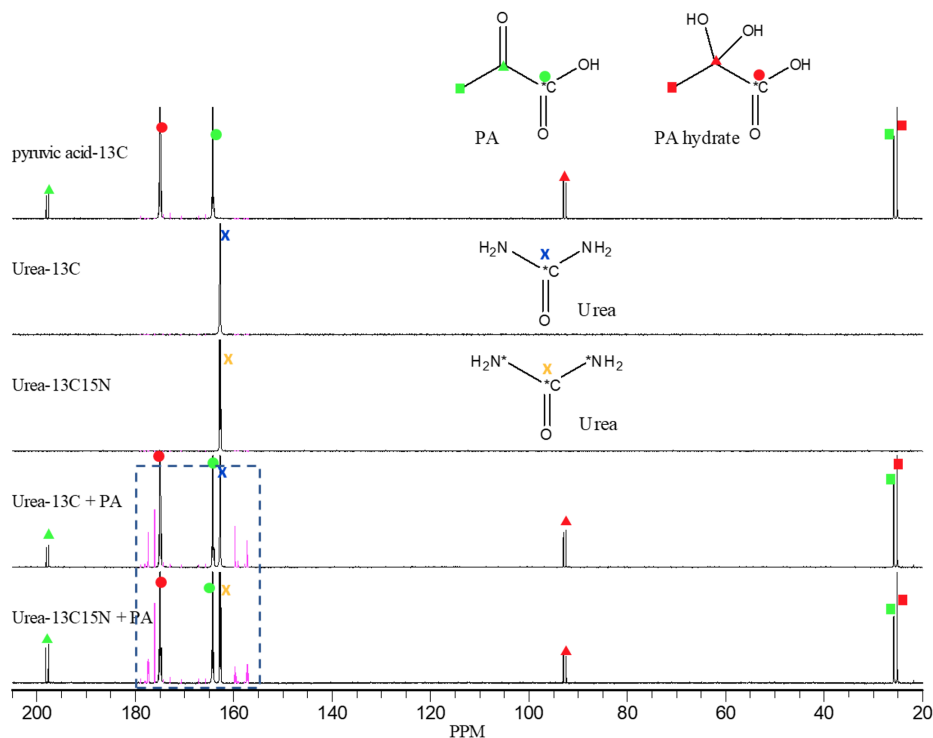
Figure S.4.4: ^{13}C NMR spectra of raw material and starting material of co-polarization of ^{13}C labeled pyruvic acid (PA) and urea. Peak assignments for PA and PA hydrate were confirmed.

4.5.3 NMR impurity analysis

Three sets of ^{13}C NMR experiments were performed on 11.7T/500MHz systems (Bruker Avance III or Varian Inova) to identify and quantify novel impurities in the co-polarized [1-^{13}C]pyruvate and [^{13}C,^{15}N$_2$]urea injection product: 1) raw material ([^{13}C]urea, [^{13}C,^{15}N$_2$]urea, and [1-^{13}C]pyruvic acid) for baseline structure elucidation and peak assignment (**Figure S.4.4**) ; 2) starting material for co-polarization (cryovial condition) for impurity identification: neat [1-^{13}C]pyruvic acid mixed with [^{13}C]urea, or [^{13}C,^{15}N$_2$]urea, at 4:1 molar ratio for 30 minutes at room temperature, then diluted by D$_2$O (**Figure S.4.4, S.4.4**); 3) manual dissolution product (patient injection condition) for impurity quantification: neutralized [1-^{13}C]pyruvate and [^{13}C,^{15}N$_2$]urea solution. All experiments used D$_2$O solvent and 1% v/v Gd-DTPA (Magnevist®, Bayer, Whippany, NJ). Standard data acquisition parameters were used, including a 5s repetition time with inverse gated 1H-^{13}C decoupling.
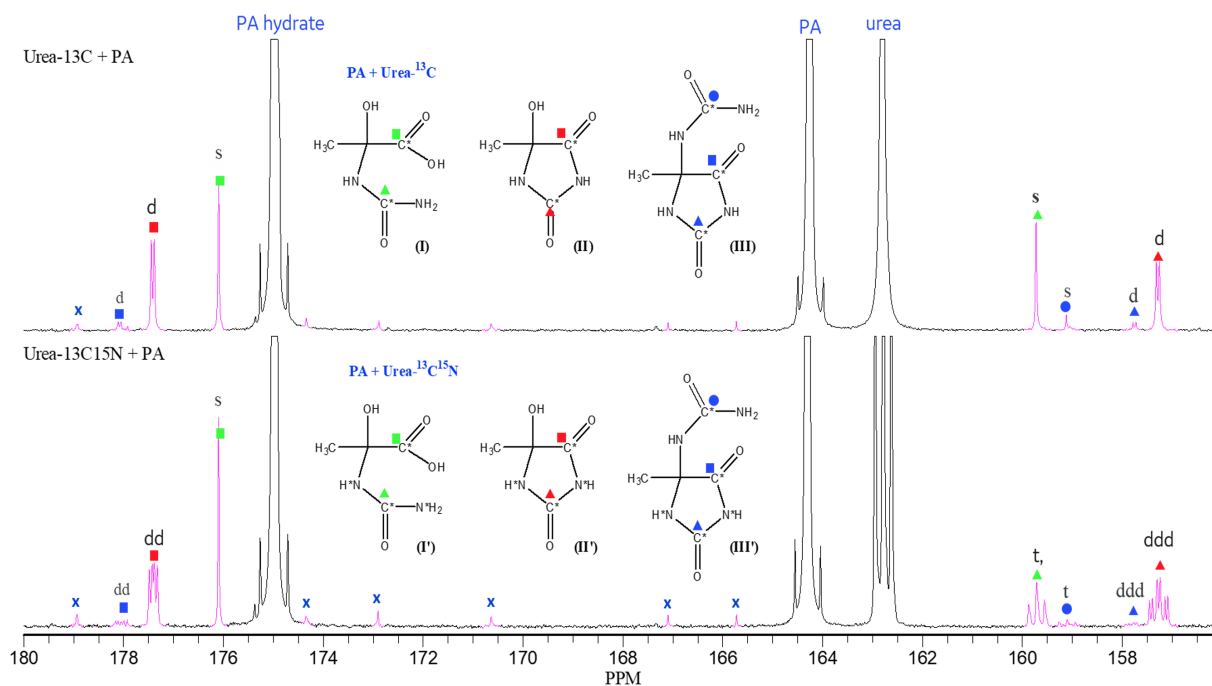
Figure S.4.5: ^{13}C NMR spectra of $[1\text{-}^{13}C]$pyruvic acid (PA) mixed with $[^{13}C]$urea and $[^{13}C, ^{15}N_2]$urea, respectively (starting material, high concentration cryovial condition). Three novel impurities were shown with peak assignment. Small peaks denoted with "x" corresponds to impurities in PA as they are present in ^{13}C PA starting material.

Three novel impurity compounds (I, II, III) were identified, with their % molar concentrations in the starting material estimated to be 0.28 %, 1.1 %, and 0.22 %, respectively (**Figure S.4.5**). To further understand the impurity formation schemes, neat $[1\text{-}^{13}C]$PA and 10M $[^{13}C, ^{15}N_2]$urea solution were mixed at a 4:1 molar ratio, and dynamic ^{13}C NMR was acquired for 1 hour after the mixing. The spectra showed broad peaks, resulting from the high viscosity of the mixture and inefficient shimming due to the low D_2O concentration. To identify these peaks, a gradual dilution was performed on this concentrated PA-urea mixture, where 50–100 µL of the approximately 700 µL solution was gradually replaced with D_2O, and ^{13}C spectra were taken after each dilution as shown in **Figure S.4.6**. As the sample becomes diluted, chemical shift changed due to concentration, pH, and solvent changes. As shimming quality improved, PA and urea peaks became distinguishable. Based on the relative chemical shifts, previously unassigned peaks at 158 ppm and 173 ppm were assigned to Impurity I, and previously unassigned peaks at 155 ppm and 174 ppm were assigned to Impurity II (**Figure S.4.7**.
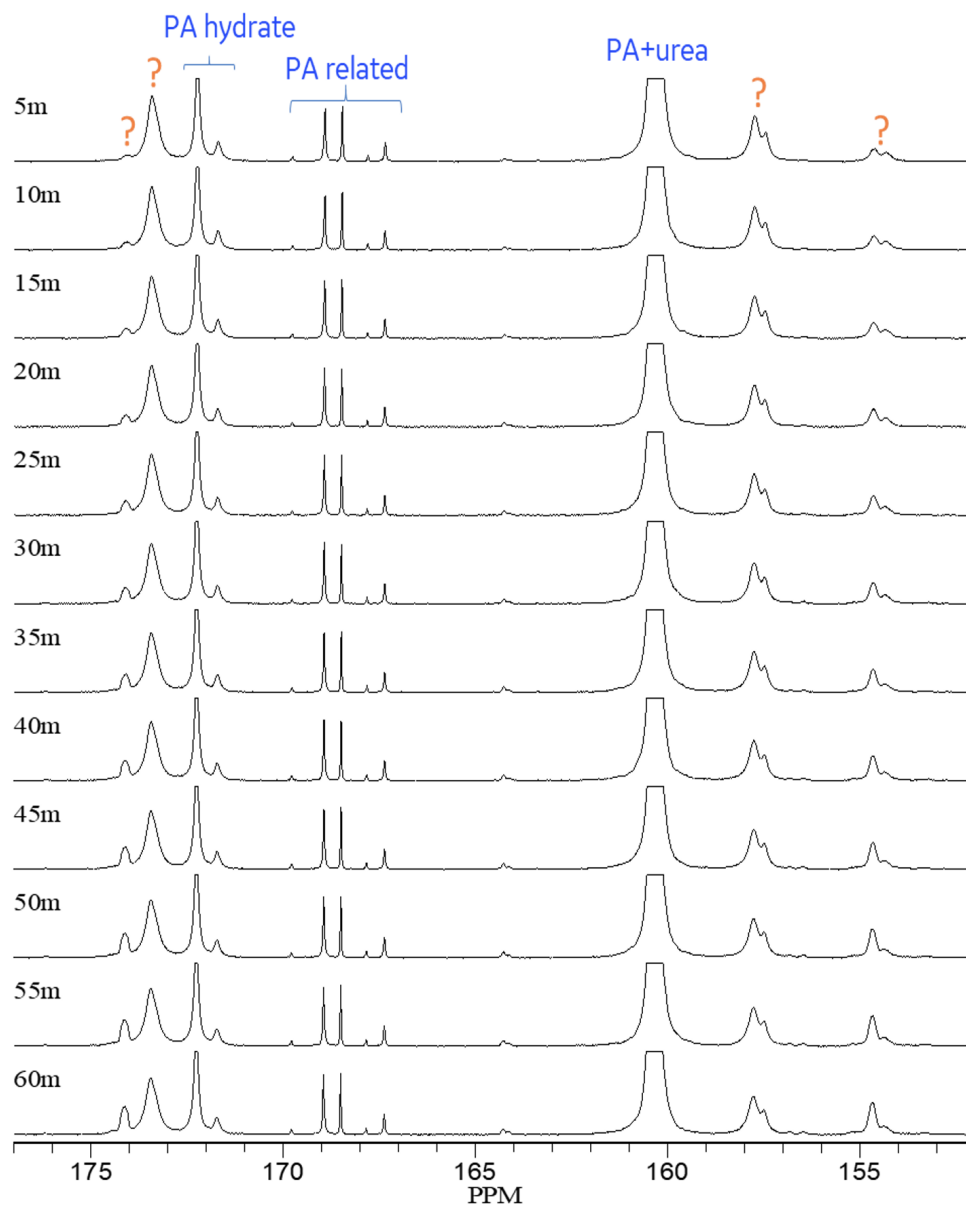
Figure S.4.6: Dynamic ^{13}C spectra of [1-^{13}C]pyruvic acid and [^{13}C,^{15}N$_2$]urea mixture at high concentration (before gradual dilution) to demonstrate impurity formation scheme. Peaks marked with "?" are to be assigned.
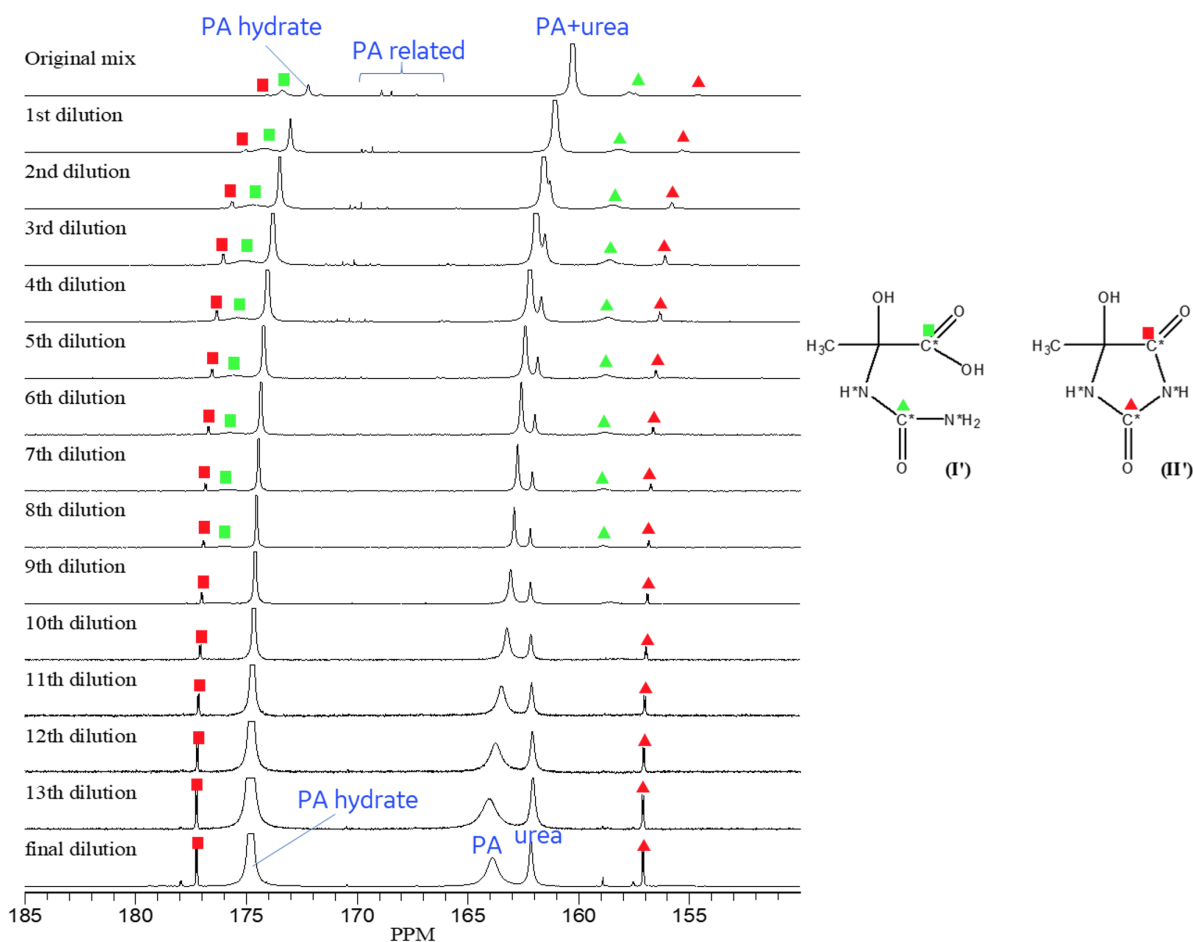
Figure S.4.7: ^{13}C spectra of [1-^{13}C]pyruvic acid (PA) and [^{13}C,^{15}N$_2$]urea concentrated mixture as being gradually diluted showed Impurity I peaks gradually disappear while Impurity II peaks gradually enhance, suggesting that Impurity I is readily converted to Impurity II at lower concentrations.

Taken together, the dynamic ^{13}C NMR of high concentration starting material and its gradual dilution suggest that Impurity I forms rapidly in the cryovial upon the mixing of pyruvic acid and urea, whereas Impurity II forms slowly. However, Impurity I is readily converted to Impurity II upon dissolution. Impurity III was not observed in this set of NMR experiments.

Further ^{13}C NMR study was performed on post-dissolution SPINlab™ Pharmacy Kit cryovial residual sample (**Figure S.4.8**) to elucidate and confirm the impurity structure ([1-^{13}C]pyruvic acid and [^{13}C,^{15}N$_2$]urea have longer cross-reaction time than bench-top studies, yielding higher impurity concentration). Notably, Impurity I was not observed in SPINlab™ Pharmacy Kit cryovial.

97
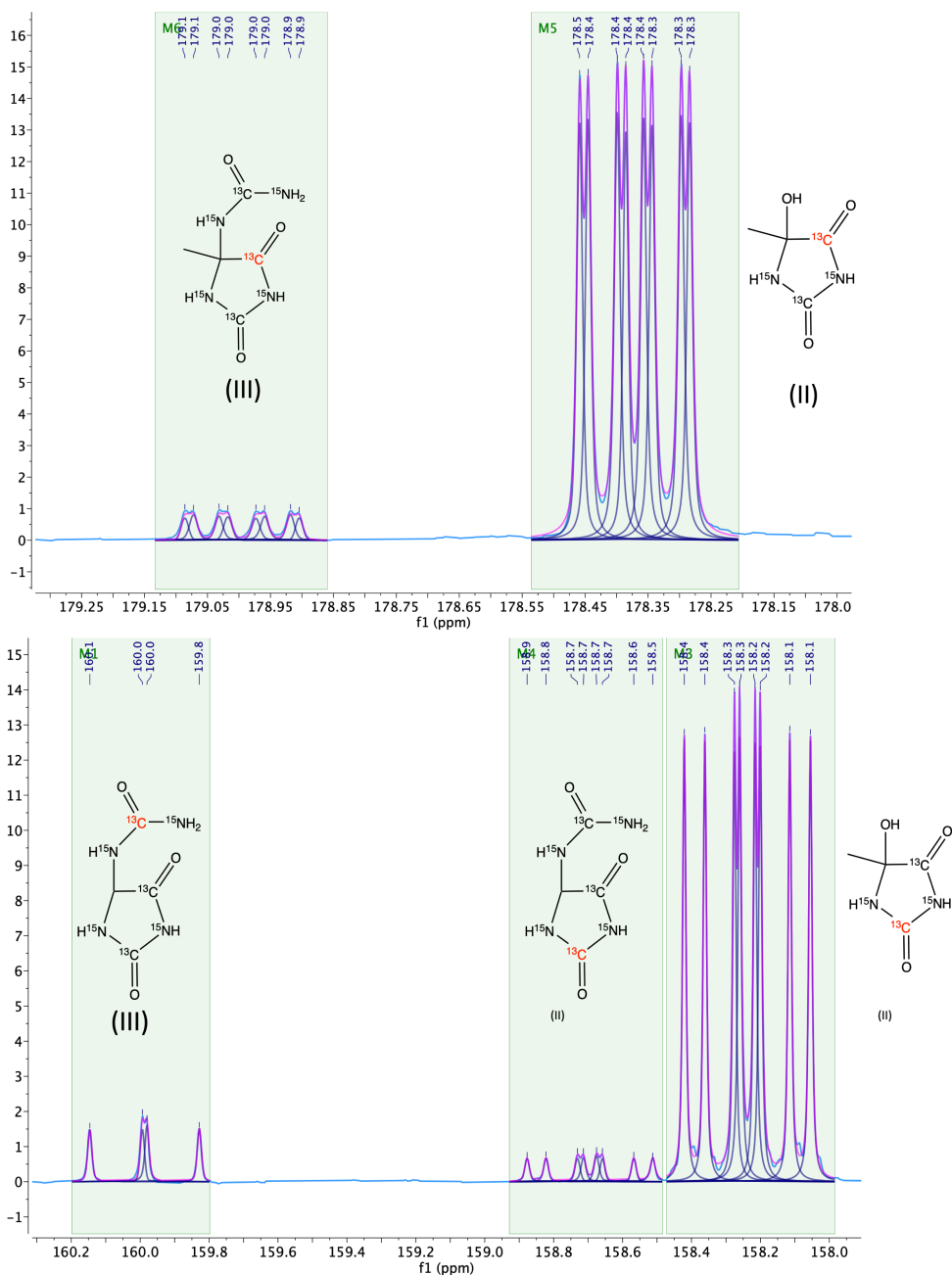
Figure S.4.8: ^{13}C NMR spectra of post-dissolution SPINlab™ Pharmacy Kit cryovial residual sample (high impurity content due to long reaction time and high concentration condition) shows the unique coupling content and the relative concentration of Impurity II and III. Impurity I was not observed.

Finally, impurity levels were quantified in the dissolution of $[1-^{13}C]$pyruvic acid and $[^{13}C,^{15}N_2]$urea. A bench-top manual dissolution was performed to replicate the Pharmacy Kit preparation process (including mixing, freezing, and thawing the starting material) and the SPINlab™ automated dissolution process (with rapid temperature and pH changes) (**Figure S.4.9**). The manual disso-
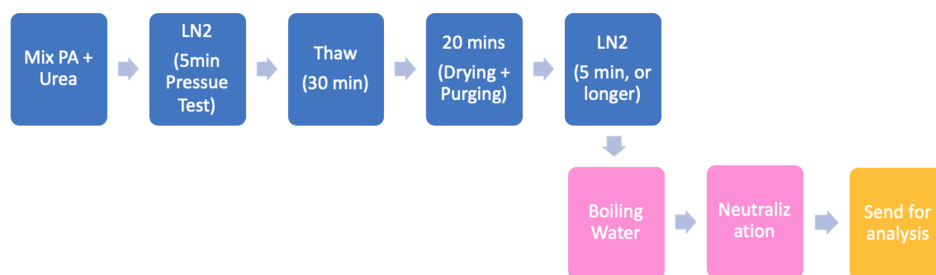
Figure S.4.9: Flowchart of the manual dissolution experiment to replicate SPINlab™ Pharmacy Kit preparation process (top row) and SPINlab™ polarizer dissolution process (bottom row). [1-^{13}C]pyruvic acid (PA) and [^{13}C, ^{15}N$_2$]urea are mixed at room temperature and then placed in liquid nitrogen (LN$_2$) for 5 minutes to replicate SPINlab™ Pharmacy Kit pressure test in LN2. The sample is subsequently thawed at room temperature for 50 minutes to replicate the thawing, drying, and purging of SPINlab™ Pharmacy Kit, followed by placing the sample into LN2 again to replicate loading the sample into the SPINlab™ polarizer. Then, the frozen sample is rapidly dissolved in boiling water (to replicate Part A dissolution syringe) and subsequently mixed with neutralization media consisting of NaOH, Tris, and EDTA (to replicated Part B receiver vessel). The dissolved and neutralized sample is sent for LC-MS and NMR analysis immediately.

lution was performed adjacent to analytic instruments to minimize the sample transfer time and to mimic the patient injection time scale. The target concentration for manual dissolution was 200 mM [1-^{13}C]pyruvic acid and 50 mM [^{13}C,^{15}N$_2$]urea. Quantitative ^{13}C NMR spectra were collected immediately after dissolution for 1 hour with 8 minutes scan time per spectra (**Figure S.4.10**).
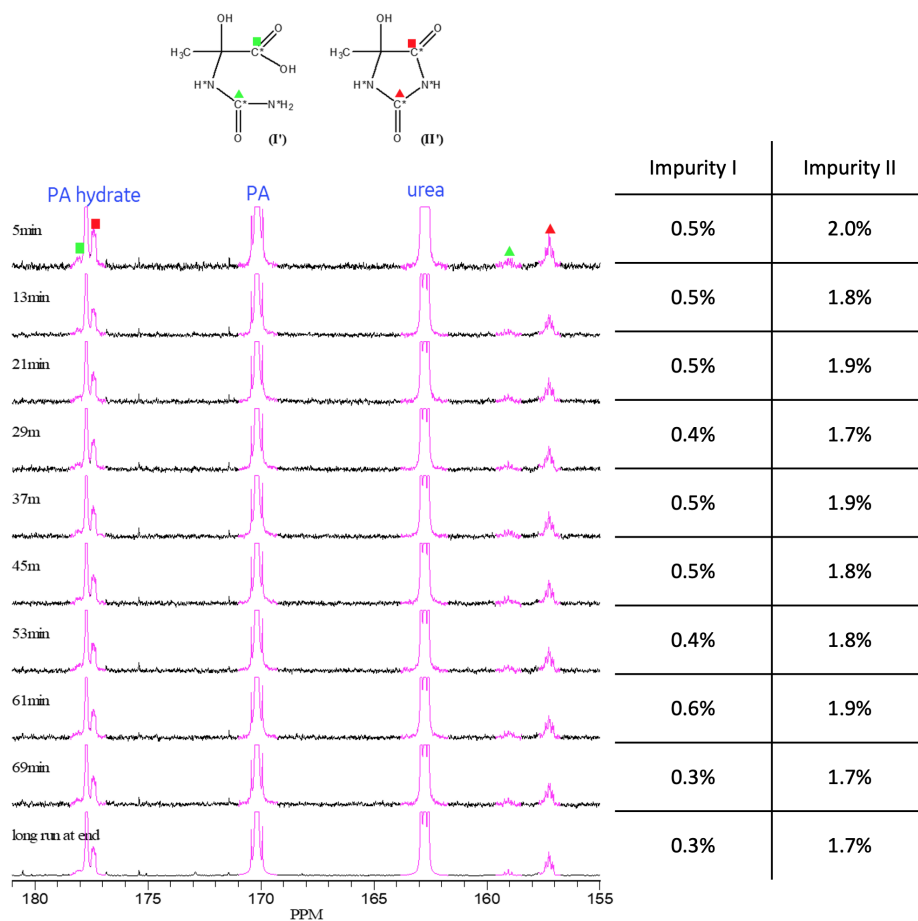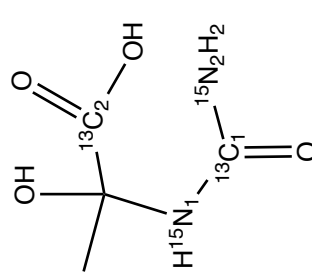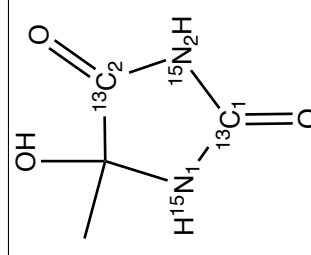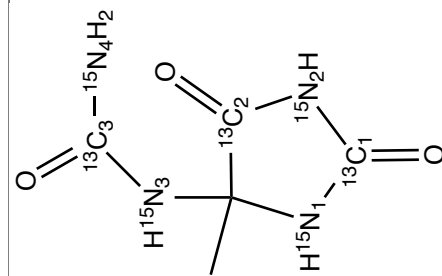
Figure S.4.10: Dynamic ^{13}C NMR spectra of manual dissolution product of [1-^{13}C]pyruvic acid and [^{13}C,^{15}N$_2$]urea with the corresponding % molar concentration of Impurity I and II. Impurity I and II concentrations are stable within one-hour post-dissolution.

Table S.4.3: Structure and characterization of novel impurities in co-polarized $[1\text{-}^{13}\text{C}]$pyruvate and $[^{13}\text{C},^{15}\text{N}_2]$urea

Assigned name	Chemical Structure	Chemical nomenclature	Molecular formula	Mole % in the injection product	J coupling constant
Impurity I		2-hydroxy-2-$[^{13}\text{C},^{15}\text{N}_2]$ureido-$[1\text{-}^{13}\text{C}]$ propanoic acid	$\text{C}_2^{13}\text{C}_2\text{H}_8^{15}\text{N}_2\text{O}_4$	0.5% by NMR; not detected by LCMS	$J_{\text{CC}} = 0.8$ Hz $J_{\text{C1N1}} = 19.6$ Hz $J_{\text{C1N2}} = 20$ Hz
Impurity II		5-hydroxy-5-methyl-$[2,4\text{-}^{13}\text{C}, 1,3\text{-15N}]$hydantoin	$\text{C}_2^{13}\text{C}_2\text{H}_6^{15}\text{N}_2\text{O}_3$	$1.71 \pm 0.26\%$ by LCMS; 2% by NMR	$J_{\text{CC}} = 7.5$ Hz $J_{\text{C1N1}} = 18.3$ Hz $J_{\text{C1N2}} = 20.2$ Hz $J_{\text{C2N1}} = 1.7$ Hz $J_{\text{C2N2}} = 12.7$ Hz
Impurity III		5-methyl-5-$[^{13}\text{C},^{15}\text{N}_2]$ureido-$[2,4\text{-}^{13}\text{C}, 1,3\text{-15N}]$hydantoin	$\text{C}_2^{13}\text{C}_3\text{H}_8^{15}\text{N}_4\text{O}_3$	$0.48 \pm 0.12\%$ by LCMS; not detected by NMR	$J_{\text{C1C2}} = 6.9$ Hz $J_{\text{C1N1}} = 18.3$ Hz $J_{\text{C1N2}} = 20.5$ Hz $J_{\text{C2N1}} = 1.7$ Hz $J_{\text{C2N2}} = 14.2$ Hz $J_{\text{C3N3}} = 20.9$ Hz $J_{\text{C3N4}} = 19.2$ Hz

4.5.4 LC-MS Methods
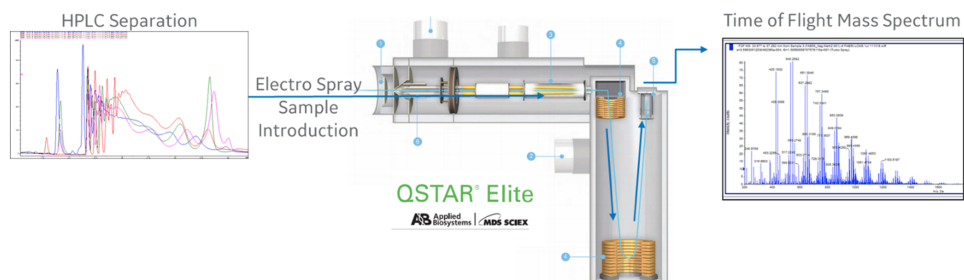
Figure S.4.11: Workflow of Liquid chromatography–mass spectrometry (LC-MS) study. Reversed-phase HPLC was run through Scherzo SS-C18 2 mm × 75 mm (Imtakt, Portland, OR) column at a flow rate of 0.2 ml/min using gradient elution with Solvent A (99.99% deionized water; 0.1% formic acid) and Solvent B (99.99% acetonitrile; 0.1% formic acid) under the following conditions: 0-5 minutes (100% Solvent A), 5-15 minutes (0-100% Solvent B), and 10 minutes equilibration to initial condition.
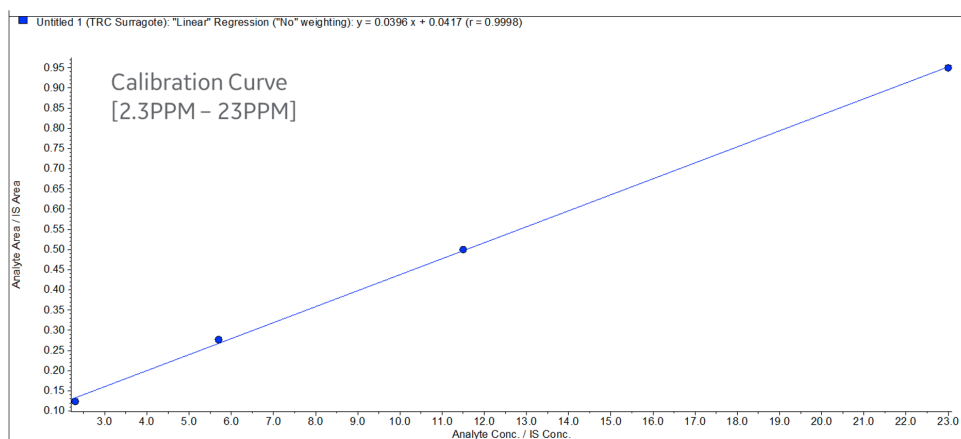
Figure S.4.12: LC-MS concentration quantification calibration curve of the internal reference standard (Impurity II, 5-hydroxy-5-methyl-hydantoin).

4.5.5 Toxicology study data

Four groups of male Sprague-Dawley rats (2-3 months old, 0.4-0.55 kg body weights) were intravenously injected with 2.5 ml of the following solution over 10 s: (I) saline control, n = 3; (II) HP co-polarized injection product (approximately 150 mM pyruvate, 35 mM urea), n = 10; (III) Impurity II (5-hydroxy-5-methyl-hydantoin; 40mM in saline), n = 5; (IV) Impurity III (5-methyl-5-ureido-hydantoin; 20mM in saline), n = 5. Abbreviations: Co-Pol, co-polarized [1-^{13}C]pyruvate and [^{13}C,^{15}N$_2$]urea.

Table S.4.4: Heart rate during injection (bpm)

Group	Injection	Baseline	5 min	10 min	15 min	20 min
I	Saline control	273 ± 16	279 ± 14	277 ± 10	280 ± 9	282 ± 21
II	Co-Pol	309 ± 43	314 ± 30	320 ± 30	324 ± 29	326 ± 28
III	Impurity II	316 ± 36	336 ± 28	334 ± 30	336 ± 31	337 ± 36
IV	Impurity III	337 ± 54	340 ± 31	348 ± 29	342 ± 36	344 ± 20

Table S.4.5: Breath rate during injection (bpm)

Group	Injection	Baseline	5 min	10 min	15 min	20 min
I	Saline control	39 ± 7	38 ± 5	39 ± 6	41 ± 8	41 ± 8
II	Co-Pol	42 ± 10	45 ± 9	46 ± 8	45 ± 8	47 ± 10
III	Impurity II	50 ± 11	54 ± 9	55 ± 13	54 ± 10	57 ± 8
IV	Impurity III	60 ± 5	55 ± 4	56 ± 13	54 ± 7	57 ± 9

Table S.4.6: Oxygen saturation rate during injection (%)

Group	Injection	Baseline	5 min	10 min	15 min	20 min
I	Saline control	99.5 ± 0.2	99.5 ± 0.1	99.5 ± 0.1	99.4 ± 0.1	99.5 ± 0.2
II	Co-Pol	98.9 ± 1.0	98.9 ± 0.9	98.9 ± 0.8	98.9 ± 0.9	99.0 ± 0.6
III	Impurity II	99.3 ± 0.7	99.5 ± 0.2	99.4 ± 0.4	99.3 ± 0.5	99.1 ± 0.5
IV	Impurity III	99.6 ± 0.2	99.6 ± 0.3	99.6 ± 0.3	99.6 ± 0.3	99.6 ± 0.1

Table S.4.7: Body weight 2 weeks post-injection (kg)

Group	Injection	SD1	SD3	SD5	SD8	SD10	SD13	SD15
I	Saline control	0.47	0.48	0.48	0.48	0.49	0.50	0.50
II	Co-Pol	0.47	0.47	0.47	0.48	0.48	0.48	0.49
III	Impurity II	0.47	0.47	0.47	0.47	0.48	0.48	0.48
IV	Impurity III	0.50	0.49	0.49	0.50	0.50	0.50	0.51

Abbreviation: SD, study day

Table S.4.8: Complete Blood Count (CBC) at baseline, 20 minutes, and 2 weeks post-injection

Test	Group I: Saline control (n = 3)			Group II: Co-Pol (n = 10)			Group III: Impurity II (n = 5)			Group IV: Impurity III (n = 5)			Reference range
	baseline	20 min	2-week	baseline	20-min	2-week	baseline	20-min	2-week	baseline	20-min	2-week	
WBC (1000 cells/uL)	12.7 ± 1.5	9.2 ± 3.1	11.7 ± 2	10.97 ± 1.35	9.3 ± 3.03	8.43 ± 2.13	9 ± 0.8	6.8 ± 1.8	6.9 ± 1.6	9.6 ± 1.1	6.9 ± 1.4	9.9 ± 0.6	6.0–18.0
Neut%	19 ± 4.6	21.5 ± 6.8	20.4 ± 3.2	20 ± 4.6	27.3 ± 5.2	20.9 ± 6	22.2 ± 8.7	34 ± 14	20.4 ± 3.5	20.8 ± 3.6	32.7 ± 7.2	21.1 ± 3.1	10.0–30.0
Lymp%	75.4 ± 5.8	72.8 ± 6.9	74.1 ± 4.7	66.4 ± 21.1	64.4 ± 5.4	73.4 ± 6.9	71.7 ± 9	56.7 ± 16.6	73.4 ± 3	72.3 ± 4.1	57 ± 9.9	72.7 ± 4.2	65.0–85.0
Mono%	4.3 ± 0.9	5.3 ± 0.8	4.5 ± 0.7	4.88 ± 0.87	6.67 ± 2.11	4.04 ± 1.66	4.2 ± 1.6	6.7 ± 3	3.9 ± 1.9	4.9 ± 1.1	8.6 ± 2.5	4.2 ± 0.3	0.0–5.0
Eos%	0.8 ± 0.2	0.4 ± 0.4	0.7 ± 0.8	1.43 ± 0.95	1.37 ± 0.85	1.17 ± 0.98	1.7 ± 1.4	2.2 ± 1.5	1.7 ± 0.2	1.7 ± 0.9	1.6 ± 1.2	1.4 ± 0.5	0.0–6.0
Baso%	0.5 ± 0.2	0.1 ± 0.1	0.7 ± 0.3	0.22 ± 0.18	0.24 ± 0.24	0.52 ± 0.48	0.2 ± 0.1	0.5 ± 0.7	0.5 ± 0.2	0.4 ± 0.5	0.2 ± 0.2	0.6 ± 0.3	0.0–1.0
HGB (g/dL)	15.4 ± 0.9	14.5 ± 0.4	14.6 ± 1.4	15.2 ± 1.5	13.4 ± 1.2	14.9 ± 1.9	16.2 ± 0.8	14.8 ± 0.3	15.4 ± 0.9	15.7 ± 0.7	14.6 ± 0.7	15.1 ± 0.2	9.2–11.0
HCT (%)	46.1 ± 4	42.7 ± 0.5	44.2 ± 0.9	44.4 ± 2.3	40.8 ± 2.9	42.8 ± 3.6	45.9 ± 2.7	42.7 ± 1.1	43.7 ± 2.4	44.5 ± 2.8	41.8 ± 2.2	42.9 ± 0.5	36.0–54.0
PLT (1000 cells/uL)	971 ± 161	1125.3 ± 430.2	1363.7 ± 299.4	1109 ± 146	982 ± 151	735 ± 226	1084.6 ± 77.9	996 ± 168.1	848.8 ± 156.3	1084.6 ± 77.9	996 ± 168.1	848.8 ± 156.3	300–500

Abbreviations: WBC, white blood cells; Neut, neutrophils; Lymp, lymphocytes; Mono, monocytes; Eos, eosinophils; Baso, basophils; HGB, hemoglobin; HCT, hematocrit; PLT, platelet count.
N.B. Reference ranges for rats were provided by UC Davis Comparative Pathology Laboratory. Group I saline control serves as additional reference to account for species and age.

Table S.4.9: Liver-kidney (L-K) panel at baseline, 20 minutes, and 2 weeks post-injection

Test	Group I: Saline control (n = 3)			Group II: Co-Pol (n = 10)			Group III: Impurity II (n = 5)			Group IV: Impurity III (n = 5)			Reference range
	baseline	20 min	2-week	baseline	20-min	2-week	baseline	20-min	2-week	baseline	20-min	2-week	
ALT (U/L)	28.5 ± 4.1	27.1 ± 3.9	29.5 ± 2.8	45.1 ± 18.4	31.9 ± 6.3	30.5 ± 6.3	33.5 ± 5.2	30.7 ± 2.8	30.5 ± 3.5	34.8 ± 4.6	31.6 ± 4.7	34.1 ± 2.8	12–67
AST (U/L)	59.6 ± 15.9	64.4 ± 29.4	68 ± 7.7	72.8 ± 22.6	62.2 ± 11.9	55.3 ± 13	61.4 ± 3.8	60.3 ± 3.8	55.6 ± 3.7	68 ± 7.9	67 ± 5.6	61.8 ± 3.4	14–113
ALB (g/dL)	4 ± 0.1	3.9 ± 0.1	3.9 ± 0.6	4.1 ± 0.2	3.6 ± 0.2	2.8 ± 0.2	3.9 ± 0.1	3.6 ± 0.2	3.8 ± 0.2	3.9 ± 0.1	3.6 ± 0.2	3.8 ± 0.1	2.7–4.6
Alk Phos (U/L)	106 ± 1.2	106.1 ± 4	107.1 ± 12	179.5 ± 36.1	152 ± 25	114.6 ± 32.4	143.6 ± 15.5	125.6 ± 20.5	124.9 ± 15.4	153.7 ± 21.8	136.1 ± 18.1	139.9 ± 25.4	136–188
BUN (mg/dL)	14.5 ± 1.1	19.7 ± 3.3	16.7 ± 4.6	16.2 ± 1.8	18.7 ± 2.2	13.6 ± 1.8	17.9 ± 3.2	19.8 ± 3.3	20 ± 4.2	16.9 ± 2.2	18.6 ± 2.6	19.3 ± 1.7	10–25
Cr (mg/dL)	0.23 ± 0.02	0.25 ± 0.03	0.29 ± 0.05	0.3 ± 0.03	0.3 ± 0.05	0.2 ± 0.04	0.31 ± 0.04	0.31 ± 0.05	0.28 ± 0.05	0.33 ± 0.01	0.31 ± 0.01	0.3 ± 0.03	0.8–1.8
TBIL (mg/dL)	0.066 ± 0.005	0.062 ± 0.033	0.126 ± n.a.	0.028 ± 0.019	0.035 ± 0.025	0.028 ± 0.022	0.026 ± 0.016	0.042 ± 0.009	0.05 ± 0.018	0.037 ± 0.018	0.021 ± 0.023	0.059 ± 0.029	0.2–0.7
TP (g/dL)	5.7 ± 0.5	5.5 ± 0.3	5.7 ± 0.4	5.8 ± 0.2	5.1 ± 0.3	4 ± 0.2	5.6 ± 0.1	5.2 ± 0.3	5.4 ± 0.3	5.6 ± 0.2	5.2 ± 0.3	5.6 ± 0.2	5.3–7.5

Abbreviations: ALT, alanine aminotransferase; U/L, international unit/L; AST, aspartate aminotransferase; ALB, Albumin; Alk Phos, alkaline phosphatase; BUN, blood urea nitrogen; Cr, Creatinine; TBIL, Total Bilirubin; TP, Total protein.

N.B. Reference ranges for rats were provided by UC Davis Comparative Pathology Laboratory. Group I saline control serves as additional reference to account for species and age.

4.5.6 Urea-specific RF pulse design
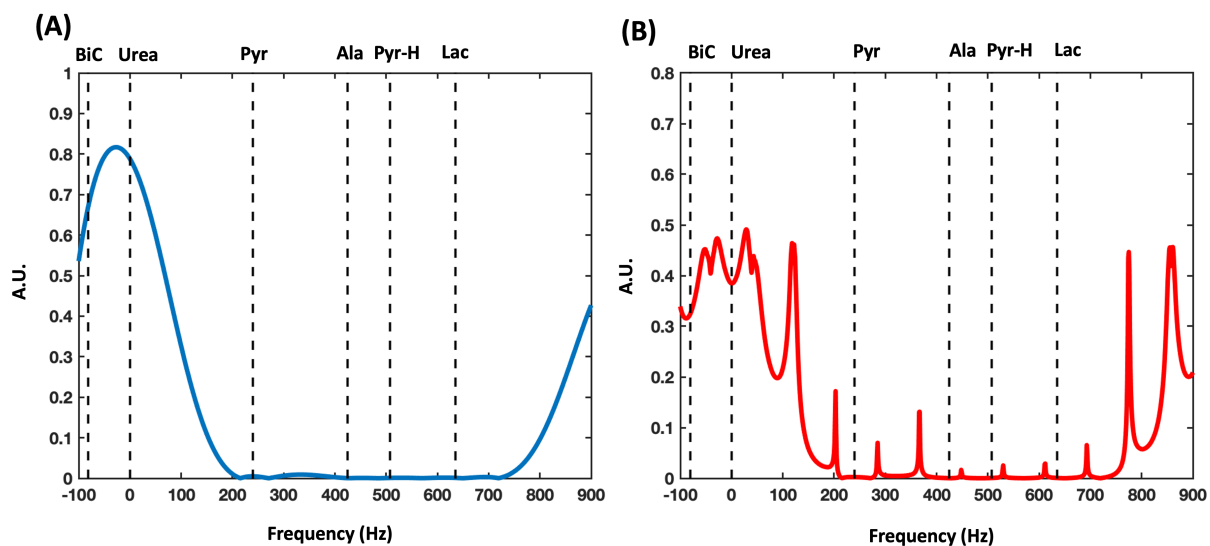
Figure S.4.13: (A) The excitation spectral profile of the ^{13}C urea frequency-specific, non-spatially selective RF pulse shows that the ^{13}C urea resonance (referenced at 0 Hz) is targeted by the RF pulse with minimal perturbations to ^{13}C pyruvate, alanine, pyruvate hydrate, and lactate (dash lines). However, the ^{13}C bicarbonate resonance is also excited by this RF pulse, limiting its application to organs or diseases where the bicarbonate signal is negligible. (B) The transverse magnetization responses of the urea-specific balance steady-state free precession (bSSFP) sequence show no overlaps between spectral banding artifacts (peaks outside the urea spectral region) and resonance frequencies of metabolites of interests (dash lines). Abbreviations: BiC, bicarbonate; Pyr, pyruvate; Ala, alanine; Pyr-H, pyruvate hydrate; Lac, lactate.

References

[1] D. G. Nishimura, <u>Principles of Magnetic Resonance Imaging</u>. Standford Univ., 2010.

[2] M. H. Levitt, <u>Spin Dynamics: Basics of Nuclear Magnetic Resonance</u>. John Wiley & Sons, 2013.

[3] C. Dean, "Zeeman splitting of nuclear quadrupole resonances," <u>Phys. Rev.</u>, vol. 96, pp. 1053–1059, 4 1954.

[4] P. A. Bottomley, "The basics," in <u>eMagRes</u>, R. K. Harris and R. L. Wasylishen, Eds., Chichester, UK: John Wiley & Sons, Ltd, 2015 d, pp. 505–524, ISBN: 9780470034590.

[5] D. W. McRobbie, E. A. Moore, M. J. Graves, and M. R. Prince, "Getting in tune: Resonance and relaxation," in <u>MRI from Picture to Proton</u>, 3rd ed. Cambridge University Press, 2017, pp. 124–143.

[6] "Pulse sequence diagram," <u>RadiologyKey.com</u>, 2016.

[7] G. B. Chavhan, P. S. Babyn, B. G. Jankharia, H.-L. M. Cheng, and M. M. Shroff, "Steady-state MR imaging sequences: Physics, classification, and clinical applications.," <u>Radiographics</u>, vol. 28, no. 4, pp. 1147–1160, 2008.

[8] "Pulse sequences: Part i," <u>RadiologyKey.com</u>, 2016.

[9] P. A. Bottomley and J. R. Griffiths, <u>Handbook of MRI pulse sequences</u>. Elsevier, 2004, ISBN: 9780120928613.

[10] J. H. Ardenkjaer-Larsen, B. Fridlund, A. Gram, G. Hansson, L. Hansson, M. H. Lerche, R. Servin, M. Thaning, and K. Golman, "Increase in signal-to-noise ratio of >10,000 times in liquid-state NMR.," <u>Proc Natl Acad Sci USA</u>, vol. 100, no. 18, pp. 10 158–10 163, 2003.

[11] J. H. Ardenkjaer-Larsen, S. Macholl, and H. Jhannesson, "Dynamic nuclear polarization with trityls at 1.2 k," <u>Appl Magn Reson</u>, vol. 34, no. 3-4, pp. 509–522, 2008.

[12] N. Abhyankar and V. Szalai, "Challenges and advances in the application of dynamic nuclear polarization to liquid-state NMR spectroscopy.," <u>J Phys Chem B</u>, 2021.

[13] Z. J. Wang, M. A. Ohliger, P. E. Z. Larson, J. W. Gordon, R. A. Bok, J. Slater, J. E. Villanueva-Meyer, C. P. Hess, J. Kurhanewicz, and D. B. Vigneron, "Hyperpolarized 13C MRI: State of the art and future directions.," Radiology, vol. 291, no. 2, pp. 273–284, 2019.

[14] B. Corzilius, "Theory of solid effect and cross effect dynamic nuclear polarization with half-integer high-spin metal polarizing agents in rotating solids.," Phys Chem Chem Phys, vol. 18, no. 39, pp. 27 190–27 204, 2016.

[15] J. H. Ardenkjaer-Larsen, "Hyperpolarization by dissolution dynamic nuclear polarization," in Dynamic hyperpolarized nuclear magnetic resonance, T. Jue and D. Mayer, Eds., Cham: Springer International Publishing, 2021, pp. 1–26, ISBN: 978-3-030-55041-7.

[16] C. F. Hwang and D. A. Hill, "Phenomenological model for the new effect in dynamic polarization," Phys. Rev. Lett., vol. 19, no. 18, pp. 1011–1014, 1967.

[17] A. Equbal, Y. Li, T. Tabassum, and S. Han, "Crossover from a solid effect to thermal mixing 1H dynamic nuclear polarization with trityl-OX063.," J Phys Chem Lett, vol. 11, no. 9, pp. 3718–3723, 2020.

[18] Y. Li, A. Equbal, T. Tabassum, and S. Han, "1H thermal mixing dynamic nuclear polarization with BDPA as polarizing agents.," J Phys Chem Lett, vol. 11, no. 21, pp. 9195–9202, 2020.

[19] J. Maidens, J. W. Gordon, M. Arcak, and P. E. Z. Larson, "Optimizing flip angles for metabolic rate estimation in hyperpolarized carbon-13 MRI.," IEEE Trans Med Imaging, vol. 35, no. 11, pp. 2403–2412, 2016.

[20] J. W. Gordon, H.-Y. Chen, N. Dwork, S. Tang, and P. E. Z. Larson, "Fast imaging for hyperpolarized MR metabolic imaging.," J Magn Reson Imaging, vol. 53, no. 3, pp. 686–702, 2021.

[21] Y.-F. Yen, S. J. Kohler, A. P. Chen, J Tropp, R Bok, J Wolber, M. J. Albers, K. A. Gram, M. L. Zierhut, I Park, V Zhang, S Hu, S. J. Nelson, D. B. Vigneron, J Kurhanewicz, H. A. A. M. Dirven, and R. E. Hurd, "Imaging considerations for in vivo 13C metabolic mapping using hyperpolarized 13C-pyruvate.," Magn Reson Med, vol. 62, no. 1, pp. 1–10, 2009.

[22] F. Wiesinger, E. Weidl, M. I. Menzel, M. A. Janich, O. Khegai, S. J. Glaser, A. Haase, M. Schwaiger, and R. F. Schulte, "IDEAL spiral CSI for dynamic metabolic MR imaging of hyperpolarized [1-13C]pyruvate.," Magn Reson Med, vol. 68, no. 1, pp. 8–16, 2012.

[23] W. Jiang, M. Lustig, and P. E. Z. Larson, "Concentric rings k-space trajectory for hyperpolarized (13)c MR spectroscopic imaging.," Magn Reson Med, vol. 75, no. 1, pp. 19–31, 2016.

[24] H.-Y. Chen, P. E. Z. Larson, R. A. Bok, C. von Morze, R. Sriram, R. Delos Santos, J. Delos Santos, J. W. Gordon, N. Bahrami, M. Ferrone, J. Kurhanewicz, and D. B. Vigneron, "Assessing prostate cancer aggressiveness with hyperpolarized dual-agent 3D dynamic imaging of metabolism and perfusion.," Cancer Res, vol. 77, no. 12, pp. 3207–3216, 2017.

[25] J. W. Gordon, R. B. Hansen, P. J. Shin, Y. Feng, D. B. Vigneron, and P. E. Z. Larson, "3D hyperpolarized c-13 EPI with calibrationless parallel imaging.," J Magn Reson, vol. 289, pp. 92–99, 2018.

[26] A. D. Elster, Chemical shift imaging.

[27] C. H. Meyer, J. M. Pauly, A Macovski, and D. G. Nishimura, "Simultaneous spatial and spectral selective excitation.," Magn Reson Med, vol. 15, no. 2, pp. 287–304, 1990.

[28] Y. Xing, G. D. Reed, J. M. Pauly, A. B. Kerr, and P. E. Z. Larson, "Optimal variable flip angle schemes for dynamic acquisition of exchanging hyperpolarized substrates.," J Magn Reson, vol. 234, pp. 75–81, 2013.

[29] C. M. Walker, D. Fuentes, P. E. Z. Larson, V. Kundra, D. B. Vigneron, and J. A. Bankson, "Effects of excitation angle strategy on quantitative analysis of hyperpolarized pyruvate.," Magn Reson Med, vol. 81, no. 6, pp. 3754–3762, 2019.

[30] P. E. Z. Larson, H.-Y. Chen, J. W. Gordon, N. Korn, J. Maidens, M. Arcak, S. Tang, M. Criekinge, L. Carvajal, D. Mammoli, R. Bok, R. Aggarwal, M. Ferrone, J. B. Slater, S. J. Nelson, J. Kurhanewicz, and D. B. Vigneron, "Investigation of analysis methods for hyperpolarized 13C-pyruvate metabolic MRI in prostate cancer patients.," NMR Biomed, vol. 31, no. 11, e3997, 2018.

[31] S. Tang, E. Milshteyn, G. Reed, J. Gordon, R. Bok, X. Zhu, Z. Zhu, D. B. Vigneron, and P. E. Z. Larson, "A regional bolus tracking and real-time b1 calibration method for hyperpolarized 13C MRI.," Magn Reson Med, vol. 81, no. 2, pp. 839–851, 2018.

[32] D. Hanahan and R. A. Weinberg, "Hallmarks of cancer: The next generation.," Cell, vol. 144, no. 5, pp. 646–674, 2011.

[33] P. S. Ward and C. B. Thompson, "Metabolic reprogramming: A cancer hallmark even warburg did not anticipate.," Cancer Cell, vol. 21, no. 3, pp. 297–308, 2012.

[34] R. A. Gatenby and R. J. Gillies, "Why do cancers have high aerobic glycolysis?" Nat Rev Cancer, vol. 4, no. 11, pp. 891–899, 2004.

[35] Y. Kato, S. Ozawa, C. Miyamoto, Y. Maehata, A. Suzuki, T. Maeda, and Y. Baba, "Acidic extracellular microenvironment and cancer.," Cancer Cell Int, vol. 13, no. 1, p. 89, 2013.

[36] G. A. Brooks, H Dubouchaud, M Brown, J. P. Sicurello, and C. E. Butz, "Role of mitochondrial lactate dehydrogenase and lactate oxidation in the intracellular lactate shuttle.," Proc Natl Acad Sci USA, vol. 96, no. 3, pp. 1129–1134, 1999.

[37] G. A. Brooks, "The science and translation of lactate shuttle theory.," Cell Metab, vol. 27, no. 4, pp. 757–785, 2018.

[38] M. G. Vander Heiden, L. C. Cantley, and C. B. Thompson, "Understanding the warburg effect: The metabolic requirements of cell proliferation.," Science, vol. 324, no. 5930, pp. 1029–1033, 2009.

[39] J. W. Locasale and L. C. Cantley, "Metabolic flux and the regulation of mammalian cell growth.," Cell Metab, vol. 14, no. 4, pp. 443–451, 2011.

[40] A. Luengo, Z. Li, D. Y. Gui, L. B. Sullivan, M. Zagorulya, B. T. Do, R. Ferreira, A. Naamati, A. Ali, C. A. Lewis, C. J. Thomas, S. Spranger, N. J. Matheson, and M. G. Vander Heiden, "Increased demand for NAD+ relative to ATP drives aerobic glycolysis," Molecular cell, 2020.

[41] G. Zhang, Y. Zhang, D. Dong, F. Wang, X. Ma, F. Guan, and L. Sun, "MCT1 regulates aggressive and metabolic phenotypes in bladder cancer.," J Cancer, vol. 9, no. 14, pp. 2492–2501, 2018.

[42] B. Faubert, K. Y. Li, L. Cai, C. T. Hensley, J. Kim, L. G. Zacharias, C. Yang, Q. N. Do, S. Doucette, D. Burguete, H. Li, G. Huet, Q. Yuan, T. Wigal, Y. Butt, M. Ni, J. Torrealba, D. Oliver, R. E. Lenkinski, C. R. Malloy, J. W. Wachsmann, J. D. Young, K. Kernstine, and R. J. DeBerardinis, "Lactate metabolism in human lung tumors.," Cell, vol. 171, no. 2, 358–371.e9, 2017.

[43] A. Tasdogan, B. Faubert, V. Ramesh, J. M. Ubellacker, B. Shen, A. Solmonson, M. M. Murphy, Z. Gu, W. Gu, M. Martin, S. Y. Kasitinon, T. Vandergriff, T. P. Mathews, Z. Zhao, D. Schadendorf, R. J. DeBerardinis, and S. J. Morrison, "Metabolic heterogeneity confers differences in melanoma metastatic potential.," Nature, vol. 577, no. 7788, pp. 115–120, 2020.

[44] S Walenta, M Wetterling, M Lehrke, G Schwickert, K Sundfor, E. K. Rofstad, and W Mueller-Klieser, "High lactate levels predict likelihood of metastases, tumor recurrence, and restricted patient survival in human cervical cancers.," Cancer Res, vol. 60, no. 4, pp. 916–921, 2000.

[45] V. Quennet, A. Yaromina, D. Zips, A. Rosner, S. Walenta, M. Baumann, and W. Mueller-Klieser, "Tumor lactate content predicts for response to fractionated irradiation of human squamous cell carcinomas in nude mice.," Radiother Oncol, vol. 81, no. 2, pp. 130–135, 2006.

[46] U. G. A. Sattler, S. S. Meyer, V. Quennet, C. Hoerner, H. Knoerzer, C. Fabian, A. Yaromina, D. Zips, S. Walenta, M. Baumann, and W. Mueller-Klieser, "Glycolytic metabolism and tumour response to fractionated irradiation.," Radiother Oncol, vol. 94, no. 1, pp. 102–109, 2010.

[47] G. Brandstetter, S. Blatt, J. Goldschmitt, L. Taylor, P. Heymann, B. Al-Nawas, and T. Ziebart, "Targeted sensitization of tumor cells for radiation through monocarboxylate transporters 1 and 4 inhibition in vitro.," Clin Oral Investig, 2020.

[48] A. Pereira-Nunes, S. Simões-Sousa, C. Pinheiro, V. Miranda-Gonçalves, S. Granja, and F. Baltazar, "Targeting lactate production and efflux in prostate cancer.," Biochim Biophys Acta Mol Basis Dis, p. 165 894, 2020.

[49] N Weidner, "Intratumor microvessel density as a prognostic factor in cancer.," <u>Am J Pathol</u>, vol. 147, no. 1, pp. 9–19, 1995.

[50] J. C. Weinreb, J. O. Barentsz, P. L. Choyke, F. Cornud, M. A. Haider, K. J. Macura, D. Margolis, M. D. Schnall, F. Shtern, C. M. Tempany, H. C. Thoeny, and S. Verma, "Pi-rads prostate imaging - reporting and data system: 2015, version 2.," <u>Eur Urol</u>, vol. 69, no. 1, pp. 16–40, 2016.

[51] M. A. Konerding, W Malkusch, B Klapthor, C van Ackern, E Fait, S. A. Hill, C Parkins, D. J. Chaplin, M Presta, and J Denekamp, "Evidence for characteristic vascular patterns in solid tumours: Quantitative studies using corrosion casts.," <u>Br J Cancer</u>, vol. 80, no. 5-6, pp. 724–732, 1999.

[52] P. Baluk, H. Hashizume, and D. M. McDonald, "Cellular abnormalities of blood vessels as targets in cancer.," <u>Curr Opin Genet Dev</u>, vol. 15, no. 1, pp. 102–111, 2005.

[53] C. R. Justus, E. J. Sanderlin, and L. V. Yang, "Molecular connections between cancer cell metabolism and the tumor microenvironment.," <u>Int J Mol Sci</u>, vol. 16, no. 5, pp. 11 055–11 086, 2015.

[54] A. G. Anastasiadis, B. C. Stisser, M. A. Ghafar, M. Burchardt, and R. Buttyan, "Tumor hypoxia and the progression of prostate cancer.," <u>Curr Urol Rep</u>, vol. 3, no. 3, pp. 222–228, 2002.

[55] A. Fraga, R. Ribeiro, P. Príncipe, C. Lopes, and R. Medeiros, "Hypoxia and prostate cancer aggressiveness: A tale with many endings.," <u>Clin Genitourin Cancer</u>, vol. 13, no. 4, pp. 295–301, 2015.

[56] L. Marignol, K. Rivera-Figueroa, T. Lynch, and D. Hollywood, "Hypoxia, notch signalling, and prostate cancer.," <u>Nat Rev Urol</u>, vol. 10, no. 7, pp. 405–413, 2013.

[57] D. A. Mankoff, L. K. Dunnwald, J. R. Gralow, G. K. Ellis, A. Charlop, T. J. Lawton, E. K. Schubert, J. Tseng, and R. B. Livingston, "Blood flow and metabolism in locally advanced breast cancer: Relationship to response to therapy.," <u>J Nucl Med</u>, vol. 43, no. 4, pp. 500–509, 2002.

[58] D. A. Mankoff, L. K. Dunnwald, J. R. Gralow, G. K. Ellis, E. K. Schubert, J. Tseng, T. J. Lawton, H. M. Linden, and R. B. Livingston, "Changes in blood flow and metabolism in locally advanced breast cancer treated with neoadjuvant chemotherapy.," J Nucl Med, vol. 44, no. 11, pp. 1806–1814, 2003.

[59] I Apostolova, F Hofheinz, R Buchert, I. G. Steffen, R Michel, C Rosner, V Prasad, C Kohler, T Derlin, W Brenner, and S Marnitz, "Combined measurement of tumor perfusion and glucose metabolism for improved tumor characterization in advanced cervical carcinoma. a PET/CT pilot study using [15O]water and [18F]fluorodeoxyglucose.," Strahlenther Onkol, vol. 190, no. 6, pp. 575–581, 2014.

[60] W. van Elmpt, C. M. L. Zegers, B. Reymen, A. J. G. Even, A.-M. C. Dingemans, M. Oellers, J. E. Wildberger, F. M. Mottaghy, M. Das, E. G. C. Troost, and P. Lambin, "Multiparametric imaging of patient and tumour heterogeneity in non-small-cell lung cancer: Quantification of tumour hypoxia, metabolism and perfusion.," Eur J Nucl Med Mol Imaging, vol. 43, no. 2, pp. 240–248, 2016.

[61] T. L. Whiteside, "The tumor microenvironment and its role in promoting tumor growth.," Oncogene, vol. 27, no. 45, pp. 5904–5912, 2008.

[62] A. J. Rice, E Cortes, D Lachowski, B. C. H. Cheung, S. A. Karim, J. P. Morton, and A Del Río Hernández, "Matrix stiffness induces epithelial-mesenchymal transition and promotes chemoresistance in pancreatic cancer cells.," Oncogenesis, vol. 6, no. 7, e352, 2017.

[63] H. Jiang, R. J. Torphy, K. Steiger, H. Hongo, A. J. Ritchie, M. Kriegsmann, D. Horst, S. E. Umetsu, N. M. Joseph, K. McGregor, M. J. Pishvaian, E. M. Blais, B. Lu, M. Li, M. Hollingsworth, C. Stashko, K. Volmar, J. J. Yeh, V. M. Weaver, Z. J. Wang, M. A. Tempero, W. Weichert, and E. A. Collisson, "Pancreatic ductal adenocarcinoma progression is restrained by stromal matrix.," J Clin Invest, vol. 130, no. 9, pp. 4704–4709, 2020.

[64] M. W. Dewhirst and T. W. Secomb, "Transport of drugs from blood vessels to tumour tissue.," Nat Rev Cancer, vol. 17, no. 12, pp. 738–750, 2017.

[65] A. Satoh, K. Shuto, S. Okazumi, G. Ohira, T. Natsume, K. Hayano, K. Narushima, H. Saito, T. Ohta, Y. Nabeya, N. Yanagawa, and H. Matsubara, "Role of perfusion CT in assessing

tumor blood flow and malignancy level of gastric cancer.," <u>Dig Surg</u>, vol. 27, no. 4, pp. 253–260, 2010.

[66] K. M. Arnold, N. J. Flynn, A. Raben, L. Romak, Y. Yu, A. P. Dicker, F. Mourtada, and J. Sims-Mourtada, "The impact of radiation on the tumor microenvironment: Effect of dose and fractionation schedules.," <u>Cancer Growth Metastasis</u>, vol. 11, p. 1 179 064 418 761 639, 2018.

[67] I. F. Tannock, R. P. Hill, R. G. Bristow, L. Harrington, <u>et al.</u>, <u>The basic science of oncology, 5e</u>. McGraw-Hill Education, 2013.

[68] S. Azzi, J. K. Hebda, and J. Gavard, "Vascular permeability and drug delivery in cancers.," <u>Front Oncol</u>, vol. 3, p. 211, 2013.

[69] S. J. Nelson, J. Kurhanewicz, D. B. Vigneron, P. E. Z. Larson, A. L. Harzstark, M. Ferrone, M. van Criekinge, J. W. Chang, R. Bok, I. Park, G. Reed, L. Carvajal, E. J. Small, P. Munster, V. K. Weinberg, J. H. Ardenkjaer-Larsen, A. P. Chen, R. E. Hurd, L.-I. Odegardstuen, F. J. Robb, J. Tropp, and J. A. Murray, "Metabolic imaging of patients with prostate cancer using hyperpolarized [1-¹³c]pyruvate.," <u>Sci Transl Med</u>, vol. 5, no. 198, 198ra108, 2013.

[70] I. Park, P. E. Z. Larson, J. W. Gordon, L. Carvajal, H.-Y. Chen, R. Bok, M. Van Criekinge, M. Ferrone, J. B. Slater, D. Xu, J. Kurhanewicz, D. B. Vigneron, S. Chang, and S. J. Nelson, "Development of methods and feasibility of using hyperpolarized carbon-13 imaging data for evaluating brain metabolism in patient studies.," <u>Magn Reson Med</u>, vol. 80, no. 3, pp. 864–873, 2018.

[71] O. J. Rider, A. Apps, J. J. J. J. Miller, J. Y. C. Lau, A. J. M. Lewis, M. A. Peterzan, M. S. Dodd, A. Z. Lau, C. Trumper, F. A. Gallagher, J. T. Grist, K. M. Brindle, S. Neubauer, and D. J. Tyler, "Noninvasive in vivo assessment of cardiac metabolism in the healthy and diabetic human heart using hyperpolarized 13C MRI.," <u>Circ Res</u>, vol. 126, no. 6, pp. 725–736, 2020.

[72] F. A. Gallagher, R. Woitek, M. A. McLean, A. B. Gill, R. Manzano Garcia, E. Provenzano, F. Riemer, J. Kaggie, A. Chhabra, S. Ursprung, J. T. Grist, C. J. Daniels, F. Zaccagna, M.-C. Laurent, M. Locke, S. Hilborne, A. Frary, T. Torheim, C. Boursnell, A. Schiller, I.

Patterson, R. Slough, B. Carmo, J. Kane, H. Biggs, E. Harrison, S. S. Deen, A. Patterson, T. Lanz, Z. Kingsbury, M. Ross, B. Basu, R. Baird, D. J. Lomas, E. Sala, J. Wason, O. M. Rueda, S.-F. Chin, I. B. Wilkinson, M. J. Graves, J. E. Abraham, F. J. Gilbert, C. Caldas, and K. M. Brindle, "Imaging breast cancer using hyperpolarized carbon-13 MRI.," Proc Natl Acad Sci USA, vol. 117, no. 4, pp. 2092–2098, 2020.

[73] S. Tang, M. V. Meng, J. B. Slater, J. W. Gordon, D. B. Vigneron, B. A. Stohr, P. E. Z. Larson, and Z. J. Wang, "Metabolic imaging with hyperpolarized 13 c pyruvate magnetic resonance imaging in patients with renal tumors-initial experience.," Cancer, 2021.

[74] B. T. Chung, H.-Y. Chen, J. Gordon, D. Mammoli, R. Sriram, A. W. Autry, L. M. Le Page, M. Chaumeil, P. Shin, J. Slater, C. T. Tan, C. Suszczynski, S. Chang, Y. Li, R. A. Bok, S. M. Ronen, P. E. Z. Larson, J. Kurhanewicz, and D. B. Vigneron, "First hyperpolarized [2-13C]pyruvate MR studies of human brain metabolism.," J Magn Reson, vol. 309, p. 106 617, 2019.

[75] K. L. Granlund, S.-S. Tee, H. A. Vargas, S. K. Lyashchenko, E. Reznik, S. Fine, V. Laudone, J. A. Eastham, K. A. Touijer, V. E. Reuter, M. Gonen, R. E. Sosa, D. Nicholson, Y. W. Guo, A. P. Chen, J. Tropp, F. Robb, H. Hricak, and K. R. Keshari, "Hyperpolarized MRI of human prostate cancer reveals increased lactate with tumor grade driven by monocarboxylate transporter 1.," Cell Metab, 2019.

[76] Y. Rao, S. Gammon, N. M. Zacharias, T. Liu, T. Salzillo, Y. Xi, J. Wang, P. Bhattacharya, and D. Piwnica-Worms, "Hyperpolarized [1-13C]pyruvate-to-[1-13C]lactate conversion is rate-limited by monocarboxylate transporter-1 in the plasma membrane.," Proc Natl Acad Sci USA, vol. 117, no. 36, pp. 22 378–22 389, 2020.

[77] H. Qin, V. Zhang, R. A. Bok, R. D. Santos, J. A. Cunha, I.-C. Hsu, J. D. Santos Bs, J. E. Lee, S. Sukumar, P. E. Z. Larson, D. B. Vigneron, D. M. Wilson, R. Sriram, and J. Kurhanewicz, "Simultaneous metabolic and perfusion imaging using hyperpolarized 13C MRI can evaluate early and dose-dependent response to radiation therapy in a prostate cancer mouse model.," Int J Radiat Oncol Biol Phys, vol. 107, no. 5, pp. 887–896, 2020.

[78] S. E. Day, M. I. Kettunen, M. K. Cherukuri, J. B. Mitchell, M. J. Lizak, H. D. Morris, S. Matsumoto, A. P. Koretsky, and K. M. Brindle, "Detecting response of rat c6 glioma

116

tumors to radiotherapy using hyperpolarized [1- 13C]pyruvate and 13C magnetic resonance spectroscopic imaging.," Magn Reson Med, vol. 65, no. 2, pp. 557–563, 2011.

[79] A. P. Chen, W. Chu, Y.-P. Gu, and C. H. Cunningham, "Probing early tumor response to radiation therapy using hyperpolarized [1-13c]pyruvate in MDA-MB-231 xenografts.," PLoS ONE, vol. 8, no. 2, e56551, 2013.

[80] K. R. Keshari, D. M. Wilson, M. Van Criekinge, R. Sriram, B. L. Koelsch, Z. J. Wang, H. F. VanBrocklin, D. M. Peehl, T. O'Brien, D. Sampath, R. A. D. Carano, and J. Kurhanewicz, "Metabolic response of prostate cancer to nicotinamide phophoribosyltransferase inhibition in a hyperpolarized MR/PET compatible bioreactor.," Prostate, vol. 75, no. 14, pp. 1601–1609, 2015.

[81] Y. Rao, S. Gammon, M. N. Sutton, N. M. Zacharias, P. Bhattacharya, and D. Piwnica-Worms, "Excess exogenous pyruvate inhibits lactate dehydrogenase activity in live cells in a MCT1-dependent manner.," J Biol Chem, p. 100 775, 2021.

[82] J. Kurhanewicz, D. B. Vigneron, J. H. Ardenkjaer-Larsen, J. A. Bankson, K. Brindle, C. H. Cunningham, F. A. Gallagher, K. R. Keshari, A. Kjaer, C. Laustsen, D. A. Mankoff, M. E. Merritt, S. J. Nelson, J. M. Pauly, P. Lee, S. Ronen, D. J. Tyler, S. S. Rajan, D. M. Spielman, L. Wald, X. Zhang, C. R. Malloy, and R. Rizi, "Hyperpolarized 13C MRI: Path to clinical translation in oncology.," Neoplasia, vol. 21, no. 1, pp. 1–16, 2019.

[83] M. C. W. Oswald, N. Garnham, S. T. Sweeney, and M. Landgraf, "Regulation of neuronal development and function by ROS.," FEBS Lett, vol. 592, no. 5, pp. 679–691, 2018.

[84] M. E. Rice and I Russo-Menna, "Differential compartmentalization of brain ascorbate and glutathione between neurons and glia.," Neuroscience, vol. 82, no. 4, pp. 1213–1223, 1998.

[85] F Fornai, M Saviozzi, S Piaggi, M Gesi, G. U. Corsini, G Malvaldi, and A. F. Casini, "Localization of a glutathione-dependent dehydroascorbate reductase within the central nervous system of the rat.," Neuroscience, vol. 94, no. 3, pp. 937–948, 1999.

[86] F. Gu, V. Chauhan, and A. Chauhan, "Glutathione redox imbalance in brain disorders.," Curr Opin Clin Nutr Metab Care, vol. 18, no. 1, pp. 89–95, 2015.

[87] J. S. Bains and C. A. Shaw, "Neurodegenerative disorders in humans: The role of glutathione in oxidative stress-mediated neuronal death.," Brain Res Brain Res Rev, vol. 25, no. 3, pp. 335–358, 1997.

[88] J. M. May, "Vitamin c transport and its role in the central nervous system.," Subcell Biochem, vol. 56, pp. 85–103, 2012.

[89] J. C. Vera, C. I. Rivas, J Fischbarg, and D. W. Golde, "Mammalian facilitative hexose transporters mediate the transport of dehydroascorbic acid.," Nature, vol. 364, no. 6432, pp. 79–82, 1993.

[90] D. B. Agus, S. S. Gambhir, W. M. Pardridge, C Spielholz, J Baselga, J. C. Vera, and D. W. Golde, "Vitamin c crosses the blood-brain barrier in the oxidized form through the glucose transporters.," J Clin Invest, vol. 100, no. 11, pp. 2842–2848, 1997.

[91] C. L. Farrell, J Yang, and W. M. Pardridge, "GLUT-1 glucose transporter is present within apical and basolateral membranes of brain epithelial interfaces and in microvascular endothelia with and without tight junctions.," J Histochem Cytochem, vol. 40, no. 2, pp. 193–199, 1992.

[92] W. W. Wells, D. P. Xu, Y. F. Yang, and P. A. Rocque, "Mammalian thioltransferase (glutaredoxin) and protein disulfide isomerase have dehydroascorbate reductase activity.," J Biol Chem, vol. 265, no. 26, pp. 15 361–15 364, 1990.

[93] M. P. Washburn and W. W. Wells, "Identification of the dehydroascorbic acid reductase and thioltransferase (glutaredoxin) activities of bovine erythrocyte glutathione peroxidase.," Biochem Biophys Res Commun, vol. 257, no. 2, pp. 567–571, 1999.

[94] J. M. May, Z Qu, and X Li, "Requirement for GSH in recycling of ascorbic acid in endothelial cells.," Biochem Pharmacol, vol. 62, no. 7, pp. 873–881, 2001.

[95] B. S. Winkler, S. M. Orselli, and T. S. Rex, "The redox couple between glutathione and ascorbic acid: A chemical and physiological perspective.," Free Radic Biol Med, vol. 17, no. 4, pp. 333–349, 1994.

118

[96] K. R. Keshari, J. Kurhanewicz, R. Bok, P. E. Z. Larson, D. B. Vigneron, and D. M. Wilson, "Hyperpolarized 13C dehydroascorbate as an endogenous redox sensor for in vivo metabolic imaging.," Proc Natl Acad Sci USA, vol. 108, no. 46, pp. 18 606–18 611, 2011.

[97] S. E. Bohndiek, M. I. Kettunen, D.-e. Hu, B. W. C. Kennedy, J. Boren, F. A. Gallagher, and K. M. Brindle, "Hyperpolarized [1-13C]-ascorbic and dehydroascorbic acid: Vitamin c as a probe for imaging redox status in vivo.," J Am Chem Soc, vol. 133, no. 30, pp. 11 795–11 801, 2011.

[98] K. R. Keshari, V. Sai, Z. J. Wang, H. F. Vanbrocklin, J. Kurhanewicz, and D. M. Wilson, "Hyperpolarized [1-13C]dehydroascorbate MR spectroscopy in a murine model of prostate cancer: Comparison with 18F-FDG PET.," J Nucl Med, vol. 54, no. 6, pp. 922–928, 2013.

[99] C. Baligand, H. Qin, A. True-Yasaki, J. W. Gordon, C. von Morze, J. D. Santos, D. M. Wilson, R. Raffai, P. M. Cowley, A. J. Baker, J. Kurhanewicz, D. H. Lovett, and Z. J. Wang, "Hyperpolarized (13) c magnetic resonance evaluation of renal ischemia reperfusion injury in a murine model.," NMR Biomed, 2017.

[100] D. M. Wilson, V. Di Gialleonardo, Z. J. Wang, V. Carroll, C. Von Morze, A. Taylor, V. Sai, M. VanCriekinge, R. Bok, M. A. Ohliger, and K. R. Keshari, "Hyperpolarized 13C spectroscopic evaluation of oxidative stress in a rodent model of steatohepatitis.," Sci Rep, vol. 7, p. 46 014, 2017.

[101] K. R. Keshari, D. M. Wilson, V. Sai, R. Bok, K.-Y. Jen, P. Larson, M. Van Criekinge, J. Kurhanewicz, and Z. J. Wang, "Noninvasive in vivo imaging of diabetes-induced renal oxidative stress and response to therapy using hyperpolarized 13C dehydroascorbate magnetic resonance.," Diabetes, vol. 64, no. 2, pp. 344–352, 2015.

[102] K. N. Timm, D.-E. Hu, M. Williams, A. J. Wright, M. I. Kettunen, B. W. C. Kennedy, T. J. Larkin, P. Dzien, I. Marco-Rius, S. E. Bohndiek, and K. M. Brindle, "Assessing oxidative stress in tumors by measuring the rate of hyperpolarized [1-13C]dehydroascorbic acid reduction using 13C magnetic resonance spectroscopy.," J Biol Chem, vol. 292, no. 5, pp. 1737–1748, 2017.

[103] V. N. Carroll, C Truillet, B Shen, R. R. Flavell, X Shao, M. J. Evans, H. F. VanBrocklin, P. J. H. Scott, F. T. Chin, and D. M. Wilson, "[(11)c]ascorbic and [(11)c]dehydroascorbic acid, an endogenous redox pair for sensing reactive oxygen species using positron emission tomography.," Chem Commun (Camb), vol. 52, no. 27, pp. 4888–4890, 2016.

[104] K. M. Brindle, "Imaging metabolism with hyperpolarized 13c-labeled cell substrates.," J Am Chem Soc, vol. 137, no. 20, pp. 6418–6427, 2015.

[105] K. R. Keshari and D. M. Wilson, "Chemistry and biochemistry of 13C hyperpolarized magnetic resonance using dynamic nuclear polarization.," Chem Soc Rev, vol. 43, no. 5, pp. 1627–1659, 2014.

[106] J. Kurhanewicz, D. B. Vigneron, K. Brindle, E. Y. Chekmenev, A. Comment, C. H. Cunningham, R. J. Deberardinis, G. G. Green, M. O. Leach, S. S. Rajan, R. R. Rizi, B. D. Ross, W. S. Warren, and C. R. Malloy, "Analysis of cancer metabolism by imaging hyperpolarized nuclei: Prospects for translation to clinical research.," Neoplasia, vol. 13, no. 2, pp. 81–97, 2011.

[107] E. S. Wagner, W. White, M. Jennings, and K. Bennett, "The entrapment of [14C]ascorbic acid in human erythrocytes," Biochimica et Biophysica Acta (BBA) - Biomembranes, vol. 902, no. 1, pp. 133–136, 1987.

[108] C. A. Weber, C. A. Duncan, M. J. Lyons, and S. G. Jenkinson, "Depletion of tissue glutathione with diethyl maleate enhances hyperbaric oxygen toxicity.," Am J Physiol, vol. 258, no. 6 Pt 1, pp. L308–12, 1990.

[109] D. J. Bassett and S. S. Reichenbaugh, "Lung mitochondrial function following oxygen exposure and diethyl maleate-induced depletion of glutathione.," Toxicol Appl Pharmacol, vol. 115, no. 2, pp. 161–167, 1992.

[110] A Blaustein, S. M. Deneke, R. I. Stolz, D Baxter, N Healey, and B. L. Fanburg, "Myocardial glutathione depletion impairs recovery after short periods of ischemia.," Circulation, vol. 80, no. 5, pp. 1449–1457, 1989.

[111] K Kramer, H Dijkstra, and A Bast, "Control of physical exercise of rats in a swimming basin.," Physiol Behav, vol. 53, no. 2, pp. 271–276, 1993.

[112] S. M. Deneke, B. A. Lynch, and B. L. Fanburg, "Transient depletion of lung glutathione by diethylmaleate enhances oxygen toxicity.," J Appl Physiol, vol. 58, no. 2, pp. 571–574, 1985.

[113] R. I. R. Macias, C. Hierro, S. C. de Juan, F. Jimenez, F. Gonzalez-San Martin, and J. J. G. Marin, "Hepatic expression of sodium-dependent vitamin c transporters: Ontogeny, subtissular distribution and effect of chronic liver diseases.," Br J Nutr, vol. 106, no. 12, pp. 1814–1825, 2011.

[114] S. N. Jin, G. H. Mun, J. H. Lee, C. S. Oh, J. Kim, Y. H. Chung, J. S. Kang, J.-G. Kim, D.-H. Hwang, Y. I. Hwang, D. H. Shin, and W. J. Lee, "Immunohistochemical study on the distribution of sodium-dependent vitamin c transporters in the respiratory system of adult rat.," Microsc Res Tech, vol. 68, no. 6, pp. 360–367, 2005.

[115] H Tsukaguchi, T Tokui, B Mackenzie, U. V. Berger, X. Z. Chen, Y Wang, R. F. Brubaker, and M. A. Hediger, "A family of mammalian na+-dependent l-ascorbic acid transporters.," Nature, vol. 399, no. 6731, pp. 70–75, 1999.

[116] K. Nagashima, "Optimum pulse flip angles for multi-scan acquisition of hyperpolarized NMR and MRI.," J Magn Reson, vol. 190, no. 2, pp. 183–188, 2008.

[117] B. L. Koelsch, G. D. Reed, K. R. Keshari, M. M. Chaumeil, R. Bok, S. M. Ronen, D. B. Vigneron, J. Kurhanewicz, and P. E. Z. Larson, "Rapid in vivo apparent diffusion coefficient mapping of hyperpolarized (13) c metabolites.," Magn Reson Med, vol. 74, no. 3, pp. 622–633, 2015.

[118] H. Tu, H. Li, Y. Wang, M. Niyyati, Y. Wang, J. Leshin, and M. Levine, "Low red blood cell vitamin c concentrations induce red blood cell fragility: A link to diabetes via glucose, glucose transporters, and dehydroascorbic acid.," EBioMedicine, vol. 2, no. 11, pp. 1735–1750, 2015.

[119] J. C. Crane, M. P. Olson, and S. J. Nelson, "SIVIC: Open-source, standards-based software for DICOM MR spectroscopy workflows.," Int J Biomed Imaging, vol. 2013, p. 169 526, 2013.

[120] M. G. Sanda, J. A. Cadeddu, E. Kirkby, R. C. Chen, T. Crispino, J. Fontanarosa, S. J. Freedland, K. Greene, L. H. Klotz, D. V. Makarov, J. B. Nelson, G. Rodrigues, H. M. Sandler, M. E. Taplin, and J. R. Treadwell, "Clinically localized prostate cancer: AUA/ASTRO/SUO

guideline. part i: Risk stratification, shared decision making, and care options.," J Urol, vol. 199, no. 3, pp. 683–690, 2018.

[121] J. Chin, R. B. Rumble, M. Kollmeier, E. Heath, J. Efstathiou, T. Dorff, B. Berman, A. Feifer, A. Jacques, and D. A. Loblaw, "Brachytherapy for patients with prostate cancer: American society of clinical oncology/cancer care ontario joint guideline update.," J Clin Oncol, vol. 35, no. 15, pp. 1737–1743, 2017.

[122] M. Roach, G. Hanks, H. Thames, P. Schellhammer, W. U. Shipley, G. H. Sokol, and H. Sandler, "Defining biochemical failure following radiotherapy with or without hormonal therapy in men with clinically localized prostate cancer: Recommendations of the RTOG-ASTRO phoenix consensus conference.," Int J Radiat Oncol Biol Phys, vol. 65, no. 4, pp. 965–974, 2006.

[123] J. D. Cox, M. J. Gallagher, E. H. Hammond, R. S. Kaplan, and P. F. Schellhammer, "Consensus statements on radiation therapy of prostate cancer: Guidelines for prostate re-biopsy after radiation and for radiation therapy with rising prostate-specific antigen levels after radical prostatectomy. american society for therapeutic radiology and oncology consensus panel.," J Clin Oncol, vol. 17, no. 4, p. 1155, 1999.

[124] M. Jalloh, M. S. Leapman, J. E. Cowan, K. Shinohara, K. L. Greene, M. Roach, A. J. Chang, J. M. Chan, J. P. Simko, and P. R. Carroll, "Patterns of local failure following radiation therapy for prostate cancer.," J Urol, vol. 194, no. 4, pp. 977–982, 2015.

[125] J. Hayman, K. H. Hole, T. Seierstad, J. Perin, T. L. DeWeese, P. T. Tran, and W. Lilleby, "Local failure is a dominant mode of recurrence in locally advanced and clinical node positive prostate cancer patients treated with combined pelvic IMRT and androgen deprivation therapy.," Urol Oncol, vol. 37, no. 4, 289.e19–289.e26, 2019.

[126] E. Arrayeh, A. C. Westphalen, J. Kurhanewicz, M. Roach, A. J. Jung, P. R. Carroll, and F. V. Coakley, "Does local recurrence of prostate cancer after radiation therapy occur at the site of primary tumor? results of a longitudinal MRI and MRSI study.," Int J Radiat Oncol Biol Phys, vol. 82, no. 5, e787–93, 2012.

[127] J. M. Crook, E Choan, G. A. Perry, S Robertson, and B. A. Esche, "Serum prostate-specific antigen profile following radiotherapy for prostate cancer: Implications for patterns of failure and definition of cure.," Urology, vol. 51, no. 4, pp. 566–572, 1998.

[128] W. V. Vogel, M. G. E. H. Lam, F. A. Pameijer, U. A. van der Heide, J. B. van de Kamer, M. E. Philippens, M van Vulpen, and M Verheij, "Functional imaging in radiotherapy in the netherlands: Availability and impact on clinical practice.," Clin Oncol (R Coll Radiol), vol. 28, no. 12, e206–e215, 2016.

[129] G. C. Pereira, M. Traughber, and R. F. Muzic, "The role of imaging in radiation therapy planning: Past, present, and future.," Biomed Res Int, vol. 2014, p. 231 090, 2014.

[130] D Thorwarth, "Functional imaging for radiotherapy treatment planning: Current status and future directions-a review.," Br J Radiol, vol. 88, no. 1051, p. 20 150 056, 2015.

[131] V. Y. Zhang, A Westphalen, L Delos Santos, Z. L. Tabatabai, K Shinohara, D. B. Vigneron, and J Kurhanewicz, "The role of metabolic imaging in radiation therapy of prostate cancer.," NMR Biomed, vol. 27, no. 1, pp. 100–111, 2014.

[132] R. E. Hurd, Y.-F. Yen, A. Chen, and J. H. Ardenkjaer-Larsen, "Hyperpolarized 13C metabolic imaging using dissolution dynamic nuclear polarization.," J Magn Reson Imaging, vol. 36, no. 6, pp. 1314–1328, 2012.

[133] C. von Morze, P. E. Z. Larson, S. Hu, H. A. I. Yoshihara, R. A. Bok, A. Goga, J. H. Ardenkjaer-Larsen, and D. B. Vigneron, "Investigating tumor perfusion and metabolism using multiple hyperpolarized (13)c compounds: HP001, pyruvate and urea.," Magn Reson Imaging, vol. 30, no. 3, pp. 305–311, 2012.

[134] J. E. Lee, C. J. Diederich, R. Bok, R. Sriram, R. D. Santos, S. M. Noworolski, V. A. Salgaonkar, M. S. Adams, D. B. Vigneron, and J. Kurhanewicz, "Assessing high-intensity focused ultrasound treatment of prostate cancer with hyperpolarized 13 c dual-agent imaging of metabolism and perfusion.," NMR Biomed, e3962, 2018.

[135] R. Bok, J. Lee, R. Sriram, K. Keshari, S. Sukumar, S. Daneshmandi, D. E. Korenchan, R. R. Flavell, D. B. Vigneron, J. Kurhanewicz, and P. Seth, "The role of lactate metabolism

in prostate cancer progression and metastases revealed by dual-agent hyperpolarized 13C MRSI.," <u>Cancers (Basel)</u>, vol. 11, no. 2, 2019.

[136] D. Eriksson and T. Stigbrand, "Radiation-induced cell death mechanisms.," <u>Tumour Biol</u>, vol. 31, no. 4, pp. 363–372, 2010.

[137] R. Baskar, K. A. Lee, R. Yeo, and K.-W. Yeoh, "Cancer and radiation therapy: Current advances and future directions.," <u>Int J Med Sci</u>, vol. 9, no. 3, pp. 193–199, 2012.

[138] M. I. Koukourakis, A Giatromanolaki, M Panteliadou, S. E. Pouliliou, P. S. Chondrou, S Mavropoulou, and E Sivridis, "Lactate dehydrogenase 5 isoenzyme overexpression defines resistance of prostate cancer to radiotherapy.," <u>Br J Cancer</u>, vol. 110, no. 9, pp. 2217–2223, 2014.

[139] V. C. Sandulache, Y. Chen, J. Lee, A. Rubinstein, M. S. Ramirez, H. D. Skinner, C. M. Walker, M. D. Williams, R. Tailor, L. E. Court, J. A. Bankson, and S. Y. Lai, "Evaluation of hyperpolarized [1-13c]-pyruvate by magnetic resonance to detect ionizing radiation effects in real time.," <u>PLoS ONE</u>, vol. 9, no. 1, e87031, 2014.

[140] N. K. Taunk, J. H. Oh, A. Shukla-Dave, K. Beal, B. Vachha, A. Holodny, and V. Hatzoglou, "Early post-treatment assessment of MRI perfusion biomarkers can predict long-term response of lung cancer brain metastases to stereotactic radiosurgery.," <u>Neuro Oncol</u>, vol. 20, no. 4, pp. 567–575, 2017.

[141] P. A. Hein, C. J. Eskey, J. F. Dunn, and E. B. Hug, "Diffusion-weighted imaging in the follow-up of treated high-grade gliomas: Tumor recurrence versus radiation injury.," <u>AJNR Am J Neuroradiol</u>, vol. 25, no. 2, pp. 201–209, 2004.

[142] D. M. Wilson, K. R. Keshari, P. E. Z. Larson, A. P. Chen, S. Hu, M. Van Criekinge, R. Bok, S. J. Nelson, J. M. Macdonald, D. B. Vigneron, and J. Kurhanewicz, "Multi-compound polarization by DNP allows simultaneous assessment of multiple enzymatic activities in vivo.," <u>J Magn Reson</u>, vol. 205, no. 1, pp. 141–147, 2010.

[143] R. M. Henkelman, "Measurement of signal intensities in the presence of noise in MR images.," <u>Med Phys</u>, vol. 12, no. 2, pp. 232–233, 1985.

[144] H Gudbjartsson and S Patz, "The rician distribution of noisy MRI data.," <u>Magn Reson Med</u>, vol. 34, no. 6, pp. 910–914, 1995.

[145] K. Alhallak, S. V. Jenkins, D. E. Lee, N. P. Greene, K. P. Quinn, R. J. Griffin, R. P. M. Dings, and N. Rajaram, "Optical imaging of radiation-induced metabolic changes in radiation-sensitive and resistant cancer cells.," <u>J Biomed Opt</u>, vol. 22, no. 6, p. 60 502, 2017.

[146] C. A. Hahn, S.-M. Zhou, R. Raynor, A. Tisch, K. Light, T. Shafman, T. Wong, J. Kirkpatrick, T. Turkington, D. Hollis, and L. B. Marks, "Dose-dependent effects of radiation therapy on cerebral blood flow, metabolism, and neurocognitive dysfunction.," <u>Int J Radiat Oncol Biol Phys</u>, vol. 73, no. 4, pp. 1082–1087, 2009.

[147] U Mahmood, A. A. Alfieri, H Thaler, D Cowburn, and J. A. Koutcher, "Radiation dose-dependent changes in tumor metabolism measured by 31P nuclear magnetic resonance spectroscopy.," <u>Cancer Res</u>, vol. 54, no. 18, pp. 4885–4891, 1994.

[148] M. Matsuo, T. Kawai, S. Kishimoto, K. Saito, J. Munasinghe, N. Devasahayam, J. B. Mitchell, and M. C. Krishna, "Co-imaging of the tumor oxygenation and metabolism using electron paramagnetic resonance imaging and 13-c hyperpolarized magnetic resonance imaging before and after irradiation.," <u>Oncotarget</u>, vol. 9, no. 38, pp. 25 089–25 100, 2018.

[149] R. Jakubovic, S. Zhou, C. Heyn, H. Soliman, L. Zhang, R. Aviv, and A. Sahgal, "The predictive capacity of apparent diffusion coefficient (ADC) in response assessment of brain metastases following radiation.," <u>Clin Exp Metastasis</u>, vol. 33, no. 3, pp. 277–284, 2016.

[150] C.-H. Lo, W.-Y. Huang, C.-W. Hsiang, M.-S. Lee, C.-S. Lin, J.-F. Yang, H.-H. Hsu, and W.-C. Chang, "Prognostic significance of apparent diffusion coefficient in hepatocellular carcinoma patients treated with stereotactic ablative radiotherapy.," <u>Sci Rep</u>, vol. 9, no. 1, p. 14 157, 2019.

[151] J. E. Moulder and S Rockwell, "Hypoxic fractions of solid tumors: Experimental techniques, methods of analysis, and a survey of existing data.," <u>Int J Radiat Oncol Biol Phys</u>, vol. 10, no. 5, pp. 695–712, 1984.

[152] S. Huang, C. Liu, G. Dai, Y. R. Kim, and B. R. Rosen, "Manipulation of tissue contrast using contrast agents for enhanced MR microscopy in ex vivo mouse brain.," Neuroimage, vol. 46, no. 3, pp. 589–599, 2009.

[153] N. Howlader, G. Forjaz, M. J. Mooradian, R. Meza, C. Y. Kong, K. A. Cronin, A. B. Mariotto, D. R. Lowy, and E. J. Feuer, "The effect of advances in lung-cancer treatment on population mortality.," N Engl J Med, vol. 383, no. 7, pp. 640–649, 2020.

[154] D Hanahan and R. A. Weinberg, "The hallmarks of cancer.," Cell, vol. 100, no. 1, pp. 57–70, 2000.

[155] D. R. Welch and D. R. Hurst, "Defining the hallmarks of metastasis.," Cancer Res, vol. 79, no. 12, pp. 3011–3027, 2019.

[156] J. M. Specht, B. F. Kurland, S. K. Montgomery, L. K. Dunnwald, R. K. Doot, J. R. Gralow, G. K. Ellis, H. M. Linden, R. B. Livingston, K. H. Allison, E. K. Schubert, and D. A. Mankoff, "Tumor metabolism and blood flow as assessed by positron emission tomography varies by tumor subtype in locally advanced breast cancer.," Clin Cancer Res, vol. 16, no. 10, pp. 2803–2810, 2010.

[157] W van Elmpt, M Das, M. Hüllner, H Sharifi, K Zegers, B Reymen, P Lambin, J. E. Wildberger, E. G. C. Troost, P Veit-Haibach, and D De Ruysscher, "Characterization of tumor heterogeneity using dynamic contrast enhanced CT and FDG-PET in non-small cell lung cancer.," Radiother Oncol, vol. 109, no. 1, pp. 65–70, 2013.

[158] L. K. Dunnwald, J. R. Gralow, G. K. Ellis, R. B. Livingston, H. M. Linden, J. M. Specht, R. K. Doot, T. J. Lawton, W. E. Barlow, B. F. Kurland, E. K. Schubert, and D. A. Mankoff, "Tumor metabolism and blood flow changes by positron emission tomography: Relation to survival in patients treated with neoadjuvant chemotherapy for locally advanced breast cancer.," J Clin Oncol, vol. 26, no. 27, pp. 4449–4457, 2008.

[159] A. J. de Langen, V. van den Boogaart, M. Lubberink, W. H. Backes, J. T. Marcus, H. van Tinteren, J. Pruim, B. Brans, P. Leffers, A.-M. C. Dingemans, E. F. Smit, H. J. M. Groen, and O. S. Hoekstra, "Monitoring response to antiangiogenic therapy in non-small cell lung

cancer using imaging markers derived from PET and dynamic contrast-enhanced MRI.," J Nucl Med, vol. 52, no. 1, pp. 48–55, 2011.

[160] C. von Morze, R. A. Bok, J. M. Sands, J. Kurhanewicz, and D. B. Vigneron, "Monitoring urea transport in rat kidney in vivo using hyperpolarized ^{13}c magnetic resonance imaging.," Am J Physiol Renal Physiol, vol. 302, no. 12, F1658–62, 2012.

[161] A. Z. Lau, J. J. Miller, M. D. Robson, and D. J. Tyler, "Simultaneous assessment of cardiac metabolism and perfusion using copolarized [1-13 c]pyruvate and 13 c-urea.," Magn Reson Med, vol. 77, no. 1, pp. 151–158, 2017.

[162] S. Markovic, A. Fages, T. Roussel, R. Hadas, A. Brandis, M. Neeman, and L. Frydman, "Placental physiology monitored by hyperpolarized dynamic 13c magnetic resonance.," Proc Natl Acad Sci USA, vol. 115, no. 10, E2429–E2436, 2018.

[163] C. von Morze, P. E. Z. Larson, S. Hu, K. Keshari, D. M. Wilson, J. H. Ardenkjaer-Larsen, A. Goga, R. Bok, J. Kurhanewicz, and D. B. Vigneron, "Imaging of blood flow using hyperpolarized 13c urea in preclinical cancer models.," J Magn Reson Imaging, vol. 33, no. 3, pp. 692–697, 2011.

[164] M. Matsuo, S. Matsumoto, J. B. Mitchell, M. C. Krishna, and K. Camphausen, "Magnetic resonance imaging of the tumor microenvironment in radiotherapy: Perfusion, hypoxia, and metabolism.," Semin Radiat Oncol, vol. 24, no. 3, pp. 210–217, 2014.

[165] G. D. Reed, C. von Morze, R. Bok, B. L. Koelsch, M. Van Criekinge, K. J. Smith, H. Shang, P. E. Z. Larson, J. Kurhanewicz, and D. B. Vigneron, "High resolution (13)c MRI with hyperpolarized urea: In vivo t(2) mapping and (15)n labeling effects.," IEEE Trans Med Imaging, vol. 33, no. 2, pp. 362–371, 2014.

[166] S. Tang, R. Bok, H. Qin, G. Reed, M. VanCriekinge, R. Delos Santos, W. Overall, J. Santos, J. Gordon, Z. J. Wang, D. B. Vigneron, and P. E. Z. Larson, "A metabolite-specific 3D stack-of-spiral bSSFP sequence for improved lactate imaging in hyperpolarized [1-13 c]pyruvate studies on a 3T clinical scanner.," Magn Reson Med, vol. 84, no. 3, pp. 1113–1125, 2020.

[167] A. M. Kaushal, A. K. Chakraborti, and A. K. Bansal, "FTIR studies on differential intermolecular association in crystalline and amorphous states of structurally related nonsteroidal anti-inflammatory drugs.," Mol Pharm, vol. 5, no. 6, pp. 937–945, 2008.

[168] R. Wang, C. Pellerin, and O. Lebel, "Role of hydrogen bonding in the formation of glasses by small molecules: A triazine case study," J. Mater. Chem., vol. 19, no. 18, p. 2747, 2009.

[169] G. I. Olgenblum, L. Sapir, and D. Harries, "Properties of aqueous trehalose mixtures: Glass transition and hydrogen bonding.," J Chem Theory Comput, vol. 16, no. 2, pp. 1249–1262, 2020.

[170] K. Koperwas, K. Adrjanowicz, Z. Wojnarowska, A. Jedrzejowska, J. Knapik, and M. Paluch, "Glass-forming tendency of molecular liquids and the strength of the intermolecular attractions.," Sci Rep, vol. 6, p. 36 934, 2016.

[171] J. A. Baird, B. Van Eerdenbrugh, and L. S. Taylor, "A classification system to assess the crystallization tendency of organic molecules from undercooled melts.," J Pharm Sci, vol. 99, no. 9, pp. 3787–3806, 2010.

[172] A. Alhalaweh, A. Alzghoul, D. Mahlin, and C. A. S. Bergström, "Physical stability of drugs after storage above and below the glass transition temperature: Relationship to glass-forming ability.," Int J Pharm, vol. 495, no. 1, pp. 312–317, 2015.

[173] S. Murahashi, H. Yuki, K. Kosai, and F. Doura, "Methylene-hydantoin and related compounds. i. on the reaction of pyruvic acid and urea: The synthesis of 5-methylene-hydantoin," Bull Chem Soc Jpn, vol. 39, no. 7, pp. 1559–1562, 1966.

[174] C. G. Keith, "Intravenous urea in glaucoma.," Br J Ophthalmol, vol. 45, no. 4, pp. 307–311, 1961.

[175] M. Javid, "Effect of urea on cerebrospinal fluid pressure in human subjects," JAMA, vol. 160, no. 11, p. 943, 1956.

[176] A. B. Levin, T. A. Duff, and M. J. Javid, "Treatment of increased intracranial pressure: A comparison of different hyperosmotic agents and the use of thiopental.," Neurosurgery, vol. 5, no. 5, pp. 570–575, 1979.

[177] R. F. Reeder and R. E. Harbaugh, "Administration of intravenous urea and normal saline for the treatment of hyponatremia in neurosurgical patients.," J Neurosurg, vol. 70, no. 2, pp. 201–206, 1989.

[178] P. M. Nielsen, E. S. Szocska Hansen, T. S. Norlinger, R. Norregaard, L. Bonde Bertelsen, H. Stodkilde Jorgensen, and C. Laustsen, "Renal ischemia and reperfusion assessment with three-dimensional hyperpolarized 13 c,15 n2-urea.," Magn Reson Med, vol. 76, no. 5, pp. 1524–1530, 2016.

[179] L. B. Bertelsen, P. M. Nielsen, H. Qi, T. S. Norlinger, X. Zhang, H. Stodkilde-Jorgensen, and C. Laustsen, "Diabetes induced renal urea transport alterations assessed with 3D hyperpolarized 13 c,15 n-urea.," Magn Reson Med, vol. 77, no. 4, pp. 1650–1655, 2017.

[180] L. C. Man, J. M. Pauly, and A Macovski, "Improved automatic off-resonance correction without a field map in spiral imaging.," Magn Reson Med, vol. 37, no. 6, pp. 906–913, 1997.

[181] A. Z. Lau, J. J. Miller, and D. J. Tyler, "Mapping of intracellular pH in the in vivo rodent heart using hyperpolarized [1-13C]pyruvate.," Magn Reson Med, vol. 77, no. 5, pp. 1810–1817, 2017.

Publishing Agreement

It is the policy of the University to encourage open access and broad distribution of all theses, dissertations, and manuscripts. The Graduate Division will facilitate the distribution of UCSF theses, dissertations, and manuscripts to the UCSF Library for open access and distribution. UCSF will make such theses, dissertations, and manuscripts accessible to the public and will take reasonable steps to preserve these works in perpetuity.

I hereby grant the non-exclusive, perpetual right to The Regents of the University of California to reproduce, publicly display, distribute, preserve, and publish copies of my thesis, dissertation, or manuscript in any form or media, now existing or later derived, including access online for teaching, research, and public service purposes.

Hecong Qin
_____   6/10/2021
                    Author Signature   _____
                                                                                            Date